IEEE Access
Multidisciplinary | Rapid Review | Open Access Journal

Received June 15, 2020, accepted June 30, 2020, date of publication July 3, 2020, date of current version July 15, 2020.

Digital Object Identifier 10.1109/ACCESS.2020.3006899

Overview of Phase-Change Materials Based Photonic Devices

JIANMIN WANG, LEI WANG, AND JUN LIU
School of Information Engineering, Nanchang Hangkong University, Nanchang 330063, China

Corresponding author: Lei Wang (leiwang@nchu.edu.cn)

This work was supported in part by the National Natural Science Foundation of China under Grant 61964012, and in part by the Foundation of Jiangxi Science and Technology Department under Grant 20192BAB207009.

ABSTRACT Non-volatile storage memory is widely considered to be one of the most promising candidates to replace dynamic random access memory and even static random access memory. It has recently received particular attention because of its great potential for brain-like neuromorphic applications. Phase-change materials, also known as Chalcogenide alloys, exhibit several especially advantageous traits for non-volatile applications. These include scalability, fast switching speeds, low switching energy and outstanding thermal stability. As a result, most research to date has sought to identify electrical applications for phase-change materials in relation to phase-change random access memory, phase-change memristors and phase-change neuro networks, while overlooking their potential for non-volatile photonic applications. To address this issue, we provide a comprehensive review that examines the remarkable physical properties of phase-change materials for photonic applications, together with emerging phase-change photonic devices. The review begins by presenting the atomic structure and physical properties of phase-change materials, followed by an elaboration of the issues that phase-change materials are currently facing and the strategies being developed to overcome them. The current state-of-the-art and technical challenges confronting phase-change materials in relation to non-volatile photonic applications, such as phase-change photonic memory, phase-change photonic neuro-networks, phase-change metasurfaces and phase-change color displays are then considered. The review concludes by discussing the outlook for successfully implementing phase-change materials in emerging photonic domains.

INDEX TERMS Phase-change material, photonic device, metasurface, neuromorphic application, color display.

I. INTRODUCTION

Electrical memory is a crucial component of modern computers due to its ability to store transient data for subsequent processing and archival data for back up. The concept of 'memory' usually refers to static random access memory (SRAM) and dynamic random access memory (DRAM), which are employed to store temporary data and instructions for subsequent read and execution by Central Processing Units (CPUs), as illustrated in Figure 1. Although both SRAM and DRAM allow for ultra-fast write/read speeds, the inherent volatility of SRAM and DRAM causes data to be lost when the electrical power is cut. This is compounded by the cells of SRAM and DRAM being mainly made up of transistors and capacitors. As Moore's law approaches its limits, further boosting the integration density of conventional volatile memories becomes extremely difficult [1]. In view of this, the concept of properly scalable non-volatile memory has become a topic of intensive study over the past decade, resulting in the emergence of several non-volatile memory devices such as ferroelectric RAM (FeRAM) [2]–[4], magnetic RAM (MRAM) [5]–[7], phase-change RAM (PCRAM) [8]–[10], and resistive RAM (RRAM) [11]–[13]. Out of these competing possibillities, PCRAM offers the widest range of advantages including superb scalability [14], fast write/read speeds [15], low energy consumption [16], and a long data retention time [17]. It is therefore considered a serious option for a future 'universal' memory. As well as its storage, the resistance of a PCRAM device can be retained without external stimulus. It can also be continuously adjusted by changing the magnitude and width of excitation signals, bringing it very close to meeting

The associate editor coordinating the review of this manuscript and approving it for publication was Andrei Muller.

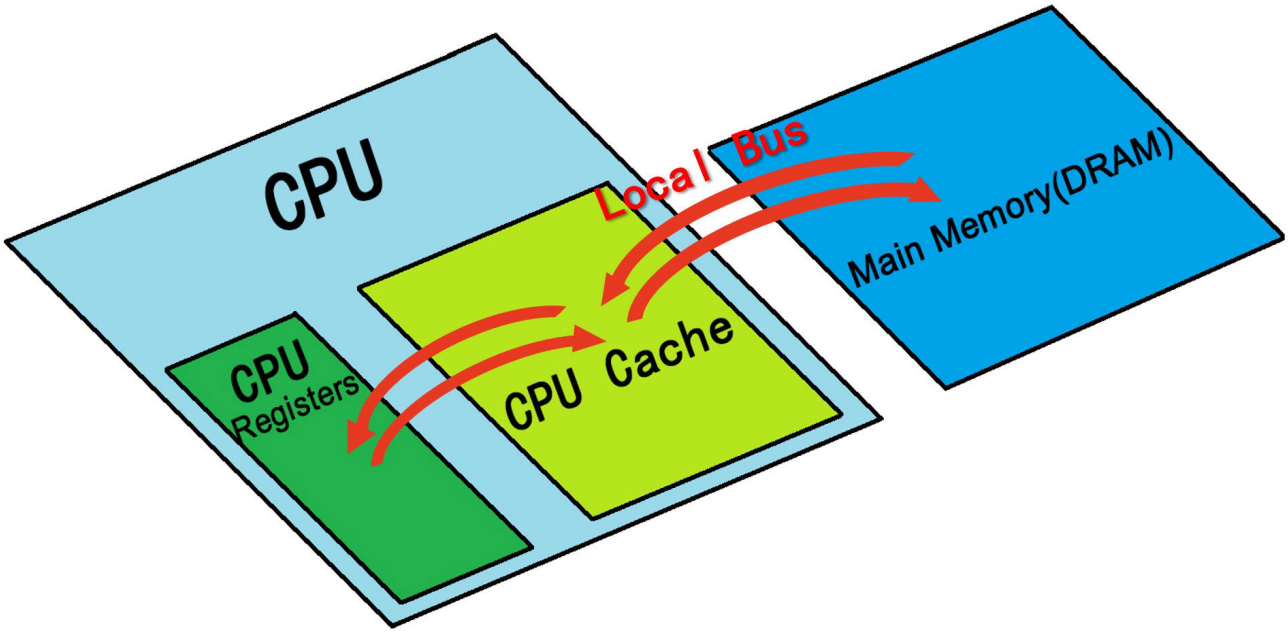

FIGURE 1. Conventional computer architecture having CPU and memory that can be further categorized into static random access memory (also known as Cache) and dynamic random access memory.

the definition of a 'memristor' [18].This offers several concrete new applications of PCRAM, including phase-change synapses [19], [20], phase-change neurons [21], [22], and phase-change neuro networks [23], [24]. It should be noted, however, that the above achievements completely rely on the vast difference in the electrical resistivity of phase-change materials (PCMs) between their crystalline and amorphous states. In addition to this disparity in electrical properties, PCMs also undergo drastic alternations in their optical characteristics during the phase-transition process (e.g., their optical reflectivity, refractive index, and transmission coefficients) [25]. These reconfigurable optical properties do not only imply similar possibilities to their electrical counterparts such as phase-change optical discs [26], phase-change photonic memory [27], and phase-change optical neuro-networks [28], they also allow for some unique applications that cannot be achieved electrically, including phase-change metasurfaces [29] and phase-change color displays [30]. Despite this blossoming interest, comprehensive reviews concerning the material physics of PCMs particularly in relation to their optical traits, latest progress and the potential challenges confronting the goal of realizing non-volatile photonic applications, are thin on the ground. To address this issue and to enable researchers to better the storage and computational qualities of PCMs, this paper presents a comprehensive review of the latest research regarding the remarkable physical properties of PCMs for photonic applications and some of the phase-change photonic devices that are starting to make an appearance. In this review, the atomic structure and physical properties of phase-change materials are first examined. This is followed by a consideration of the principal issues that phase-change materials are currently facing and the corresponding strategies being adopted overcome these drawbacks. The state-of-the-art and technical challenges confronting phase-change materials in relation to non-volatile photonic applications, such as phase-change photonic memory, phase-change photonic neuro-networks, phase-change metasurfaces, and phase-change color displays are then elucidated. The review concludes by discussing the outlooks for successfully implementing phase-change materials in emerging areas of photonic computing.

II. PHASE-CHANGE MATERIALS

It is important to elaborate that PCMs discussed here only refer to Chalcogenide alloy mainly containing chemical elements in group 16 (VI) of the periodic table such as selenium (Se) and tellurium (Te). Recently other review paper also categorized some oxides such as vanadium dioxide (VO_2) into PCMs regime due to their temperature-induced optical properties [31], [32]. However, such phase transition is volatile, as it usually returns to the original state when the material is cooled down below the transition temperature. These oxides cannot therefore directly be employed for non-volatile photonic applications until they are subjected to special sample treatments. For this reason, discussions concerning the potential applications of these oxides are excluded from this review.

The most important feature of the photonic storage materials arises from its capability of providing two different physical/chemical states, corresponding to binary code '0' and '1'. PCMs that can be reversibly transformed between a long-range atomic ordered crystalline state and a short-range

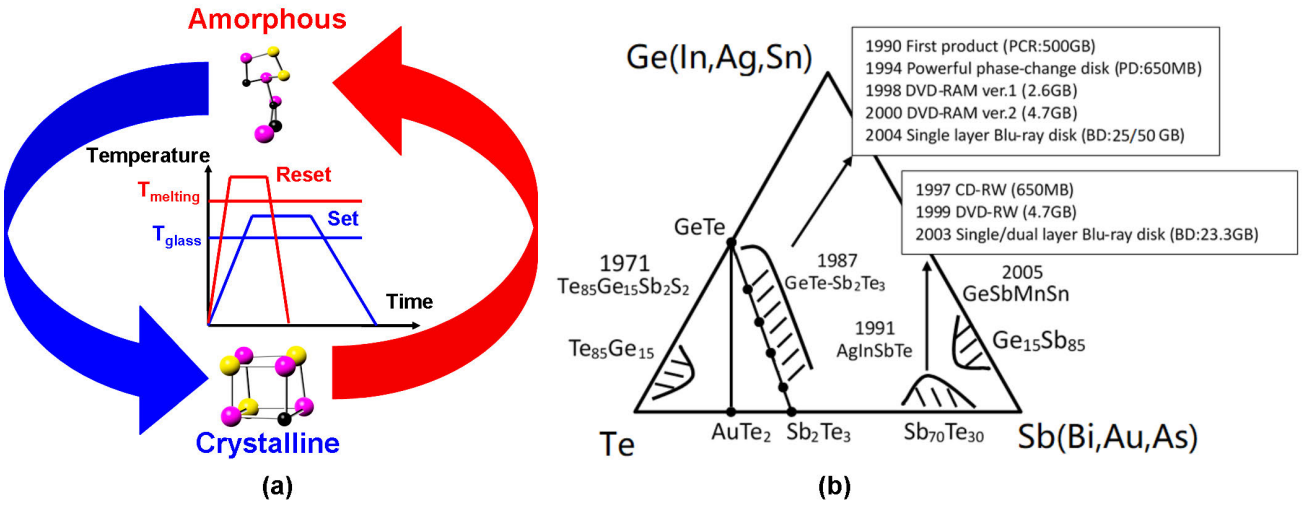

FIGURE 2. (a) Temperature-induced phase transition from amorphization/crystallization to crystallization/amorphization. Crystallization (also called 'SET'), denoted by blue curve, is achieved by heating amorphous PCMs above glass transition temperature (i.e., T_{glass}), whereas heating crystalline PCMs above melting temperature ($T_{melting}$), followed by a subsequent quench, is able to induce amorphization (also called 'RESET), represented by red curve. (b) Ternary Ge-Sb-Te phase diagram showing some popular PCMs with their years of discovery and several milestones in the history of phase-change memories. (b) is reprinted with permission from [25].

atomic ordered amorphous state, as illustrated in Figure 2(a), obviously meet the fundamental requirement for storage medium. However, PCMs suiting for non-volatile photonic applications also need to fulfill the following criterions: (1) pronounced contrast in optical properties; (2) high speed phase transition; (3) relatively low phase-transition temperature; (4) long thermal stability of amorphous state, and (5) large number of rewritable cycles. In this case, only a very few of PCMs during last three decades were found to meet aforementioned demands, as shown in Figure 2(b). Te-based eutectic alloys such as $Te_{85}Ge_{15}$, as good glass formers, were considered as the first PCMs class for storage purpose [33]. Their crystallization time were however found to be of the order of microseconds, thus causing a slow phase-transition speed. This is possibly due to the difficulty in crystallizing in a single-phase material. The subsequent findings of GeTe [34] and $Ge_{11}Te_{60}Sn_4Au_{25}$ [35], [36] that enable both fast crystallization and large optical contrast stimulated the discovery of the pseudo-binary alloys along the GeTe-Sb_2Te_3 tie line, represented by $Ge_2Sb_2Te_5$ (usually abbreviated as GST) [37] and other related alloys such as GeBiTe [38] and GeInSbTe [39]. The GST media, as the most well-known member of PCM families, has been extensively implemented in various electronic and photonic storage devices in both laboratory and industry levels. The second PCMs category of doped Sb_2Te alloys such as $Ag_5In_5Sb_{60}Te_{30}$ were later revealed and received considerable attention for rewriteable optical storage such as DVD-RW and DVD+RW [40], [41]. Besides these, Ge-doped Sb compositions were usually regarded as the third PCMs family.

The PCMs storage medium, as exemplified by GST, can be rapidly and reversibly switched between amorphous and crystalline states. The amorphous GST can be heated above its crystallization temperature but below the melting point, to achieve crystallization. On the other hand, the crystalline GST can be re-amorphized by heating the GST media above its melting temperature, followed by a rapid quenching. The external excitations to trigger required phase-transitions can be either electric pulse for electronic memories or laser pulse for photonic memories. The critical cooling rate for re-amorphization of GST was reported to be 10^9 K/s [42], which can be accomplished by applying a ultra-short laser pulse into the GST media and subsequently switching off the thermal excitation. The optical properties contrast of the GST media between crystalline and amorphous states therefore depends on their atomic structure disparity dramatically. The amorphous GST media during crystallization undergoes several metastable structures at different temperature and eventually reaches a stable phase, while the metastable phases of the GST were reported to be of importance for storage applications [43]. The first metastable phase of the GST, denoted as GST phase 1, which is categorized to the cubic system, displays a rock-salt structure [44], as shown in Figure 3(a). The cation sites are randomly occupied by 40% Ge, 40% Sb and 20% vacancies, and give rise to the mixed GeSb/vacancies sublattice site, whereas the anion sites are taken up by Te atoms. It is instructive to mention that the amount of vacancies in the cation sublattices determines the degree of crystal lattice distortions that result from a fact that the Ge and Sb atoms are off-centered within idealized $Te(GeSb)_6$ [44], [45]. Due to this reason, larger lattice distortions are usually found in GST media with higher amount of vacancies than the counterparts with lower amount of vacancies. GST phase 1 is however energetically unfavorable, and additional thermal energy along with the crystallization process accelerates the atomic motions of Ge and Sb species

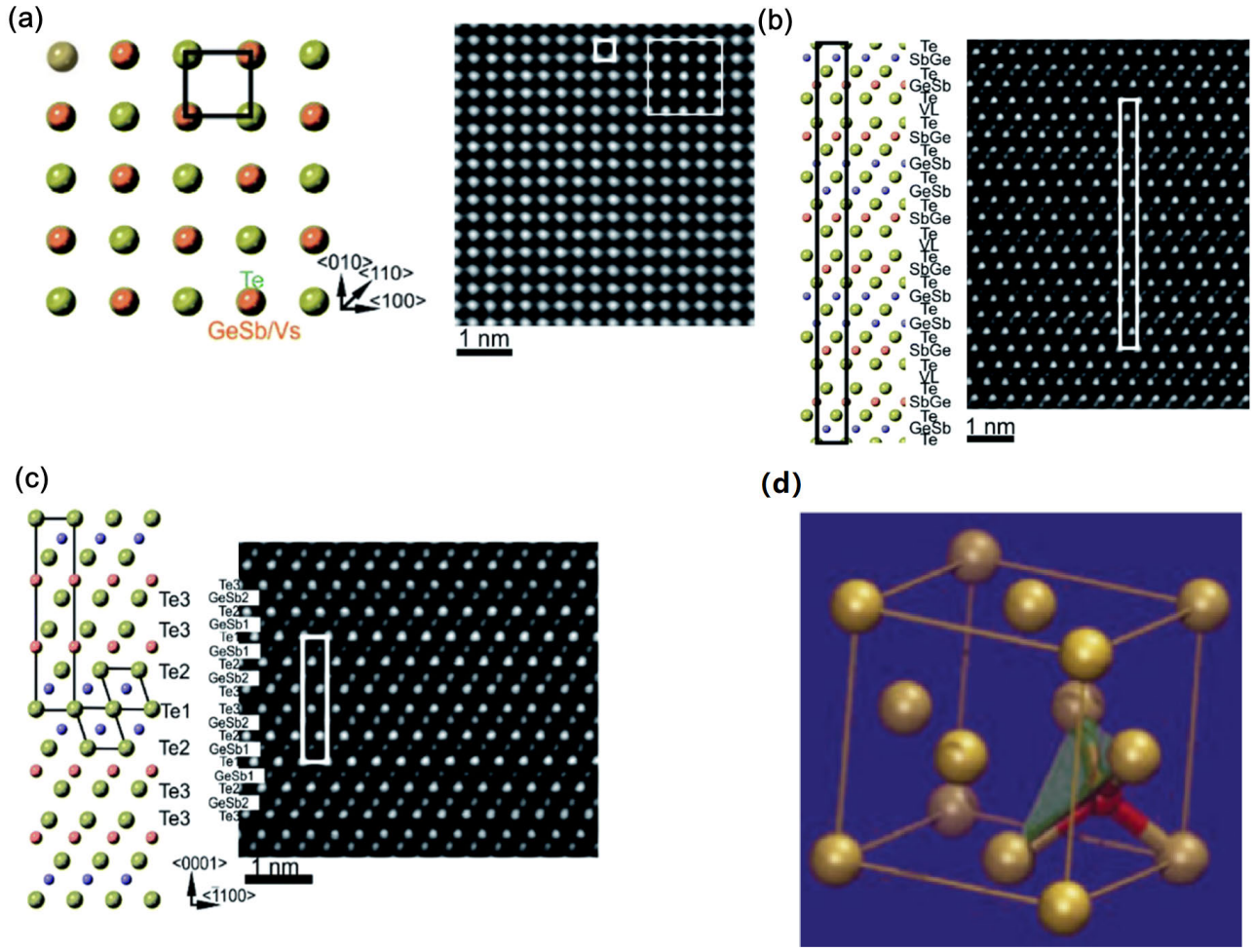

FIGURE 3. (a) ABC cubic stacking of the Te sublattice with the crystal structure of GST at its first metastable phase along < 001 > crystallographic projections. The bright dots are Te/GeSb/vacancies atomic column; (b) Atomic-resolution HAADF-STEM image of GST at its second metastable phase with the corresponding structural model along the [1120] direction; the dark lines in the image represent vacancy layers. (c) Atomic-resolution Cs-corrected HAADF-STEM image of the trigonal GST with the trigonal GST crystal structure. The unit cell is marked by a rectangle and the main structural motif of the motif of the GST phase is marked by an octahedron. (d) Fragments of the local structure of GST around Ge atoms in the amorphous states. Stronger covalent bonds are shown as thicker lines whereas weak interlock bonds are shown as thinner lines. The stronger covalent bonds remain intact on the umbrella-flip structural transformation rendering the Ge sublattic random. (a)-(c) are reprinted with permission from [45], and (d) is reprinted with permission from [54].

and re-arranges the Ge and Sb atoms, thus resulting in the gradual ordering of structural vacancies in the planes in the GST lattice [46]–[49]. Such different vacancies distributions naturally lead to various metastable GST structures, and the most thermodynamically favorable GST phase was reported to have a highly ordered distribution of the vacancies in {111} planes, defined as GST phase 2 that comprises GST building blocks periodically separated by the vacancy layers between adjacent Te-Te planes [50], as illustrated in Figure 3(b). The Ge and Sb atoms are still off-center within $Te(GeSb)_6$, as similar to phase 1, and the degree of vacancy ordering strongly pertains to the Te-Te distance. The distribution of Ge and Sb atomic species is random within individual cation layers, while the ordering of Sb and Ge atoms are preferable to be found in the cation layers next to the vacancy layers and in the middle of GST building units, respectively. The unit cell of GST phase 2 needs to extend along the [22] direction to include 15 Te layers with three vacancy layers in between to introduce these periodic layers into the cubic framework of phase 2, thereby attributing the crystal structure of phase 2 to a superstructure of the rock-salt type with the cubic stacking of Te layers (ABC) [51]. The subsequent heating drives the GST media from its metastable phase eventually towards a stable crystalline state that belongs to the trigonal crystal system and exhibits a layered structure with a 9P-type stacking sequence [52]. The building blocks of the GST stable phase are stacked along the c-axis, and are split periodically from each other by van der wall gaps between adjacent Te layers, as illustrated in Figure 3(c).

There has been also considerable investigations regarding the atomic structure of the amorphous state of the GST material. It was previously presumed that amorphous GST

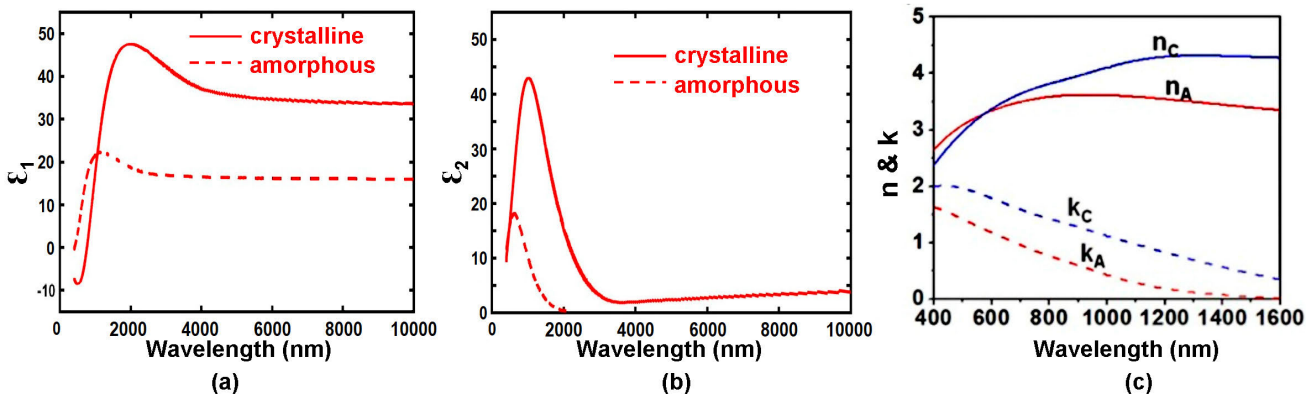

FIGURE 4. Dielectric function (a) $\varepsilon_1(\omega)$ and (b) $\varepsilon_2(\omega)$ of amorphous and crystalline GST with respect to wavelength, and (c) optical constants of GST in amorphous and crystalline states. n_A and k_A are the refractive index and extinction coefficient of a-GST; n_C and k_C are those of c-GST, respectively. (a) and (b) are updated and reprinted from [59], and (c) is reprinted with permission from [60].

had a similar atomic structure to its crystalline counterpart, but lacked any long-range order [53]. If this were the case, despite the lack of long-range atomic order, there might still be some rules to enable tracking of the atomic arrangement of amorphous GST materials. One plausible model assumed the transition between the amorphous and the crystalline states had the character of an 'umbrella flip' with the fast rate of of crystallization being attributable to the similarity in their atomic arrangement [54]. Calculations revealed that the increase of bandgap in the amorphous state depends on a tetrahedral atomic arrangement of the Ge atoms as would be found in a spinel structure [55], [56]. Following an EXAFS spectrographic analysis, it was found that there is a large number of Ge-Ge bonds in GST [57], raising the possibility of an ideal network. X-ray diffraction technologies provided additional evidence that amorphous GST is characterized by even-folded ring structures [58], while amorphous GeTe exhibits both even- and odd-numbered rings [58]. Results from denstiy functional calculations also indicated that amorphous GeTe and GST exhibit long-range ordering of Te atoms and a high degree of alternating four-membered rings (ABAB squares) which are the main building blocks of both [59], [60], while the amorphous $Ge_8Se_2Te_{11}$ presents a larger Ge-Ge coordination number and a larger fraction of Ge atoms with tetrahedral coordination [61]. It is therefore informative to conclude that ring structures play an essential role in the phase change, and ABAB squares, structural units in crystalline GST, are dominant in amorphous GST.

The drastic optical properties contrast of the GST materials between amorphous and crystalline states, as illustrated in Figure 4, was reportedly dependent on its structural disorder due to the presence of the vacancies [62], [63]. The octahedral-like configurations of Ge, Sb and vacancies result in the formation of p-p orbitals that are susceptible to local distortions. The atomic vibrations excited by the thermal source will take apart the alignment of p-p orbitals to the extent that the bonding angles diverge more strongly from 90°, and the variation between the first- and second-nearest neighbors increases [42]. As a result, the amorphous GST where p-p orbitals are not aligned reveals the absence of the resonant bondings, implying a significant reduction on the dielectric constant of the amorphous GST when compared with its crystalline state, as demonstrated in Figures 4(a) and (b). It was reflected from Figure 4 that the GST material displays pronounced difference on its complex permitivity ($\varepsilon = \varepsilon_1 + \varepsilon_2 \cdot \mathrm{i}$) between two physical states. It is evident that the real part of the complex permitivity of the amorphous GST (ε_1) is much smaller than the crystalline case owing to the disruption of the resonant bonding during the amorphization of the crystalline GST. The imaginary part of the complex permitivity (ε_2) of the crystalline GST media that corresponds to the optical absorption is fairly large in wavelength region of < 2800 nm, while reducing considerably when the wavelength is greater than 2800 nm for both crystalline and amorphous phases. With regards to the crystalline GST, the optical reflectivity of the GST media at phase 1 was found to be smaller than other two phases (i.e., phase 2 and the stable phase) based on the first principle simulations and ellipsometric measurements [64], [65]. Such differences are possibly due to the changes in the free carrier absorption caused by electron localization effects. The GST media at phase 2 and the stable phase were reported to exhibit higher ε_2 than the disordered phase 1 [65], which might be attributed to the increased carrier mobility due to vacancy ordering that causes a delocalization of the electronic wave functions. Thanks to this, optical properties of the GST media radically vary along with their respective crystalline states. Hence, different optical properties of the GST alloys can be secured by tailoring the degree of structural order about the vacancy distribution and the degree of electron localization associated with texture of GST alloys [45].

Many photonic applications using PCMs such as color displays, on-chip photonic memory and metadevices rely on the dramatic changes in their optical properties. As a result, devising ways to effectively engineer, optimize and stabilize PCMs is key to being able to properly control their constrast-

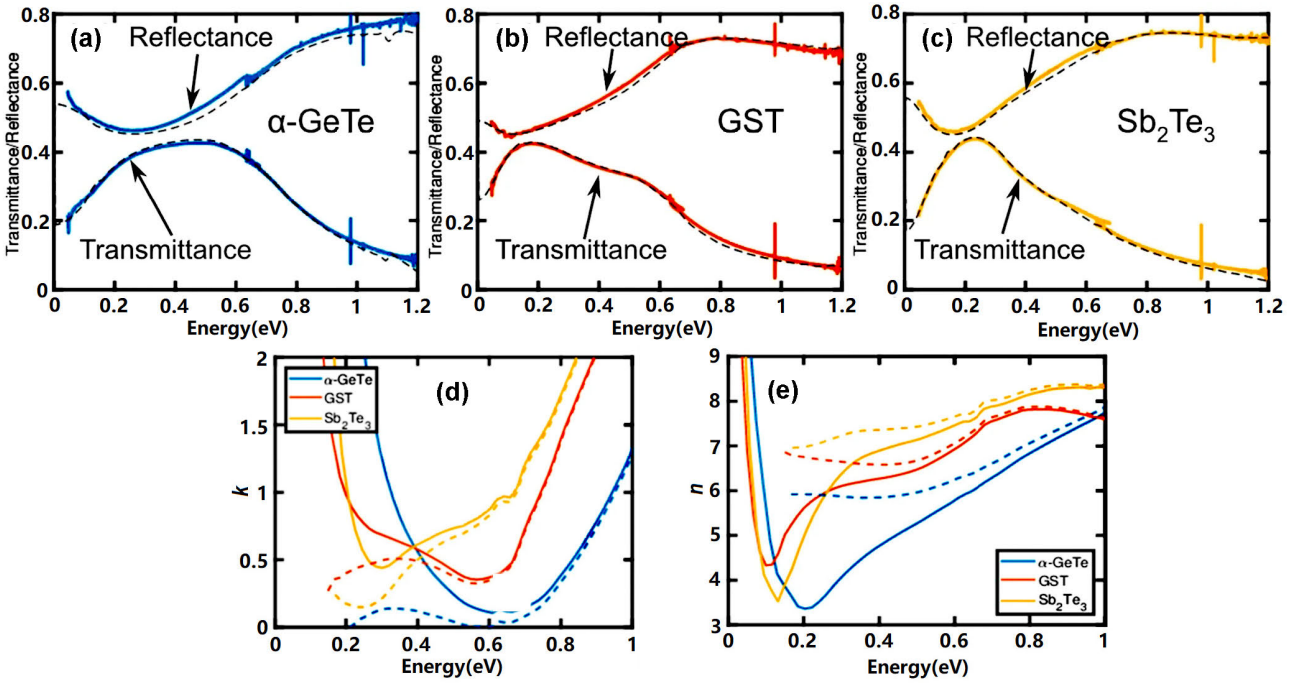

FIGURE 5. Optical characterization of epitaxial phase change materials. Transmittance (lower curves) and reflectance (upper curves) spectra of (a) α-GeTe, (b) GST, and (c) Sb_2Te_3 thin films. The dashed lines indicate fits to the transmittance and reflectance data. (d) Imaginary part k and (e) real part n of the complex refractive index of α-GeTe, GST, and Sb_2Te_3 calculated from the spectra in (a), (b), and (c). The solid lines represent the values of n and k optical constant including free-carrier absorption, whereas the dashed lines indicate the corresponding values without free-carrier absorption.

ing optical characteristics. One promising route is to make use of epitaxial PCMs that provide improved optical properties based on techniques that cannot be implemented on conventional polycrystalline samples [66]. Figures 5(a)-(d) show the transmittance, reflectance, and imaginary part of three epitaxial PCMs, namely, α-GeTe, GST, and Sb_2Te_3. It can be seen that all three samples exhibit similar transmittance and reflectance. Transmittances/reflectances initially increases/decreases at low energy because of the free-electron absorption, whereas decreasing/increasing at high energy due to the interband absorption. The calculated real part of complex refractive index with and without taking free-carrier absorption (Drude peak) into account, as illustrated in Figure 5(e), also indicated a fact that the value of n for α-GeTe is between 0.2 and 1.0 eV, which is smaller than those for Sb_2Te_3 and GST. This is expected as α-GeTe gives rise to the larger energy gap. Sb_2Te_3 however shows analogous values of n to GST. Although GST has larger energy gap and much lower absorption coefficient, such characteristic is offset by the larger absorption coefficient in GST for energies below 0.4 eV, thus making comparable values of n for Sb_2Te_3 and GST around 0.1 eV [66].

III. PHASE-CHANGE PHOTONIC MEMORIES

A. OFF-CHIP STORAGE MEMORY

The popularity of phase-change memories can retrospect to its applications in optical storage devices that mainly serves as the tertiary storage (i.e., off-chip storage) since 1990s [67]. The families of phase-change optical memories that widely adopt the PCMs located in GeTe-Sb_2Te_3 tie line include rewritable compact disc (CD) [68], rewritable digital versatile disc (DVD) [69], and Blu-Ray [70]. As illustrated in Figure 6, a phase-change optical disc usually has a PCM layer sandwiched between two dielectric buffer layers such as ZnS-SiO_2, deposited on a polycarbonate substrate. To record data, a laser spot generated from a laser beam propagating towards an objective lens is focused on PCMs, and the resulting joule heating inside PCMs causes the phase transformation once the corresponding phase-transformation temperature is achieved, as interpreted in Figure 6. To read the previously written bit, a reflected light collected by the objective lens is sent towards the detectors through a beam splitter, producing the readout signals and servo signals for automatic focusing and tracking. Owing to the drastic reflectivity contrast, the intensity of the light when reflected from the written bits shows a pronounced difference from that reflected from surrounding background. The aforementioned storage mechanism clearly indicates that the storage capacity of the phase-change optical disc is mainly dominated by the size of laser spot that is generally estimated by λ/NA where λ is the laser beam wavelength and NA is the numerical aperture of the objective lens that relates to refractive index and half-angle encompassed by the focused cone of light at its apex. Small wavelength and large numerical aperture are therefore preferable in order to enhance the storage capacity. However, further increasing the wavelength beyond 405 nm

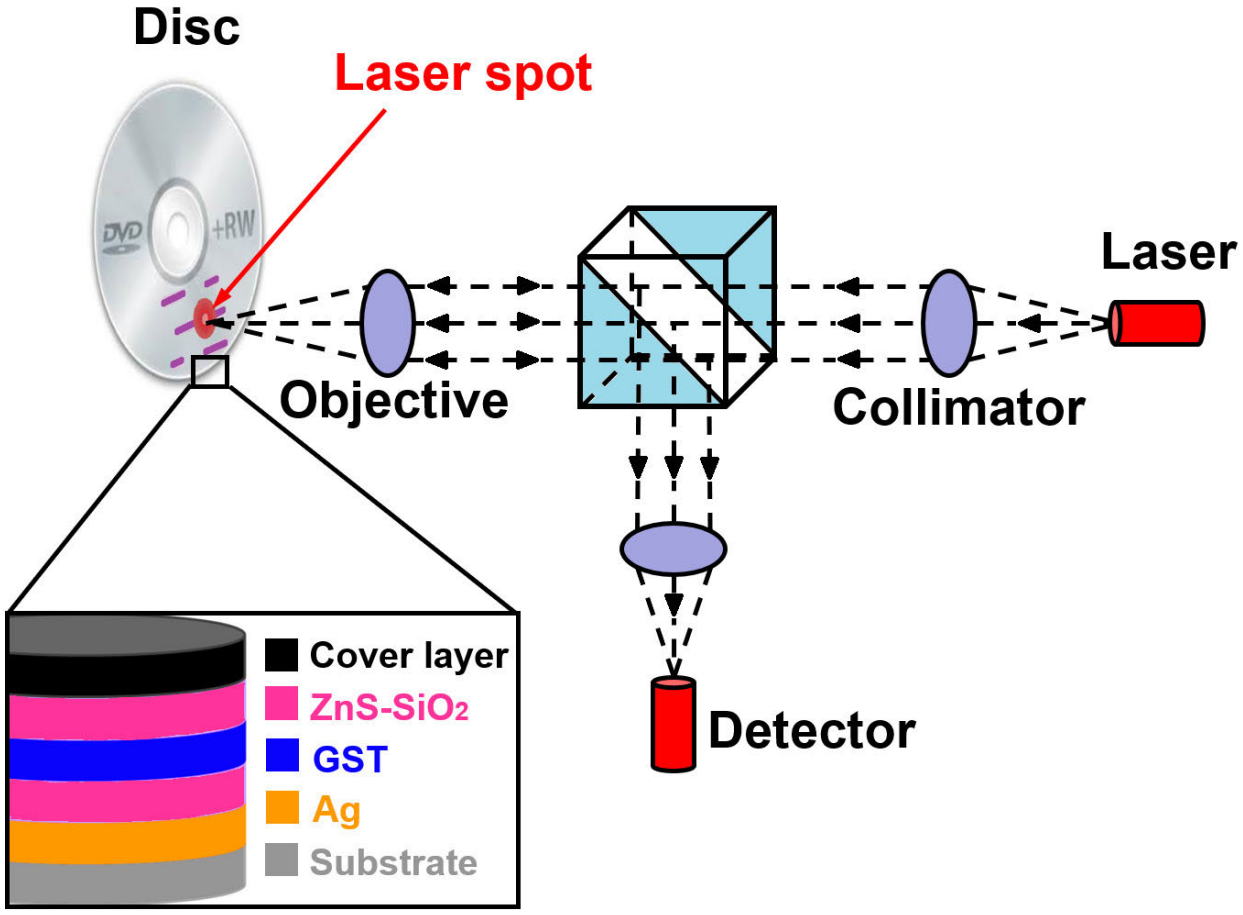

FIGURE 6. Conventional optical storage system showing a typical phase-change optical disc architecture.

(i.e., wavelength of blue light) seems to be a formidable task due to the limited solid state laser technology [71]. Lowering numerical aperture is accompanied with very thin substrate, making device very susceptible to dust and fingerprints. Due to above reasons, state-of-the-art numerical aperture can not exceed 0.85 [72], which restricted the storage capacity of the phase-change optical disc.

Several methods such as near-field recording [73], [74], multi-level [75], [76] and multi-layer storage [77], [78] have been devised during last two decades in order to overcome the diffraction limits. The most promising route within these methods was considered as the near-field optics that takes advantageous of a solid immersion lens (SIL) with high refractive index to physically increase NA. As illustrated in Figure 7(a), the function of SIL inserted between the conventional objective lens and the sample is to make the focal plane of the laser beam coincide with the sample surface. To realize this, a very short gap distance betweenn SIL and sample is required to induce evanescent wave coupling that allows for the laser energy transferred from SIL to the sample to achieve the write operation. Additionally, an extra cover layer with a similar refractive index to NA of SIL is also demanded to minimize the spot size for higher recording density. However, it becomes extremely hard to precisely control the gap distance for a rotational, non-ideal plastic disc. As a result, the concept of Super-resolution near-field structures (Super-RENs) has been proposed to alleviate the drawbacks of conventional near-field optic [74]. The idea of Super-RENs is to fill the space between SIL and sample with a so-called mask layer that is made of the optical nonlinear material whose optical properties can be altered by either light intensity or temperature. To perform readout operation, the mask layer is locally heated up to some certain temperature above the pre-defined threshold level, thereby changing the optical properties significantly in the region where laser beam is focused. A near-field coupling is therefore generated in the same area that is smaller than the optical resolution. This renders the detection of very small bits possible. Multi-level storage method depends on the ability to generate a variety of reflectivity by continuously changing the ratio of the crystalline to amorphous volume. This can be achieved by continuously changing the energy of the thermal source, as demonstrated in Figure 7(b). In this case, one recorded mark is capable of storing multiple bits, which suggests an increase in data density by a factor of $\log_2(n)$ (n denotes the number of the level). In contrast to multi-level technology,

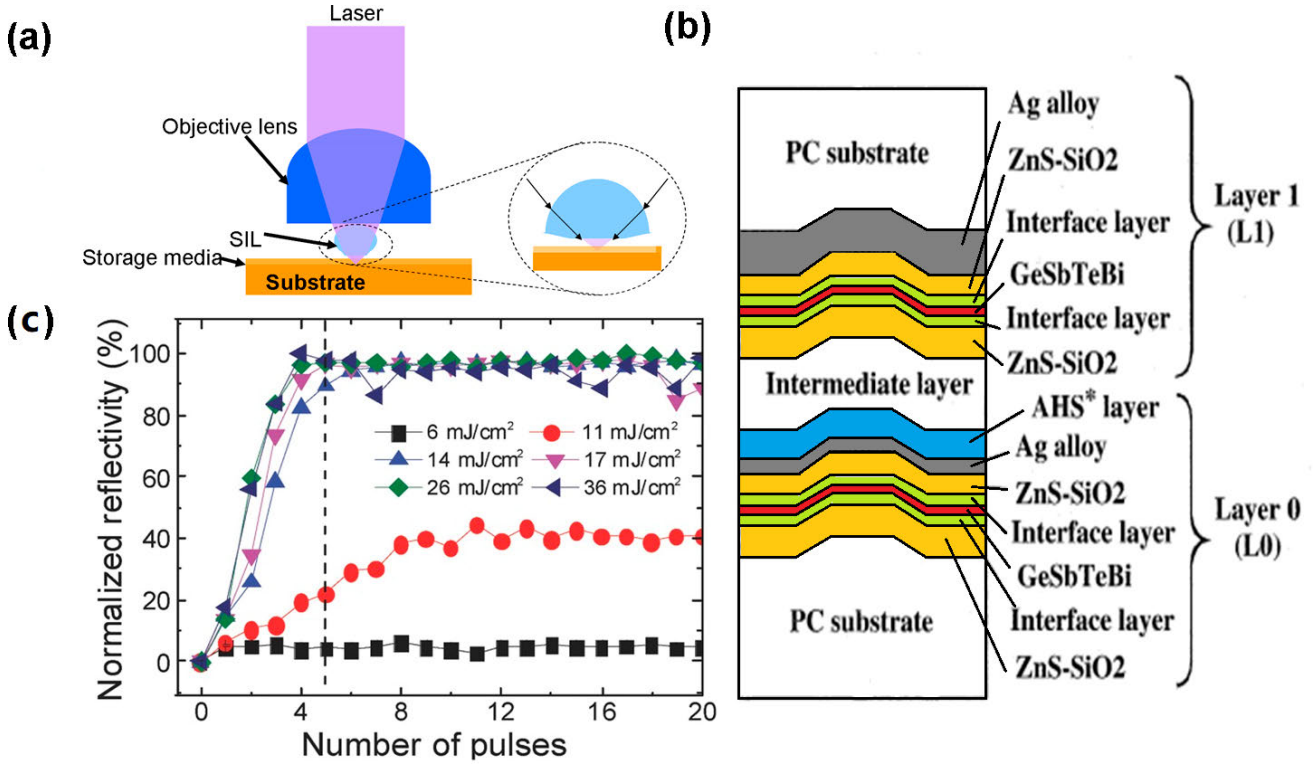

FIGURE 7. (a) Optical near-field storage system; (b) cross-view of a typical dual-layer phase-change optical disc. The basic structure has 10 nm thick PCM layer, 10 nm thick Ag layer and a HfO_2-based interface layer without any optical absorption. To enhance re-writability, a GeTe-Sb_2Te_3 pseudobinary alloy of which a part of Sb was substituted by Bi.(c) optical reflectivity of GeTe films after 20 ns laser pulse irradiation at various fluences between 0 and 36 mJ cm^{-2} as a function of pulse number. (a) is reprinted with permission from [64]; (b) is reprinted with permission from [73]; (c) is updated and reprinted with permission from [75].

multi-layer storage, as depicted in Figure 7(c), enables data store in multiple layers of one disc, stimulating the debut of 3D optical memory [79]. Such 3D optical memory however requires a new form of optical storage means in multiple layers closely packed together simultaneously with minimum interlayer crosstalk, which can be achieved by two-photon absorption.

B. ON-CHIP STORAGE MEMORY

Research relating to On-chip phase-change storage memory is focused on developing a novel non-volatile memory to replace DRAM or even SRAM. A PCRAM device that can provide an electronic solution to the realization of non-volatile storage, is considered one of the most promising contenders for replacing conventional CMOS-based memories. However, it is better to have information transferred in the form of photons because of the much higher bandwidth of optical systems when compared to their electronic analogues [80]. As a result, a great deal of efforts has been devoted to exploring on-chip storage photonic devices using PCMs. The first generation of on-chip photonic devices saw the beginning of phase-change photonic resonators [81]. One particular design here involved overcladding GST media on a silicon (Si) racetrack resonator, as illustrated in Figure 8(a). The resonant wavelength can be reconfigured in the spectral region from 1550.38 to 1550.55 nm by continuously modulating the crystallized proportion of the GST overcladding. This results in changes to the real part of the permittivity (ε_1). A similar GST-based microring resonator was also devised by coating a silicon nitride (Si_3N_4) waveguide with GST media [82] (Figures 8(b)-(e)). The resonating energy is reduced due to the absorption inside the resonator, enabling expansion of the spectral width of the resonance. These innovative ideas inspired the development of a true all-photonic non-volatile memory comprising a thin GST film coated by an indium tin oxide (ITO) film to protect the GST layer from oxidation [83]. This was deposited on top of a half-etched waveguide on an Si_3N_4 substrate, as depicted in Figures 8(f)-(i). During the write operation, an intense light pulse is propagated along the waveguide. The resulting evanescent coupling effect brings about optical energy that is simultaneously absorbed by the GST media where phase transition occurs. The readout operation relies on the large disparity between the refractive index of the amorphous and crystalline states. As the amorphous GST exhibits less attenuation and thus has a higher optical transmission than its crystalline state, after amorphization the designed device becomes less absorptive, and only slightly changes the intensity of the light pulse. After crystallization the intensity of the passing light is attenuated dramatically as it passes through the

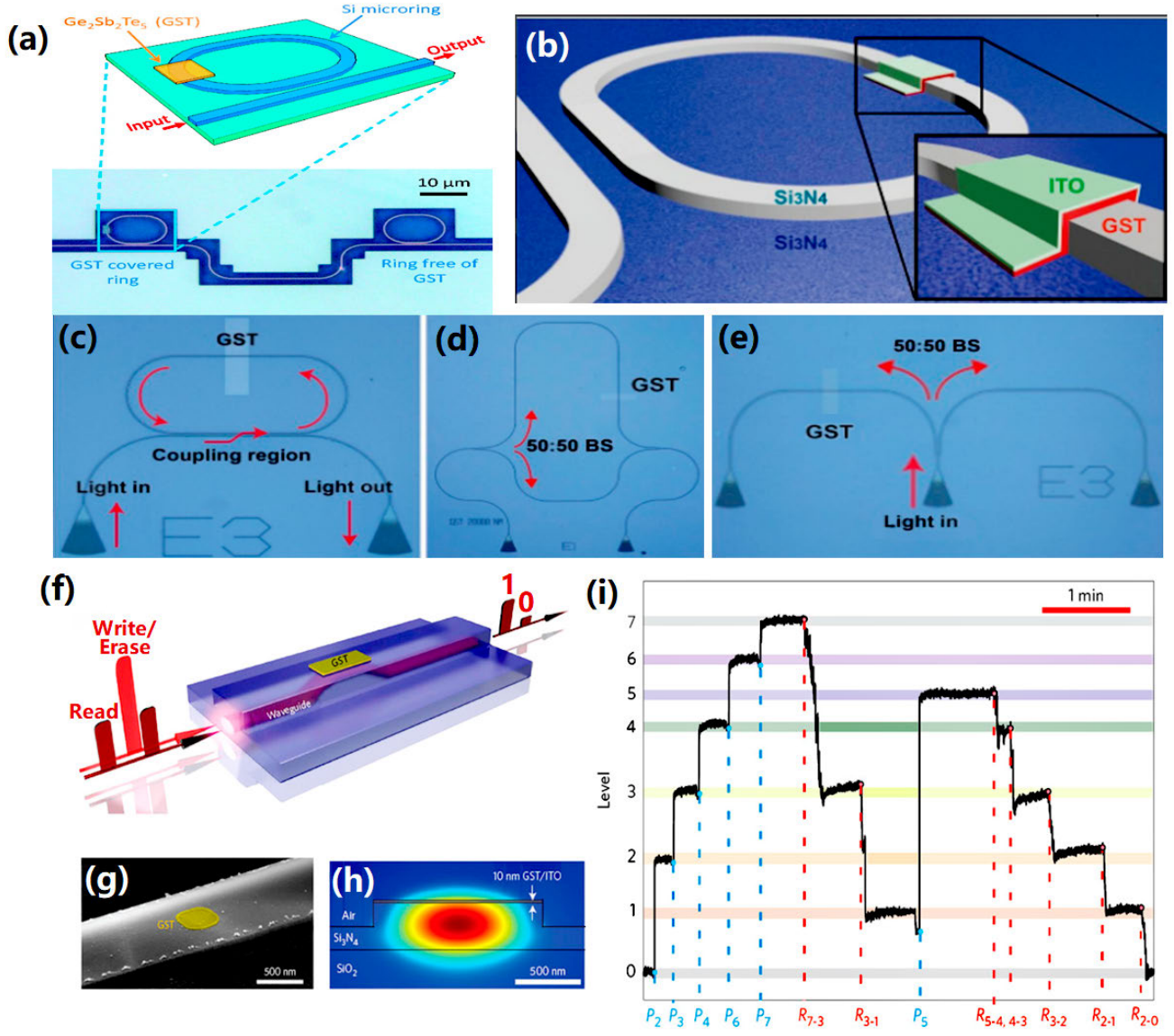

FIGURE 8. (a) Optical microscope image showing the two microrings coupled to a waveguide. The first of them (top) contains the overladding layer of GST. (b) 3D scheme of a hybrid nanophotonic-PCM circuits using partially etched ridge waveguides in Si. (c) Optical microscopy image of an optical race-track resonator with GST switching section. (d) Image of a micro Mach-Zehnder interferometer with a path difference of 200 μm between both arms. (e) Balanced splitters used in the optical properties characterization of GST. (f) Sketch and (g) scanning electron microscopy image of the designed photonic memory having GST on top of a waveguide that can be programmed to set and reset states and subsequently readout as a change in transmission of the waveguide. (h) Simulated field distribution, which shows that the PCM is coupled evanescently to the light in the waveguide. (i) Multi-level switching of eight transmission levels by applying write (P_i) and partial erase (R_{i-j}) pulses. (a) is reprinted with permission from [78]. (b)-(e) are reprinted with permission from [79]. (f)-(i) are reprinted with permission from [80].

device. This makes it possible to sense the phase-transformed region from its background by measuring the transmission coefficient of the hybrid device via a low power optical pulse. This novel phase-change photonic memory has several advantages over its electronic counterparts. Its write and read processes are operated in the near-field, so they are immune to diffraction limits, massively improving the memory's downscalability. Moreover, large arrays of all-optical memory elements can be integrated on nanoscale on-chip waveguides by using a wavelength division multiplexed access (WDM) technique. This allows for ultra-fast all-optical storage with an ultra-low power consumption [84]. Most importantly, novel photonic cells like this enable the multi-level storage, raising the possibility of achieving high density storage [85]. To realize multi-level functionality, the lowest and the highest transmission levels of the photonic device need to be separated by numerous other levels based on a pulse amplitude modulation (PAW) scheme. This can generate up to 8 levels represented by different partially crystalline states (Figure 8(i)), which makes it possible to have various different transmission coefficients in a single optical cell.

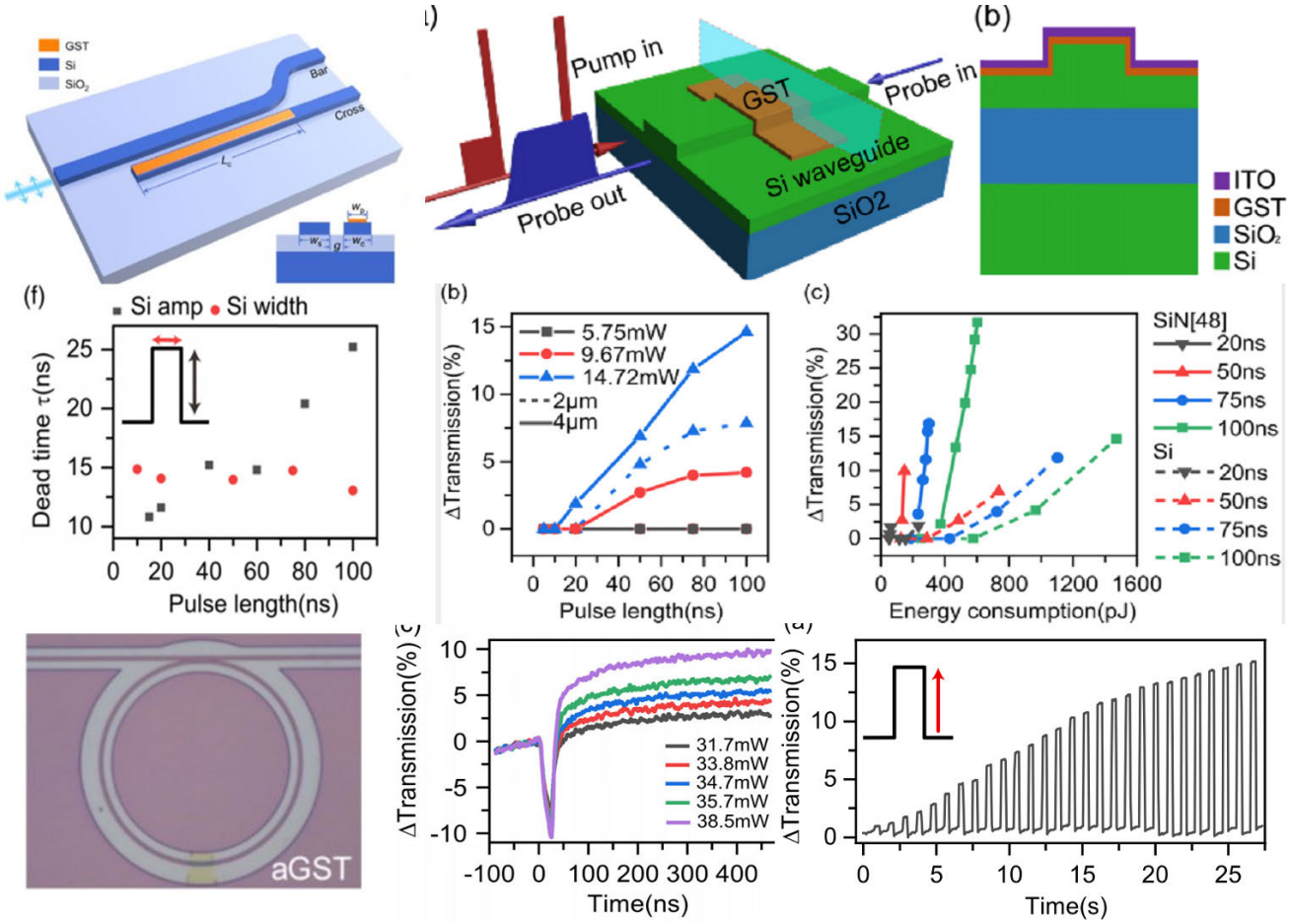

FIGURE 9. (a) Schematic of the switch. (b) 3D overview (left) and cross-sectional (right) view of an Si wavegide phase-change computing cell. (c) Dead time comparison between amplitude amorphization modulation and time width amorphization modulation methods and with SiN devices. (left) and relative transmission changes with the increase of time width of pump pulses from 5 to 100 ns as a comparison between 2 and 4 μm devices separately (right). (d) Comparisoon of energy consumption of Si and SiN devices. (e) Scanning electron microscopic images of amorphous GST on rights. (f) Thermo-optical changes taken with a high-speed photodetector with variation of pump amplitude during amorphizaiton. (g) Independent multilevel states with pulse amplitude modulation during crystallization. (a) is reprinted with permission from [87]. (e) is reprinted with permission from [88]. (b)-(d) and (f)-(g) are reprinted with permission from [89].

A key recent trend in the use of PCMs and nanophtonics is the development of on-chip programmable photonic integrated circuits (PICs) [86]. The work of Fang *et al.* is notable here [87], [88], who have experimented with several different construction techniques relating to silicon PICs, where the Si is doped with GST (Figure. 9(a)) and different forms of heating is used to manage the tunability of the PCM. Their work was originally addressed to the problem of SiN-based PICs having a fairly large footprint and offering relatively low contrast. It is worth noting that Li *et al.* [89] actively compared the relative merits of Si and SiN platforms (Figure. 9(b)) and found that Si is better in relation to its potential for integration with PCMs, its modulation speed and its footprint (Figure. 9(c)), but that SiN is superior in terms of its energy consumption (Figure. 9(d)). Fang *et al.*'s innovation [87], [88] was to introduce GST-clad microring resonators and directional couplers that could be tuned according to the state of the GST (Figure. 9(e)). They also experimented with using two low loss PCMs, Sb_2S_3(SbS) and GeSe, with the electrical actuation of SbS being accomplished on-chip by using an external indium tin oxide (ITO) heater. As mentioned above, basic tuning of the condition of the platform was accomplished by on the one hand achieving amorphization of the GST by means of a single short laser pulse (Figure 9(f)), on the other hand heating the GST to above its crystallization temperature by using a repeated sequence of short laser pulses or a single long pulse (Figure 9(g)). The heat dissipates more quickly in Si than for SiN when applying the same amount of optical power, so short, higher amplitude pulses tend to be more effective for PCMs [89]. By proceeding in this way, Fang *et al.* [87], [88] enabled highly controllable multi-level switching of the microrings by being able to shift the GST to different and intermediate states between its fully amorphous and fully crystalline states, each with different refractive properties (Figure 10(a)). At a

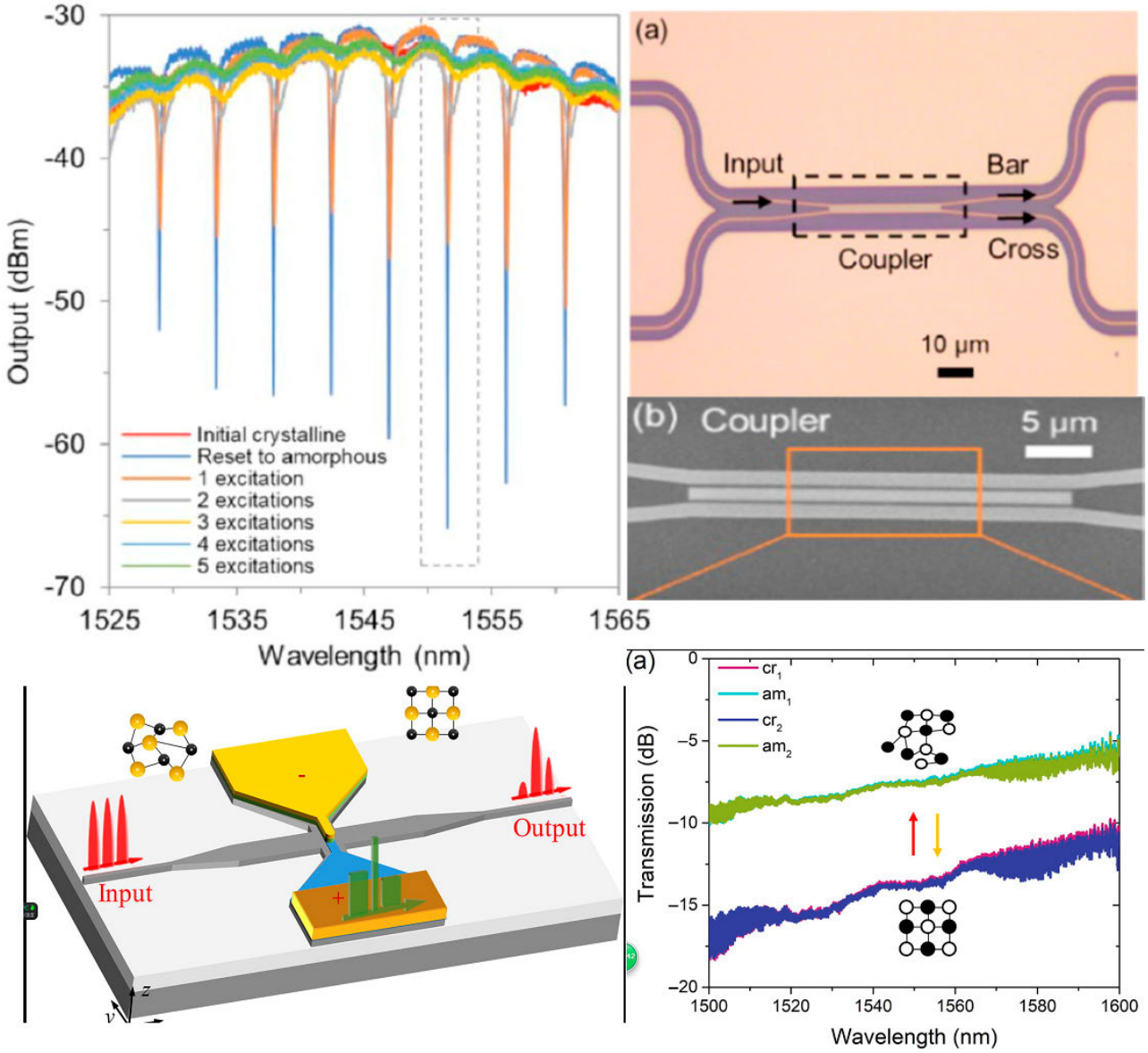

FIGURE 10. (a) Output spectra of a microring with 2 μm GST under different number of excitation. (b) Optical microscope image of the fabricated 2 × 2 switch DC switch (top) and an enlarged view of the coupling regin highlighted by the orange rectangle (bottom). (c) Schematic structure of the GST-loaded Si waveguide. (d) Measured transmission spectra of the waveguide over two phase-change cycles. (a) and (b) are reprinted with permission with [88]. (c) and (d) are reprinted with permission from [90].

transmission rate of 1551.5 nm, this was already able to produce a switching effect that had an extinction ratio of 33 dB. This basic platform was then further refined by adding directional coupler (DC) switches (Figure 10(b)), which consisted of an ordinary silicon (Si) strip waveguide and a hybrid waveguide constructed by placing a thin layer of GST on the silicon. By optimizing the structure of these two waveguides it was possible to control the phase-matching condition for the GST by switching the evanescent coupling of the input TE-polarized light. Others have also noted the potential to dope Si waveguides with PCMs to act as effective heaters because of their attrative thermal conductivity (Figures 10(c) and (d)) [89], [90]. Fang *et al.*'s decision to use ordinary Si waveguides and coat them with GST is important because Si and SiN have very different properties regarding thermal conductivity and heat capacity, with Si having higher thermal conductivity and lower evanescent coupling [89]. Fang *et al.* [87], [88] experimented with using both 1 × 2 DC and a 2 × 2 DC switches. They found that their hybrid platform was able to fully exploit the high optical contrast of the PCM and deliver a small non-volatile overall structure that was low-loss (∼1 dB) and capable of handling broadband operations.

The problem with on-chip optical heating is that the PICs that are currently feasible are limited by the need to route light and are not very scalable [86]. Similar concerns have

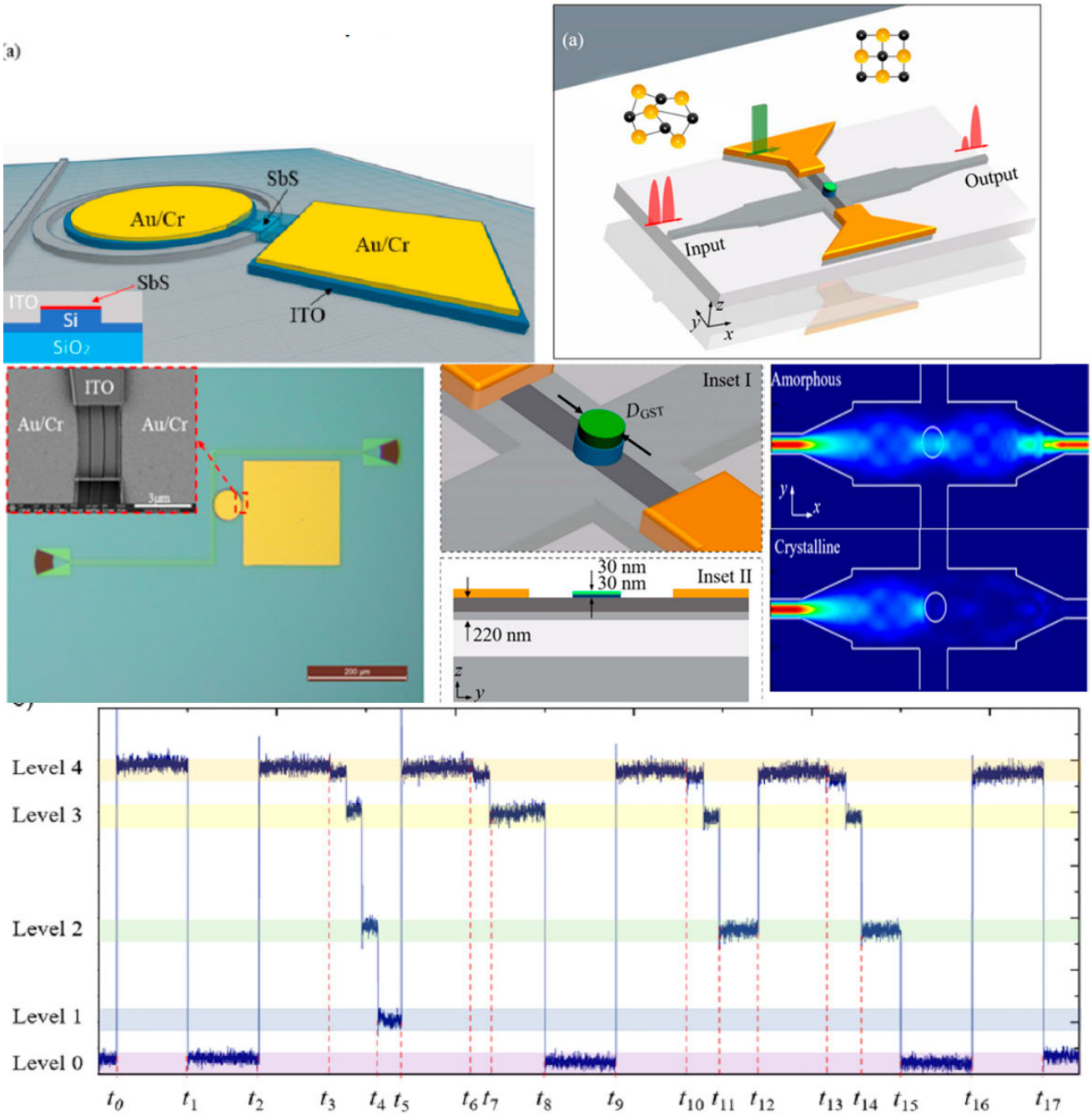

FIGURE 11. (a) Schematic of Si microring modulator integrating SbS and an ITO external heater (top) and the fabricated device (bottom). (b) Schematic of the GST-gated Si MMI switch. (c) Zoom-in view of the active region and the transversal cross-sectional view of the active region. (d) Simulated optical power distributions in the MMI when the GST is in amorphous (top) and crystalline (bottom) states. (e) Multilevel switching of the device with each middle-level corresponding to a partially crystalline state. (a) is reprinted with permission from [88]. (b)-(e) are reprinted with permission from [92].

been expressed about electrical self-heating [86]. There are also potentially high losses from the PCM [91]. By contrast, external local electric heating that can achieve flexible phase transition, is scalable [86], and can deliver extremely fast switching speeds (up to $\sim$ 10 MHz), which is much faster than thermo-optic switching (up to $\sim$ 100 kHz) [88]. At the same time, the amount of energy required to obtain phase transition is only one order of magnitude greater than the thermodynamic limit. Fang *et al.* [88] have therefore also experimented with using local electric heating by placing an ITO external heater on top of a Si PIC doped with the PCM SbS to electrically actuate it (Figure 11(a)). This produced very low loss performance ($\Delta Q < 10$)and large phase modulation ($\Delta\lambda = 0.4$ nm) on microrings clad with just 8 μm

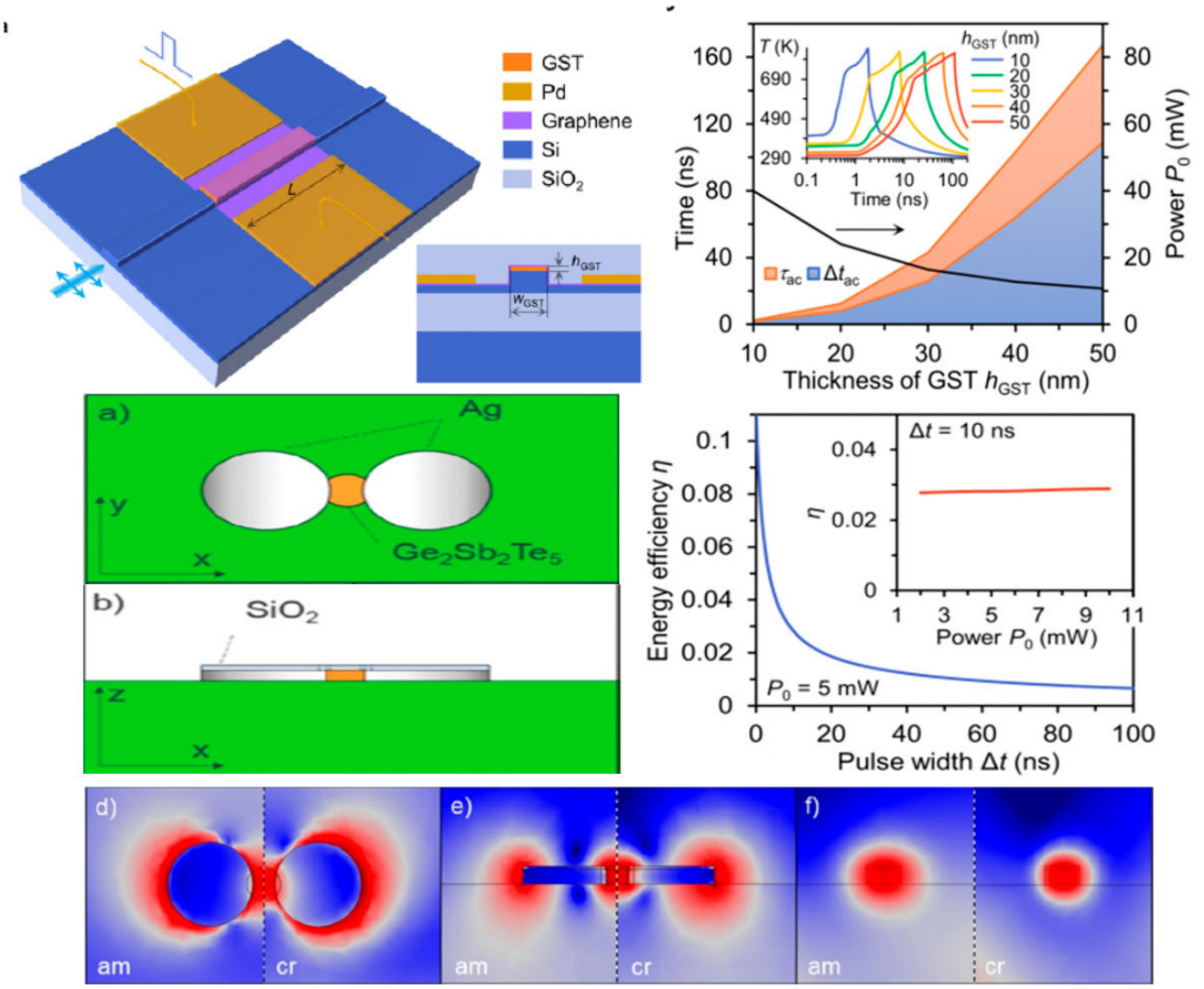

FIGURE 12. (a) Schematic of the proposed PINC with a grapheme heater. The two ports of the PINC are connected with regular Si rib waveguides in this case. (b) Area chart of the minimum pulse width (Δt_{ac}) and corresponding dead time (τ_{ac}) required to achieve complete crystallization actuated by the maximum allowed pulse power (black line) as a function of GST thickness. (c) Energy efficiency (η) as a function of pulse width. (d) Cross sections of the photonic memory across xy (top) and xz (bottom) planes, respectively; each plane cuts the plasmonic nanoantenna at its center. (e) Log10 of electric field norm due to TE propagating waveguide model of 1 mW power (figures depict the electric field at room temperature for amorphous (left) and crystalline (right) states of the GST cell). (a)-(c) are reprinted with permissions from [86]. (d) and (e) are reprinted with permissions from [94].

of SbS. Zhang *et al.* [92] have also experimented with using an ITO-related heater to induce the electrical switching of GST. In their design, an optical memristive switch in the form of a silicon multimode interferometer (MMI) had a small circular piece of GST placed at its center. The piece of GST was then covered by an ITO film (Figures 11(b) and (c)). A non-volatile phase transition was induced in the GST by an electrical pulse (Figure 11(d)). To induce amorphization, a high-voltage pulse was applied to melt the GST, which then cooled rapidly. This was treated as the Write pulse. To crystallize the GST, a medium-voltage pulse was applied for long enough to restore the GST's atomic order. This was treated as the Erase pulse. The light propagation across the MMI was calculated by means of an FDTD simulation to assess the state of the switch. Experimental testing showed that a transmission contrast in excess of 20 dB can be achieved for a wavelength in the range of 1500 to 1600 nm. Both binary-level and multi-level switching was found to be possible at very low levels of power consumption using this kind of device (Figure 11(e)).

To tackle the fact that the energy consumption of external electric heaters is greater than it is for purely optical heaters, Zheng *et al.* [86] have experimented with using graphene heaters on programmable GST-on-Si platforms. Graphene has an extremely low heat capacity and very high in-plane thermal conductivity. A graphene heater consists of a layer of carbon atoms constructed as a honeycomb lattice [93]. In Zheng *et al.*'s study [86], a GST-on-Si hybrid phase-change

integrated nanophotonic cell (PINC) was conformally covered with a graphene monolayer with palladium contacts. This was capped by a layer of SiO_2 (Figure 12(a)). The response of the PINC was then tested according to the application of different width electrical pulses. As a consequence, Zheng *et al.* [86] were able to obtain a switching speed of ∼80 MHz (Figure 12(b)) and achieve full phase transitions with an energy efficiency of 19.2 aJ/nm^3 (Figure 12(c)). The attenuation was ∼6.46 dB/μm and the optical phase modulation was ∼0.28 p/μm at 1550 nm. In comparative testing this was found to be substantially superior to the performance of comparable ITO and Si p-i-n heaters.

A different approach that has been adopted recently by some researchers is to not shift to external local heaters such as the ITO and graphene ones described above but rather to concentrate on staying in the optical domain and improving the light-matter interactions instead [94], [95]. This offers advantages in terms of speed and energy consumption because it obviates the need to undertake opto-electrical conversions. A promising direction being taken here is the development of plasmonic enhancement of the optical field and how it interacts with PCMs. Basically, this involves generating a resonant interaction between light and the free electrons at the interface between some kind of metal and the PCM, creating heat and producing a phase transition. In relation to this, Gemo *et al.* [94] have experimented with creating a plasmonic dimer nanoantenna. This consists of two Ag nanodiscs placed on top of a SiN waveguide, with GST deposited in the gap between the two discs (Figure 12(d)). By coupling with the optical mode propagated in the waveguide, the nanoatenna is able to maintain a localized plasmonic resonance that enhances the electric field in the gap, thus magnifying the interaction between the light and the PCM (Figure 12(e)). This can then reduce the energy required to promote an effective phase-transition while significantly augmenting the switching speed, making the device ideal for memory applications. As with many other uses of PCM in memory applications, a single high-power pulse of light is used to transition the GST to its amorphous state, which is treated as a write to memory operation. To achieve recrystallization of the GST for the erase operation, a short high-power pulse is followed straight away by a second longer pulse of linearly decreasing power. This strategy offsets the risk of re-amorphization. Simulations suggest that this device is capable of write-erase speeds of between 2 and 20 ns and an energy consumption per operation of between 2 and 15 pJ. A similar strategy, but using two electrodes principally manufactured out of Au, was adopted by Farmakidis *et al.* [95]. In their case, the GST bridging the gap between the electrodes is capped with SiO_2 and either electrical or optical pulses can be used to switch the phase of the GST. In the optical domain, piecewise optical write pulses and rectangular erase pulses are used to control the state of the GST. In the electrical domain, the write and erase pulses are sent via the RF port of a bias tee. Here, a 10 ns, 350 mV pulse is used to induce the GST's amorphous phase as a write operation, and a 350 mV triangular pulse is used to re-crystallize it for the erase operation. By allowing for both electrical and optical programming this device is able to provide for multi-level mixed mode operations.

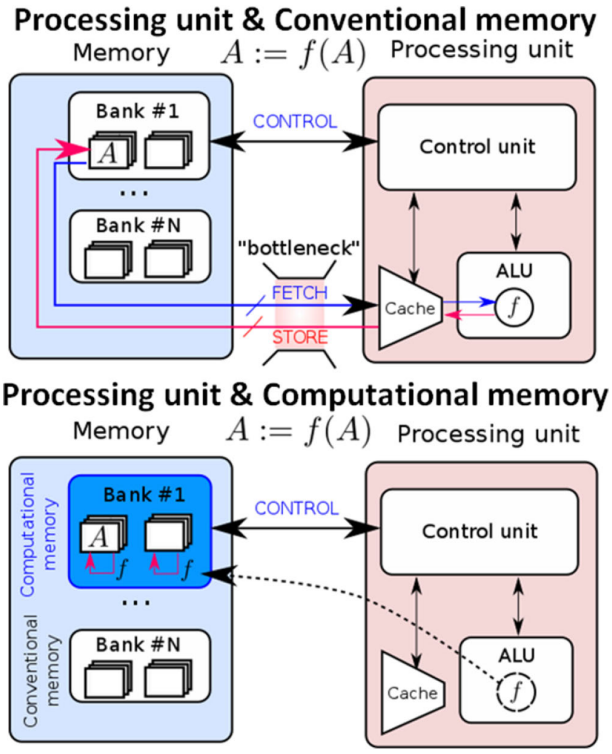

FIGURE 13. Schematic illustration of the concept of 'computational' memory. If data, A, is stored in a computational memory unit and it is required to perform an operation, then it is not necessary to transfer the data, A, to a processing unit and back. The operation is performed in place in the computational memory unit by exploiting the physical attributes of the memory devices. Reproduced from [96].

C. ON-CHIP COMPUTATIONAL MEMORY

The novel concept of 'computational' memory has attracted a lot of attention recently. It refers to the ability to simultaneously store and process data in the same place [96], as shown schematically in Figure 13. Currently, conventional digital computers usually adopts what is known as the von Neumann mode of operation where data is stored in the memory and executed in the CPU. As a result, digital data stored in the memory needs to be retrieved by the CPU prior to processing it and, after processing, the CPU has to transfer the data back to the memory. This back and forth data transfer of data between the CPU and the memory obviously results in extra energy consumption and diminishes a computer's energy efficiency. Additionally, the transfer rate of the data bus that connects the CPU with the memory is much slower than that of the CPU itself, and seriously restricts the processing speed of the modern computers. Hence, the appeal of computational memory, because it offers the possibility of overcoming the von Neumann bottleneck and creating innovative the future computer architectures.

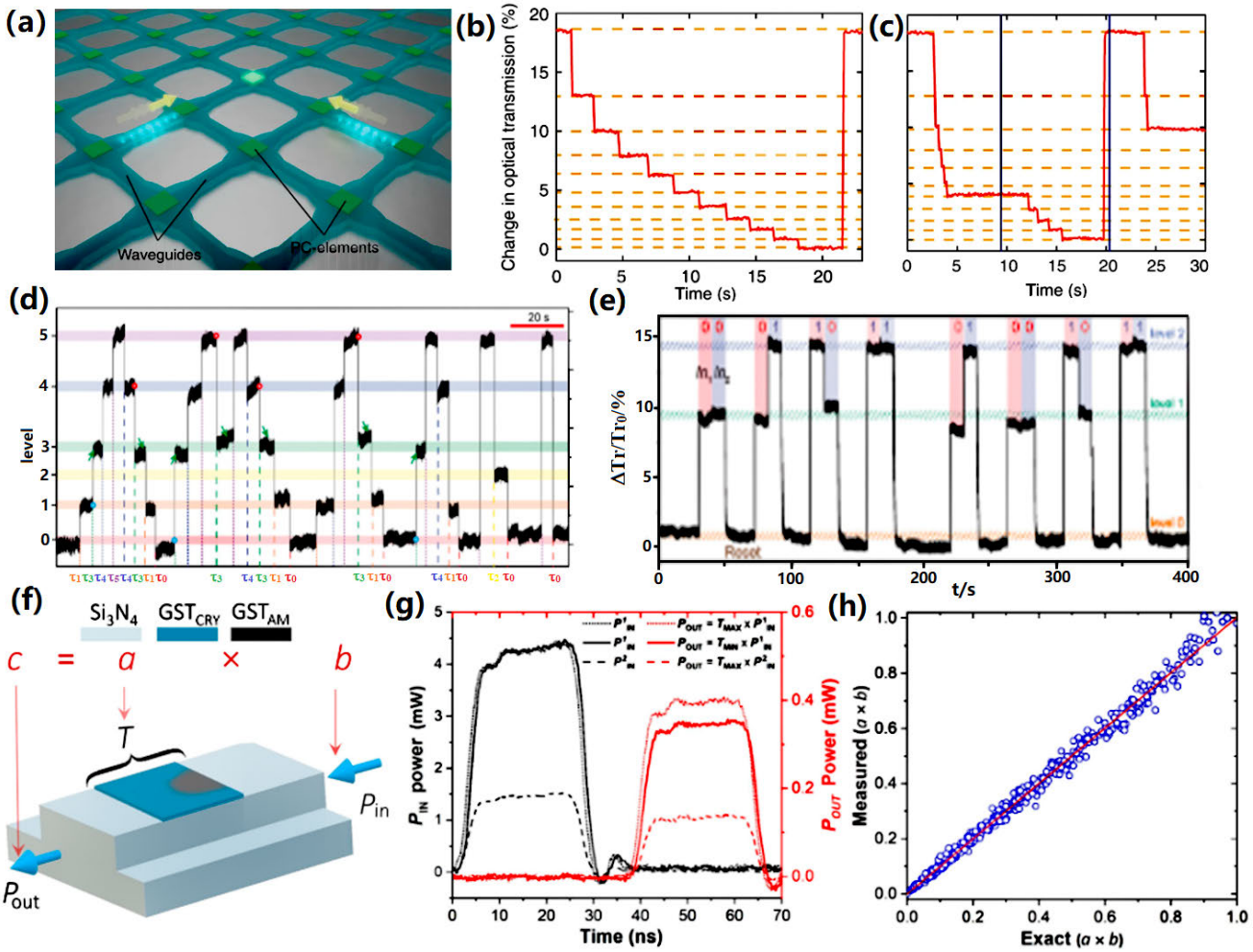

FIGURE 14. (a) Sketch of a waveguide crossing array illustrating the two-pulse addressing of individual phase-change cells. Only overlapping pulses provide sufficient power to switch a desired PCM-cell. (b) Level definition: Before using a phase-change cell, the levels for the chosen base of operation have to be defined. Therefore the pulse energies are set in such a way that clearly distinguishable and repeatedly accessible levels are obtained. In this example each step downwards consists of a group of five ps pulses, the reset pulse of a group of ten ps pulses. (c) Addition: with the transmission levels defined, '6 + 6 = 12' is calculated. By analogy to the operation of an abacus, a carryover is performed when the tenth level is reached and the cell is reset to its initial state. The result '12' is obtained from one carryover and the final state of the PCM-cell, which is at level 2. (d) Random access of six different levels of a single photonic memory with ΔTr/Tr recorded. A multiple-identical-pulse train is used to reach different levels, with N = 12, p = 20 ns, and P_{peak} = 1.6 mW. Each level can be reached with the same pulse train at a determined width (τ to τ_5) from any previous level, where τ = 10 ns, τ_1 = 10.5 ns, τ_2 = 11 ns, τ_3 = 11.5 ns, τ_4 = 12.5 ns, and τ_5 = 15 ns, respectively. (e) Transmission change of the photonic memory with different input digital encoded signals. Three distinct levels '' (orange),'1' (green), and '2' (blue) were accessed by reset, digit 0, and digit 1, respectively. (f) Scheme of the multiplication of two scalars a and b, codified in the device transmittance T and in the energy of the read pulse P_{in}. (g) Demonstration of three multiplications by applying two different P_{in}, P^1_{in} = 112.8 pJ (~4.51 mW for 25 ns) and P^2_{in} = 38.9 pJ (~1.56 mW for 25 ns), to memories programmed in the maximum and minimum transmittance levels, ΔT = 0.143 and ΔT = 0, respectively. (h) Realization of 429, c = a × b multiplications equivalent to 13 different, equally spaced, values for T, thus creating 13 values for the multiplicand a, and 33 different values for P_{in} ∈ [0 pJ, 112.8 pJ] for 33 scalars corresponding to b (note: a, b, c ∈ [0, 1]). (a)-(c) are reprinted with permission from [91]; (d)-(e) are reprinted with permission from [98]; (f)-(h) are reprinted with permission from [99].

The majority of the PCM-based computational memories function electronically, depending on the vast contrast in electrical resistivities contrast between the PCM's amorphous and crystalline states [96], [97]. The aforementioned photonic devices exhibit analogous storage behavior to their electronic counterparts, so the feasibility of developing a PCM-based photonic computational memory is an intriguing prospect that is beginning to attract considerable amounts of research. The success or otherwise of photonic computational memory depends to a great extent upon the effectiveness of the arithmetic and logical computations inside the device itself. One possible scheme for performing arithmetic calculation is to implement a rectangular waveguide array with a PCM-cell deposited at every waveguide crossing point [91], enabling the selective addressing and manipulation of each of these basic arithmetic units, as illustrated in Figure 14(a). To perform a basic-10 arithmetic calculation, the degree of crystallization in each PCM cell can be divided stepwise into 10 different levels by using a group of identical picosecond (ps) pulses. It can then be re-amorphized using a group of picojoule pulses, as shown in Figure 14(b). Taking the example of the base-10 addition of '6+6', the amorphous

PCM cell was first set so as to crystallize level 6 through appropriate pulse configurations, corresponding to the first summand. The second summand was subsequently added into the PCM cell in terms of the corresponding pulses. When the 10^{th} level was reached, the PCM cell was reset (i.e., reamorphized) to level 0 (i.e., the initial state) before the rest of the pulses were applied. It should be pointed out that while resetting the cell, one pulse sequence was applied to a second PCM cell that was denoted as the next highest order multiple of the base to store the carryover information. The rest of the pulse sequence for the second summand then drove the PCM cell to crystallize level 2, with the second PCM cell being set at level 1 due to the previous carryover of 1. This results in the answer of '12'. Such a strategy, as shown in Figure 14(c), was recently employed to achieve logic functions on the same photonic device, while replacing the conventional PAM by a novel pulse width modulation (PWM) scheme [98]. In contrast to PAM, where there is a fixed width and different amplitudes, PWM makes use of optical pulses with a fixed peak amplitude and different widths. Various phase-transformation levels can therefore be enabled by using different pulse widths, as demonstrated in Figure 14(d). The most exciting feature of PWM is its ability to directly access a particular memory level (i.e., phase-transformation level) from any other memory level using the same PWM pulse sequence (i.e., one stored level only correlates to one particular PWM sequence that then induces that memory level to be written, whatever the starting state) [98]. The resulting random accessibility from PWM reveals the logic functionality of the photonic device by utilizing a double pulse train of the fixed time separation and peak power, but with three different pulse widths, corresponding to digital inputs 0, 1, and reset, respectively. The device transmission was measured after two input signals with different combinations were applied to a photonic memory, followed by a reset signal. The PCM cell was initially set in the crystalline state, and digital inputs of '0' and '1' resulted in different relative changes in transmission that was reset back to the pristine state by the reset signal. In this case, combining different input signals (such as '00', '01', '10', and '11') allows for several relative changes in transmission with distinguishable values and shapes (Figure 14(e)), which can determine the digital output of the photonic memory (i.e., '0' or '1') by comparing the peak amplitude of the relative change in transmission with a pre-defined threshold value. Triggered by above progress, the first instance of a photonic computational memory for direct scalar multiplications of two numbers, using a single integrated PCM-based photonic cell, was demonstrated [99], as illustrated in Figures 14(f)-(h). To perform scalar multiplication, one write pulse, P_{write}, was used to program the device to a particular transmittance (T) level, and another readout pulse with lower intensity, P_{in}, was subsequently implemented to sense the device transmittance previously induced by the pulse P_{write} without changing the phase-transformation extent of the PCM. The power of the pulse of P_{in} at the output port, $P_{out} = T(P_{write}) \times P_{in}$, is the outcome of the multiplication a $\times$ b by mapping the multiplicand a to T and the multiplier b to P_{in}. Measured values of 429 multiplications choosing arbitrary values, obtained from this method, were demonstrated to show a good match with the exact values of the multiplication, as illustrated in Figure 14(h). Such findings not only establish the potential of PCMs in photonic hardware, but also verify the possibility of combining integrated optics with collocated data storage and processing to enable all photonic in-memory computations.

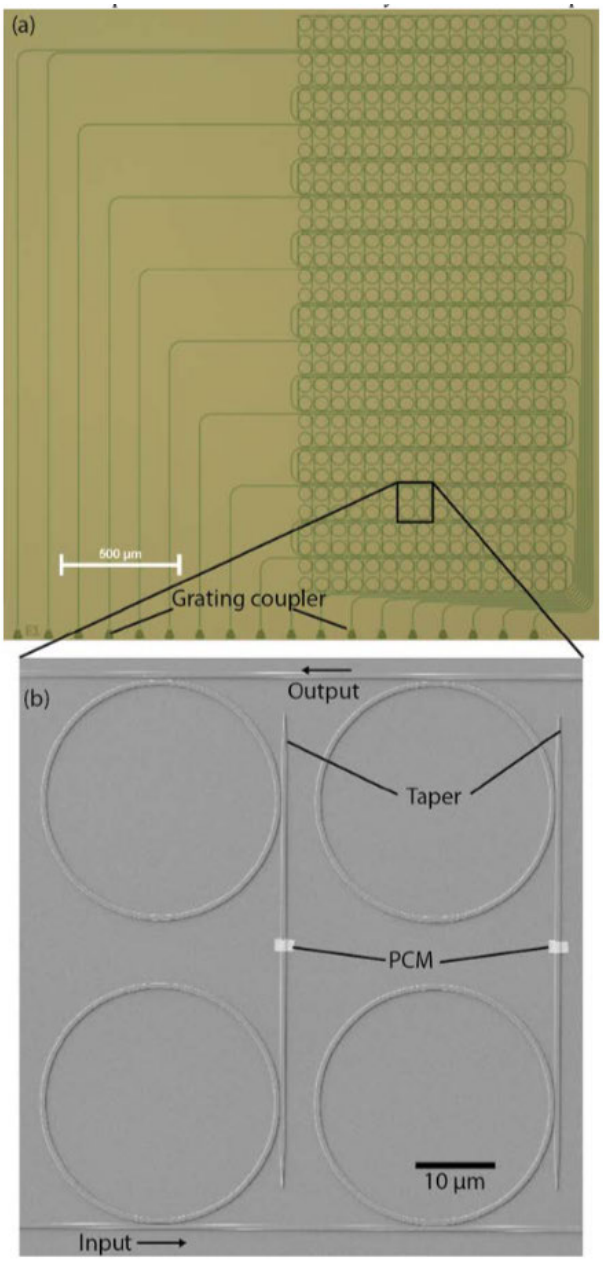

FIGURE 15. 16 × 16 cell photonic matrix memory, (a) Optical micrograph of the memory cells. (b) SEM of a single cell within the array. Reprinted with permission from [100].

Some recent research has been addressed to trying to solve the problem of making all-photonic memory circuits

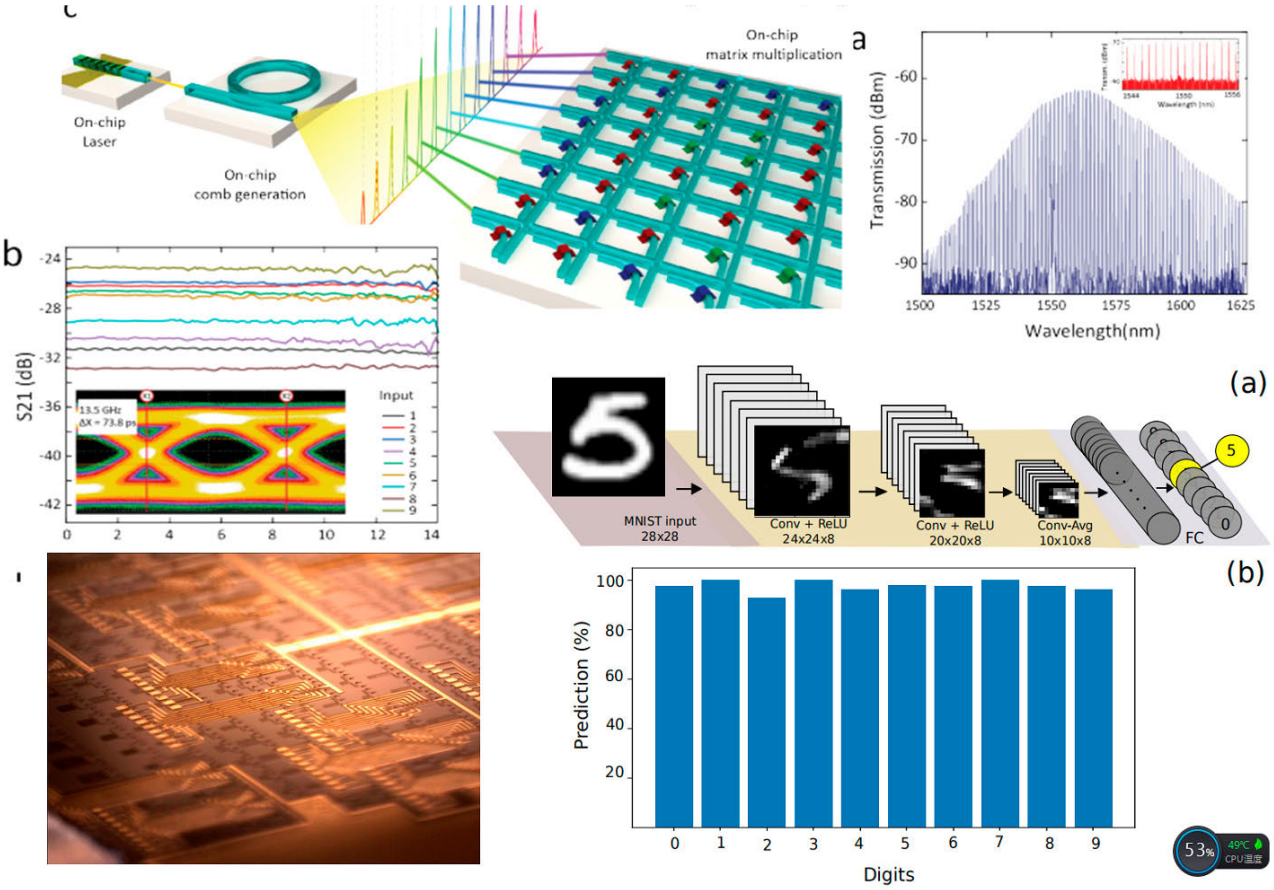

FIGURE 16. (a) Conceptual illustration of a fully integrated photonic architecture to compute convolution operations. An on-chip laser (not used) pumps an integrated SiN solution microcomb to generate a broadband frequency comb. Individual comb teeth which form the input vectors are modulated at high speeds, multiplied with a matrix of non-volatile phase-change memory cells, and summed along each column on a photodetector. (b) Transmission spectrum of the coherent soliton frequency comb through the device. Inset: spectrum of the 16 selected comb lines used in the experiment. (c) Modulation bandwidth of all comb lines, showing modulation rates up to 14 GHz. Inset: open eye diagram at 13.5 GHz. (d) Picture of a silicon photonic B & W neural network platform. (e) An illustrative block diagram of the two-layers DEAP CNN solving MNIST (top), and results of the MNIST task using a simulated DEAP CNN with an overall accuracy of 97.6% (bottom). (a)–(c) are reprinted with permission from [101]. (d) is reprinted with permission from [103]. (e) is reprinted with permission from [102].

scalable. In relation to this, Feldmann *et al.* [100] have developed a 256 cell all-photonic phase-change memory that can store 512 bits of data. The data is stored in an array of nanoscale PCM-based devices. In a move redolent of the work by Fang *et al.* [87], [88] discussed in section 3.2, Feldmann *et al.* [99] based their memory array upon rows of microring resonators, each of which are connected to a single input waveguide. Every row also contains a certain number of memory cells that each consist of an input and output waveguide, joined by two microring resonators and with a waveguide with a PCM-patch on top. When light passes through the input waveguide, some of it is coupled to the lower microring resonator and the PCM waveguide. Once the light has passed through the PCM and induced as phase-transition, it is guided to the second microring resonator. The input wavelength directed to the PCM can be adjusted by tuning the radius of the microring resonators. Importantly, both of the resonators have the same radius and, thus, the same resonance wavelength. This makes it possible to multiplex and demultiplex the same input signal. The amount of light going to the PCM and output waveguide is controlled by adjusting the gaps between the resonators and the waveguides. The PCM cell between the resonators works as the actual data storage component, with its exact content depending upon the ratio between the crystalline and amorphous parts within it. The design was tested using SiN-based waveguides and resonators with GST as the PCM, topped with a protective ITO layer. The 16×16 element device had 256 separate PCM elements (Figure 15) and managed to store a 16×16 pixel pictogram of a floppy disk in two-bit resolution. The 2-bit resolution allowed for 4 color values to be assigned to each PCM-cell. All of the cells could be addressed individually and were able to reproduce the pictogram with a high degree of accuracy. The overall footprint of the device was 1000×2400 μm2.

It should be also noticed that the conventional optically computing approaches have severely been limited by a lack of integrated non-volatile photonic memory and a lack of

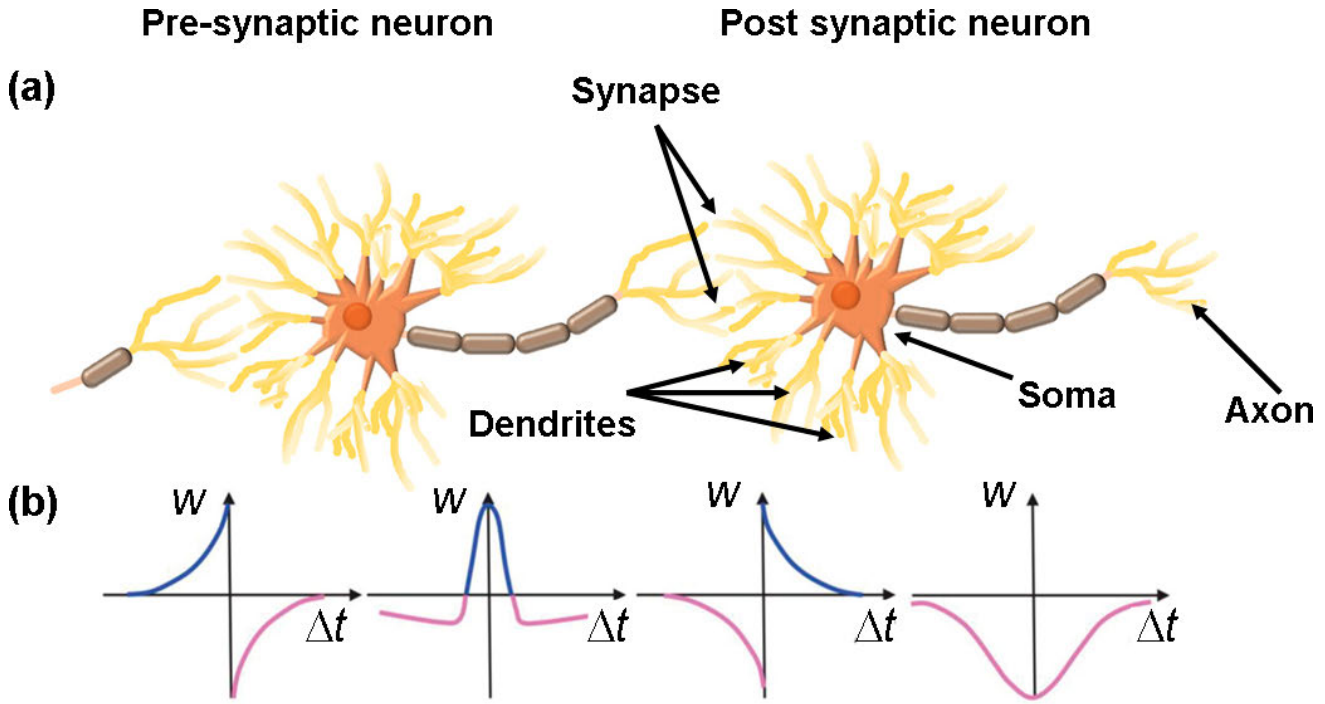

FIGURE 17. (a) Neuron structure in human brain and (b) example of STDP desired weight change based on the time different between two neighboring neurons. Updated and reprinted with permission from [106].

multiplexing capability for such calculations. This can be excitingly alleviated by devising a computational specific integrated photonic tensor core that consists of phase-change memory arrays to locally store convolution kernels on-chip, and photonic chip-based frequency combs that enables true in-memory photonic computing using wavelength division multiplexing (WDM) capability (Figure 16(a)) [101]. As the calculation is performed by measuring the optical transmission of reconfigurable and non-resonant (Figure 16(b)), i.e., broadband, passive components operation at a bandwidth exceeding 14 GHz (Figure 16(c)), the designed photonic core exhibits the computational potential at the speed of light at very low power, thus providing an effective method to remove the computing bottleneck in machine learning hardware for applications ranging from live video processing to autonomous driving and Ai-aided life saving applications. In addition to above findings, Prucnal *et al.* [102]–[104] also proposed a photonic network, i.e., digital electronics and analogue photonics (DEAP), suited for convolutional neural networks based on silicon photonics technologies (Figure 16(d)). DEAP was estimated to perform convolutions between 2.8 and 14 × faster than a GPU while roughly using 25% less energy. Its capability of computing a convolution and solving MNIST handwritten recognition task with an overall accuracy of 97.6% was also demonstrated (Figure (e)). Such silicon photonics-based computing memory has the advantages to simultaneously outperform conventional electronic hardware for convolutions and have the ability to scale up in the future.

IV. PHASE-CHANGE PHOTONIC NEURONETWORK

Another emerging hotspot of PCMs stems from its applications for brain-inspired neural network. Creating artificial neural networks (ANNs) to make machine completely think and action like biological brain is the ultimate dream of human society. However, due to the well-known von Neumann bottleneck, the computational performances of the most advanced digital computers today still can not compete with human brain that exhibits a superior capability of in-memory computing [105]. The prerequisite of thoroughly mimicking the human brain is to understand its structure as well as biological response. Human brain is mainly composed of 10^{11} neurons and 10^{15} synapses [106], [107], as illustrated in Figure 17(a). One neuron was reported to have a soma, an axon and dendrites. Soma, considered as the main body of the neuron, is connected to neighboring neurons via axon and dendrites. Axon is responsible for information output, while dendrites act to receive signals from neighboring neurons. Synapse is defined as the interfacial region between the axon of the previous neuron and the dendrites of the next neuron. The connection strength between two neighboring neurons is denoted as 'synaptic weight' that can be potentiated or depressed through the adjustment of synaptic plasticity [108]. The change of synaptic plasticity that can last a long period is named long-term plasticity that usually pertains to learning and memory, whereas the change of synaptic plasticity that only lasts a short time is called short-term plasticity [109]. The most famous mechanism that governs long-term plasticity is

spike-timing-dependent-plasticity (STDP), as shown in Figure 17(b). According to the STDP theory, the relative spiking time represented by the time difference between presynaptic spike and postsynaptic spike, directly determines long-term plasticity [110]. On one hand, the long-term plasticity is potentiated (i.e., long-term potentiation (LTP)) when the presynaptic spike precedes the postsynaptic spike. On the other hand, the event that presynaptic spike lags the postsynaptic case can depress the long-term plasticity (i.e., long-term depression (LTD)). Hence, large amount of efforts have recently been devoted to the emulation of biological STDP response using emerging non-volatile memories, such as PCRAM, in an electronic manner [22], [111], [112]. This is mainly because the electrical resistivity of the PCMs can be readily modulated by applied electric pulses, closely similar to the change of synaptic weight. This naturally implies that the photonic phase-change memory elucidated in Section 3 also exhibits the potential of being artificial synapse whose weight can be interpreted as the device transmission.

One innovative scheme to realize the optical synapse is to utilize a tapered waveguide structure with the discrete GST islands capped by ITO films [113], as depicted in Figures 18(a) and (b). The optical transmission of the device with the crystalline GST as the pristine state was defined as the baseline of the readout and assigned to a synaptic weight '0'. The change of the synaptic weight is therefore regarded as any subsequent change of the readout during the measurement relative to the baseline, and can be achieved by sending fixed-duration, fixed-energy optical pulses down the waveguide. Hence, any arbitrary synaptic weight level can be secured using a set of known pulses without the requirement to notice the current actual weight. To imitate the STDP behavior, the presynaptic signal is split into two beams with 50% coupled into a photonic synapse, as explained by Figure 18((c), and the other 50% (P_{in1}) is connected to an interferometer via a phase modulator. The postsynaptic signal is also separated into two parts, with 50% transmitted and the remainder (P_{in2}) fed back to the interferometer. Changing the phase modulator enables to tune the net output power of the interferometer between 0 and $P_{in1}+ P_{in2}$, which is implemented to update the synapse weight. The pulse widths and repetition rates of pre- and postsynaptic signals are intentionally set differently. It is clearly indicated that the net output power from the interferometer applied to the synapse has a single pulse larger than the threshold power for switching PCMs in the case of no time delay between pre- and postsynaptic spikes. Increasing the time delay between pre- and postsynaptic spikes leads to different numbers of pulses above the threshold switching power being sent to the synapse, as demonstrated in Figure 18(d). This results in the required exponential dependence of the synaptic weight change on the time delay, thus allowing for the imitation of the STDP behavior in a simple and effective manner.

Another route towards optical synapse using PCMs is to build a Si-on-insulator structure comprising a rectangular waveguide and a ring waveguide [114], as shown in Figure 18(e). A GST element is deposited on one arm of the ring waveguide, which takes the shape of an arc, where the length of the arc is denoted as the length of the GST element. Waves in the rectangular waveguide are partially coupled to the ring and constructively interfere when the round-trip phase shift equals an integer multiple of 2π, defined as the resonant condition. The synaptic functionality is achieved in a way that the output power is given by the product of the transmission at resonant wavelength and the power of an incident optical pulse. The synaptic weight is thus expressed in form of the transmission at resonant wavelength, which can be tailored by changing the degree of crystallization states of the GST element. Note that although the individual synapses indicate a simple multiplication, the weighted inputs from multiple synapses are received by a neuron. To simulate the integrate-and-fire behavior of biological neuron, two add-drop ring resonators with the GST deposited on top of each is considered as the 'integration unit' of the neuron [114], [115]. In this case, two ring resonators are fed by positive and negative weighted sums, respectively, from the synapses to implement integration in the appropriate direction. The GST on ring resonators is initially set in the crystalline state, and can be partially amorphized by the incident 'write' pulses. During the read operation, transmission at the 'drop' port increase, while decreasing at the 'through' port of each ring resonator. This leads to the positive and negative integration of transmission through the 'drop' and 'through' ports, respectively, whereby these properties of the device can be combined to mimic the behavior of a bipolar integrate-and-fire neuron, as illustrated in Figure 18(f).

Enlightened by the successful emulation of the biological synapses and neurons using phase-change photonic memories, a fully optical, integrated and scalable neuromorphic framework for implementing spiking neural networks using PCMs was most recently demonstrated [116]. Such a network, as shown in Figure 19(a), consists of 4 artificial neurons and 60 synapse, arranged in a manner that one neuron has 15 synapses. The synapses are built of optical waveguides and weighting is achieved via PCM cells integrated on top of the waveguides. A multiplexer consisting of ring resonators is implemented to combine the light pulses onto one waveguide and guide it to the on-chip neuron soma. The learning capability of such hardware using both supervised and unsupervised machine learning algorithm was tested by feeding the network with information in the from of light pulses. This optical network after training process is ultimately able, on the basis of given light patterns, to recognize a pattern (i.e., four consecutive letters) being sought (Figure 19 (b)). As the system functions solely with light rather than electrons, it can process data much faster than traditional artificial systems.

V. PHASE-CHANGE METASURFACES

'Metamaterials' are artificial media that are constructed by carefully designing the unit structure on a sub-wavelength scale [117]. Due to their exotic structure, metamaterials exhibit several unique optical properties that cannot be

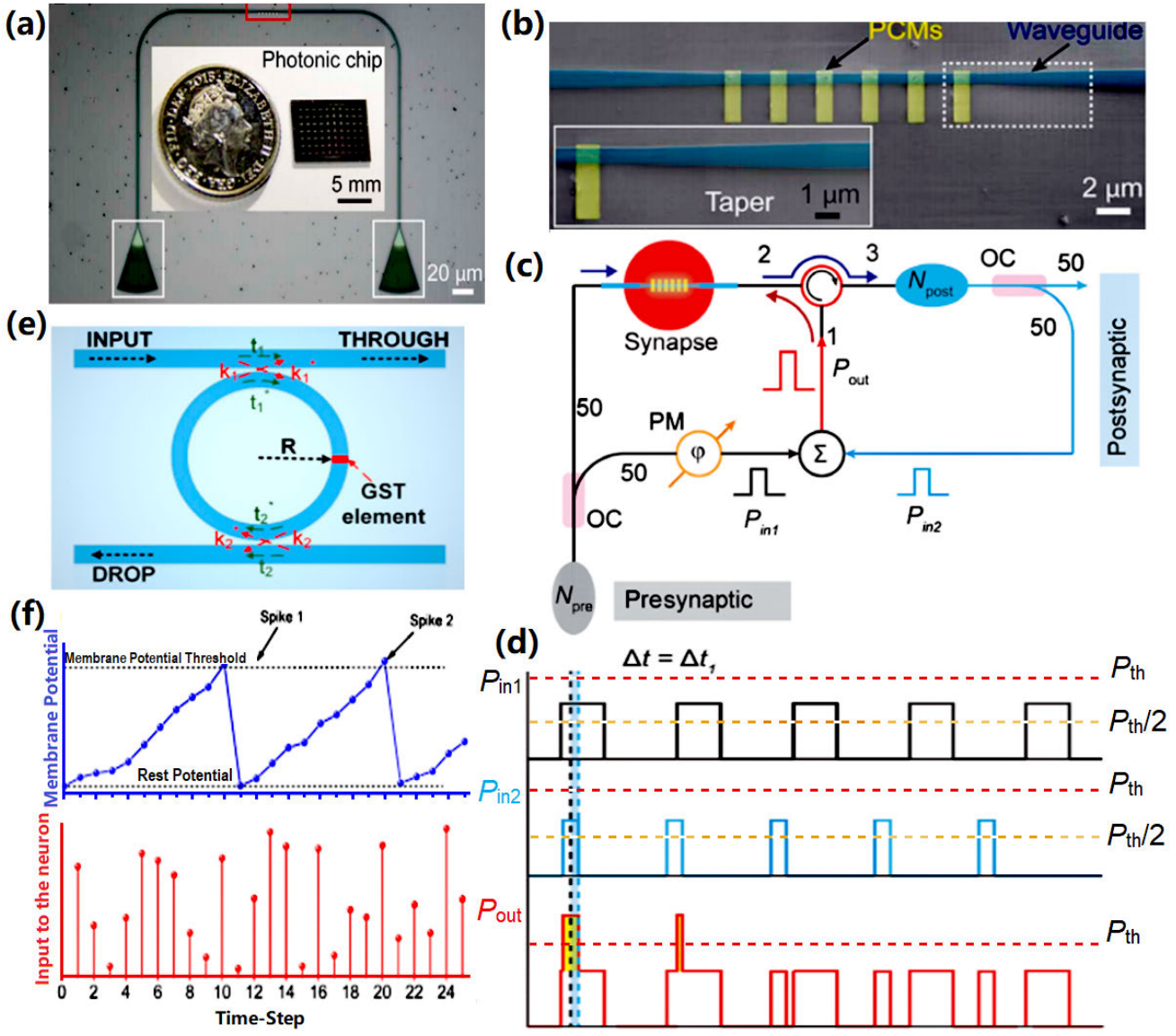

FIGURE 18. (a) Optical microscope image of a device with the active region (red box) as the photonic synapse. The optical input to and output from the device are via apodized diffraction couplers (white boxes). Inset: A typical photonic chip containing 70 photonic synapses has a dimension smaller than a 5-pence coin. (b) Scanning electron microscope image of the active region of the photonic synapse corresponding to the red box in (a) with six GST units on top of the waveguide. Inset: The zoomed-in tapered structure of the waveguide highlighted by the white dashed box. (c) Schematic of the all-optical method using a photonic synapse to achieve the STDP plasticity. Split with an optical coupler, 50% of the presynaptic signal is connected to one input (P_{in1}) of an interferometer via a phase modulator. Similarly, 50% of the postsynaptic signal is connected to the other input (P_{in2}) of the interferometer. The output signal (P_{out}) of the interferometer is used to update the synaptic weight. N_{pre} and N_{post} are pre- and postsynaptic neurons, respectively. (d) The time delay between pre- and postsynaptic signals is increased to Δt_1, leading to a net pulse above the threshold switching power (P_{th}) being sent to the synapse. (e) A two-dimensional top view of the ring resonator illustrating the input, output, coupling and transmission parameters. (f) The behavior of the proposed integrate-and-fire neuron in the simulated SNN showing the variation of the membrane potential under the action of incident pulses thus showing integrate and firing action.(a)-(d) are updated and reprinted with permission from [113]; (e)-(f) are reprinted with permission from [114].

found in natural optical materials. These include a negative refractive index [118] and an extremely large artificial chirality [119]. However, conventional metal components embedded in three-dimensional (3D) structured metamaterials adversely induce enormous amounts of loss, thus making metamaterials unsuitable for applications with a high efficiency requirement. This has triggered interest in two-dimensional versions of metamaterials, also known as 'metasurfaces' [120]–[122]. Metasurfaces where light does not need to have a deep penetration, such as flat lens [123] and polarization control [124], have demonstrated excellent optical functionality. A severe drawback of conventional metasurfaces is being able to maintain their optical performance. To this end, researchers have started to explore how to develop tuneable metasurfaces, where their optical responses can be actively manipulated by external excitations. PCMs

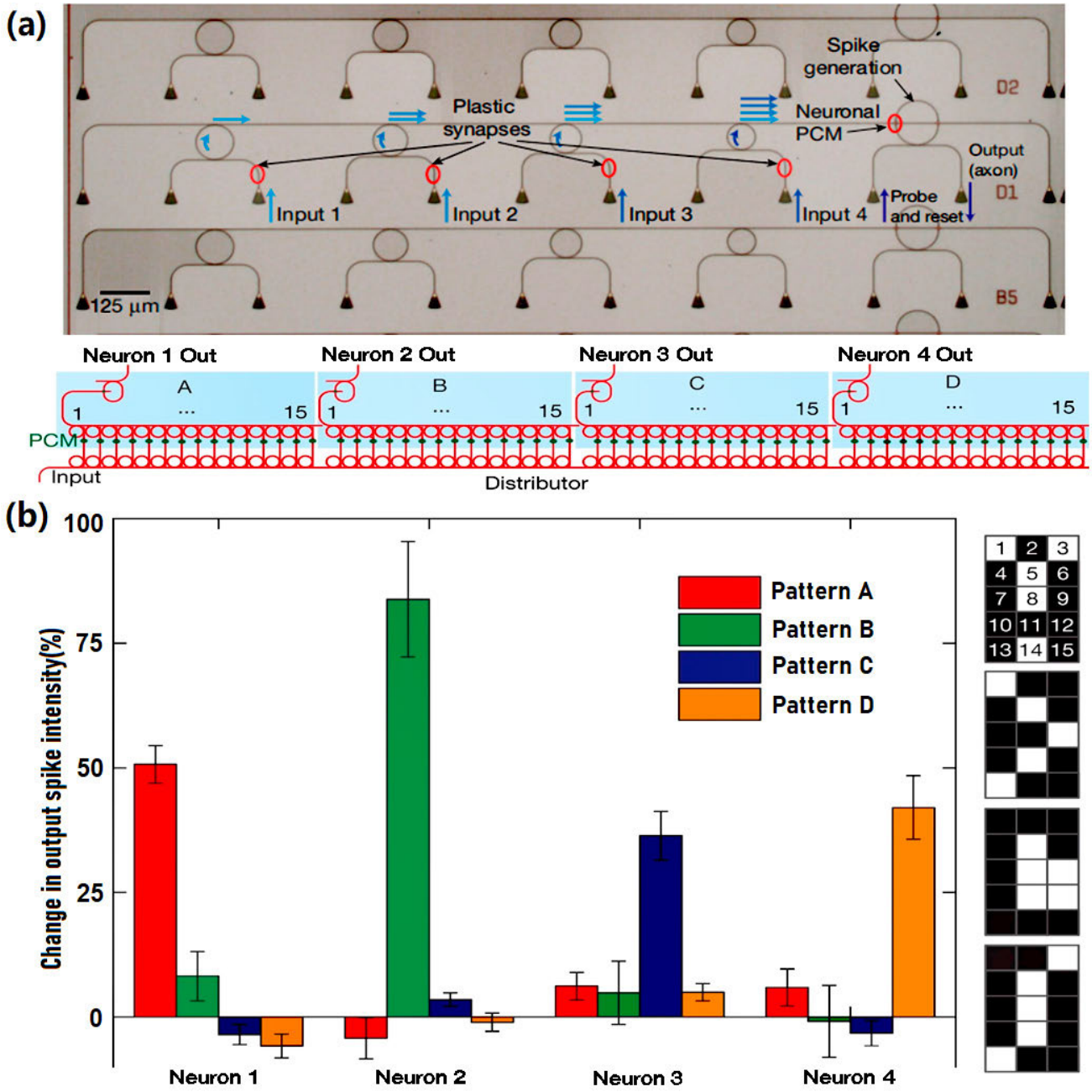

FIGURE 19. (a) Optical micrograph of three fabricated neurons (B5, D1 and D2), showing four input ports. The four small ring resonators on the left are used to couple light of different wavelengths from the inputs to a single waveguide, which then leads to the PCM cell at the crossing point with the large ring. The triangular structures on the bottom are grating couplers used to couple light onto and off the chip. (b) The device consists of four photonic neurons, each with 15 synapses. Each synapses corresponds to a pixel in a 3 × 5 image (see c) and is encoded in the wavelengths corresponding to the ring multiplexers (see numbering in c). The full device comprises an integrated photonic circuit built up from 140 optical components. (c) The change in output spike intensity is shown for the four trained patterns illustrated on the right hand side. The neural network successfully recognizes the four patterns as each neuron only responds (spikes) to one of the patterns. Reprinted with permission from [116].

whose optical properties can be either switched between full crystalline and amorphous states, or continuously adjusted by changing the degree of phase-transformation, considered the most appropriate materials to use for tuneable metasurfaces. As a result, some novel metasurfaces have recently appeared that involve integrating PCMs with conventional metasurface architectures. These can be categorized as phase-change plasmonic metasurfaces and phase-change all-dielectric metasurfaces.

A. PHASE-CHANGE PLASMONIC METASURFACE

Traditional plasmonic metasurfaces are made out of metallic meta-atoms whose optical responses are driven by plasmon resonances supported by metallic particles [125]. Placing a

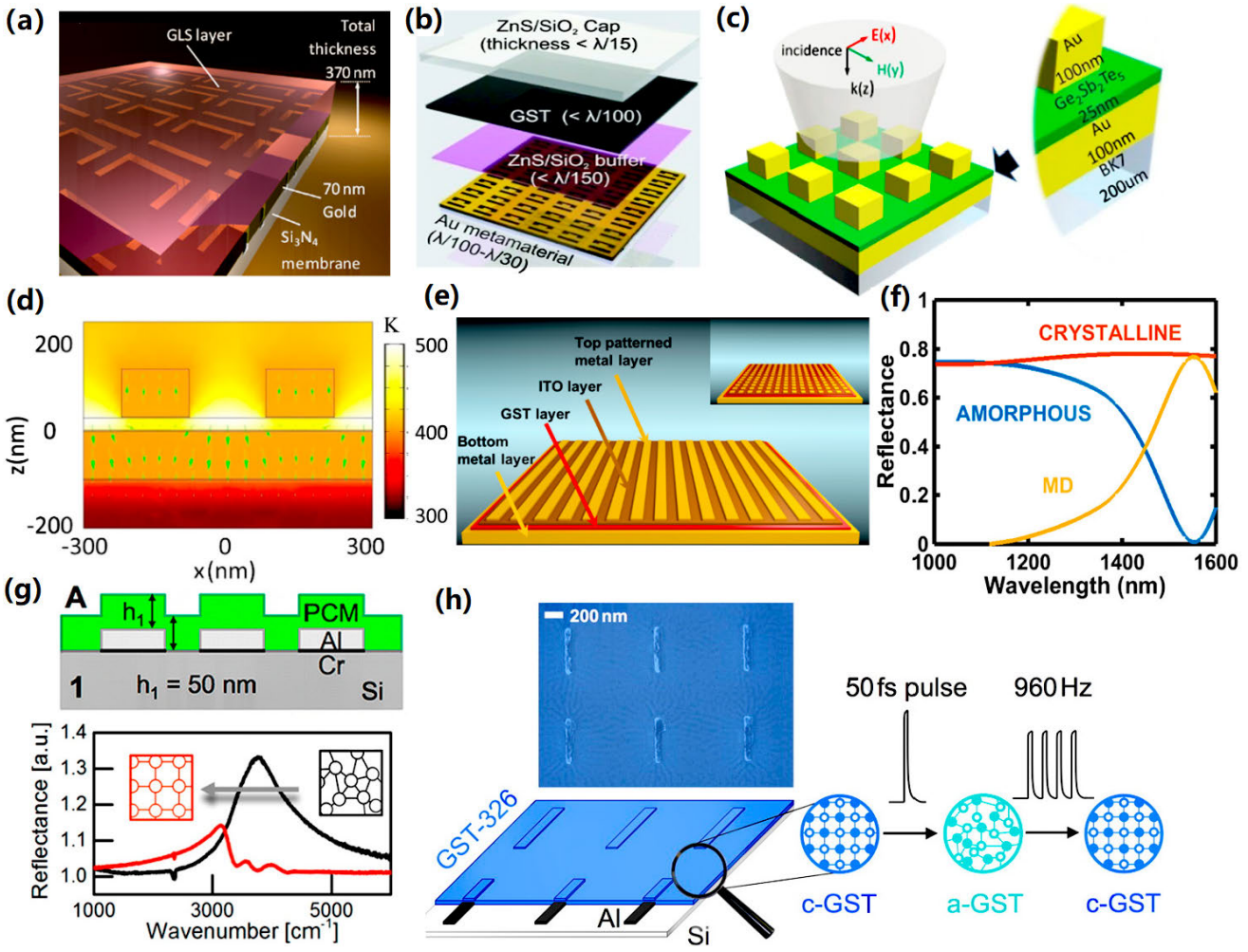

FIGURE 20. (a) Artistic impression of the hybrid device structure comprising a planar gold plasmonic metamaterial on a silicon nitride membrane, covered with GLS Chalcogenide glass. (b)Multilayer structure of near- to mid-IR chalcogenide hybrid metamaterial switches. The phase-change nanolayer of GST and protective buffer and capping layers are sputtered onto planar photonic metamaterials manufactured by focused ion beam milling. (c) Schematic of the metamaterial absorber and the incident light polarization configuration. The thickness of Au squares, GST spacer and Au mirror are 100 nm, 25 nm and 100 nm, respectively. (d) The cross section view of the unit cell of the proposed broadband metamaterial perfect absorber where the color indicates the temperature distribution and the arrows indicate the heat flux aat 0.37 ns. (e) Schematic of a thin-film phase-change metamaterial abosrober/modulator (inset shows the top metallayer patterned into squares for a polarization insenstitivfe design). (f) Simulated reflectance spectrum fro the design in (e) with Au to and bottom metal layers and with the phase-change layer in both the crystalline and amorphous states. Such design was also optimized for maximum modulation depth (MD) at 1550 nm. (g) Resonance tuning of plasmonic antennas in the mid-infrared range utilizing GST-326. (h) A reconfigurable development from (g), in which ooptical pulses are utilized to induce the phase transition in GST. (a) is reprinted with permission from [129]; (b) is reprinted with permission from [130]; (c) and (d) are reprinted with permission from [131]; (e) and (f) are reprinted with permission from [132]; (g) is reprinted with permission from [133]; (h) is reprinted with permission from [134].

metallic particle in an electric field can excite the conduction electrons from their equilibrium positions with respect to the core ions, leading to polarization of the particle as well as a depolarizing field. This collective motion in the metallic particle, when subjected to a time-varying external field, can be treated as a Lorenzian oscillator, whose characteristic peak in the displacement amplitude is around the resonant frequency associated with a phase shift of π over the spectral width of the resonance [126]–[128]. Hence, the electromagnetic field of light waves scattered by metasurfaces can be precisely controlled according to the designing the dimensional parameters of specific units within the surface.

A typical approach to fabricating reconfigurable phase-change plasmonic metasurfaces is to place an initial metasurface on PCMs whose dielectric constant can be adjusted, thus tailoring the plasmonic resonance for optical switching [63]. The first hybrid plasmonic metasurface/PCM can be dated back to the deposition of a gallium lanthanum sulfide (GLS) layer above a periodic array of asymmetrically split gold (Au) resonators [129] (see Figure 20(a)). Applying voltages between the patterned Au layer and an electrode in contact with the GLS layer causes a phase transition inside the GLS layer, resulting in the spectral resonance of the phase-change metasurface undergoing a dramatic blueshift

of 150 nm. The GLS layer in this design was later replaced by a GST thin film sandwiched between two ZnS/SiO_2 thin films that serves as a capping and buffer layers. This produces a resonance shift of over 200 nm in the near-infrared range [130], as shown in Figure 20(b). Inspired by this work, a metasurface absorber that places a GST spacer between Au squares and an Au reflector (see Figure 20(c)), was investigated using numerical simulations [131]. This revealed that the temperature of deposited amorphous GST can be raised from room temperature to 433 K in just 0.37 ns, with a low light intensity of 95 nW μm^{-2}, as shown in Figure 20(d). This ultra-fast phase transition at the cost of ultra-small amounts of energy, was reportedly induced by high broadband light absorptance through strong plasmonic resonances in the absorber [42]. A similar electromagnetic absorber incorporating GST media, that comprises a top Au layer patterned into strips, a GST layer coated with an ITO layer, and a metallic bottom layer, has also been devised [132] (see Figure 20(e)). The incident light yields a plasmonic resonance in the top patterned metal layer as well as in an oscillating in-plane electric dipole. The dipole is coupled to the bottom metal layer, and its coupling strength heavily depends on the phase-state of the GST layer. This phase-change absorber was reported to have a modulation depth of ∼77% and an extinction ratio of ∼20 dB for the near-infrared range (NIR) of the spectrum, notably at 1550 nm, when Aluminum (Al) was used for the top and bottom layers [132] (see Figure 20(f)). In addition to conventional GST, other kinds of PCMs, such as $Ge_3Sb_2Te_6$ (GST326), have also been employed for metasurface applications. The latter was chosen fordue to its low loss in the mid-infrared range and its ability to produce stronger optical contrasts. A 50 nm thick GST326 layer was used to shift the plasmonic resonances of Al antennas by a maximum fractional bandwidth of 19.3%, which was larger than the full-width at half-band-width (FWHM) of the resonance itself [133] (see Figure 20(g)). This design was further developed to incorporate the reversible cycling using a femtosecond (fs) pulse laser as well as exclusion of lossy protective layers [134] (see Figure 20(h)).

It should be pointed out that the tunability of these phase-change metasurfaces relies on the phase transition between their full crystalline and amorphous states. The multi-level optical properties of PCMs that can stem from their partial crystallization play an important role in the dynamic tunability of phase-change metasurfaces. In a similar way to a photonic synapse, the extent of the phase-transformation of PCMs can be continuously changed by adjusting the number of laser pulses illuminating them. This allows for continuous tuning of their reflectivity, transmissivity, and permittivity. This possibility has given rise to the design of a phase-change metasurface consisting of a 20 nm-thick GST film sandwiched by an Au rod array and quartz substrate [135] (see Figure 21(a)). The gradual transition of the GST from its fully amorphous to crystalline state redshifts the resonance mode of the metasurface from 1890 to 2400 nm (see Figure 21(b)). It also results in a large modulation of the transmitted light intensity. Another trilayered phase-change plasmonic resonator with an Au/GST/Au structure, is shown in Figure 21(c). The objective here, was to dynamically shape the wavefront [136]. It was found that both reflected and transmitted light can be precisely manipulated by altering the extent of the crystallization of the GST layer, raising the possibility of free space optical inter/intra chip interconnections. An analogous metasurface structure to the one proposed in [136] was recently implemented for the purposes of beam-steering [137] (see Figure 21(d)). It was observed that continuously varying the strip width from 100 nm to 650 nm enables a phase span of ∼300° in reflected light for the amorphous GST layer due to the excitation of the fundamental gap-surface plasmon (GSP) resonance. The subsequent crystallization of the GST layer induces the redshift of the GSP resonant wavelength owing to the increase of the GST refractive index, giving rise to a nearly constant spatial phase response at $\lambda = 1550$ nm. This offered an oblique reflection angle ($\theta_r = 33.6°$) of the incidence for the amorphous GST (Figure 21(e)), while maintaining a specular reflection for the crystalline GST (Figure 21(f)).

B. PHASE-CHANGE DIELECTRIC METASURFACE

In contrast to plasmonic metasurfaces, dielectric metasurfaces have a unit structure made of dielectric resonators with a high refractive index (e.g, Si, Ge, Te). These can support electric and magnetic dipole responses based on Mie resonances [138]. The illumination of a light wave whose frequency is below or near the bandgap frequency of the dielectric material on a dielectric particle excites both the magnetic dipole and electric dipole resonances. The magnetic and electric fields at optical frequencies at the center of a particle can be significantly enhanced by the magnetic and electric Mie resonance. This is partially determined by the intrinsic properties of the dielectric particles. Dielectric metasurfaces incorporating PCMs are much less lossy than their plasmonic counterparts, so, they have started to attradt a lot of attention. One scenario involves constructing a metasurface that has a patterned GST unit structure in place of a conventional metal one because the low optical loss of GST in the NIR range is associated with non-volatility [135], high stability and a quick response. This has resulted in the development of GST nano-grating metasurfaces, as shown in Figures 22(a) and (b). This device consists of high-quality nanograting arrays of GST media that are fabricated by a focused ion beam (FIB), which have demonstrated non-volatile transmission and reflection resonances. The measured TE-mode spectra for these kinds of GST-based metasurfaces in their amorphous and crystalline states exhibited vast differences in their transmission and reflection at near-resonance wavelengths because of the dramatic change in the complex refraction index of the GST media (see Figure 22(c)). The spectral dispersion of the TE-mode transmission and reflection shows that the grating period (850 nm) will produce a maximum/minimum reflectivity for amorphous/crystalline GST at 1470 nm, respectively. A phase-change metasurface

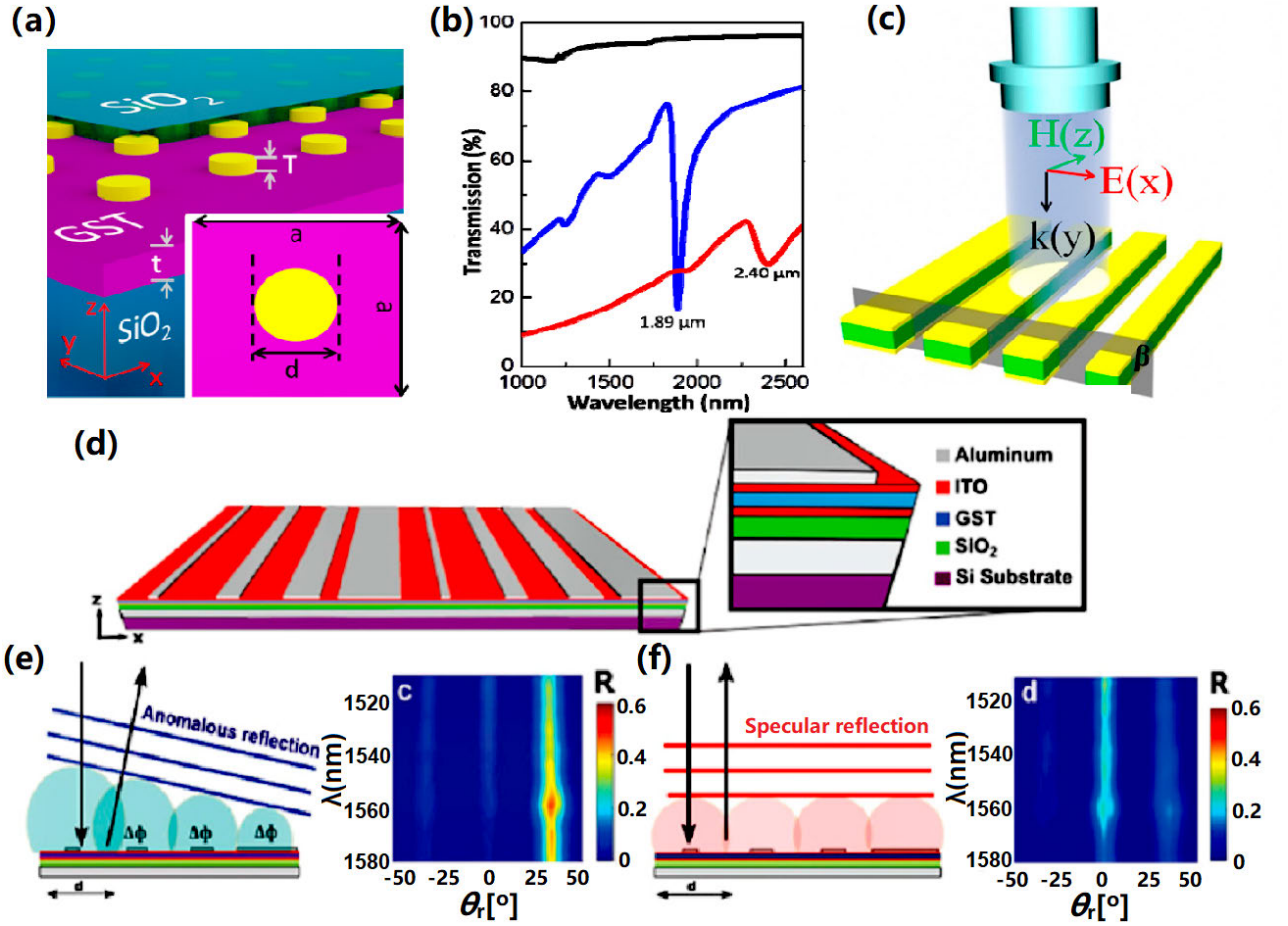

FIGURE 21. (a) Schematic diagram of the GST-Au hybrid plasmonic crystal (T = 40 nm, t = 20 nm, d = 280 nm, a = 1.2 μm). A GST phase-change thin film underneath an array of Au nanodisks is used for controlling the resonant frequencies. (b) Simulated transmission spectra of plasmonic crystals with the GST layer in amorphous and crystalline phases, and a plasmonic crystal without underneath GST. The three spectra are denoted in blue, red and black colors, respectively. (c) Schematic of an array of four MDM strip resonators consisting of a 250 nm thick GST dielectric layer between two 40 nm thick Au films suspended in a vacuum. (d) Reconfigurable plasmonic beam steering nanostructure by combining continuous thin GST layer into the phase-gradient metasurface. The fundamental mechanism of beam-steering and measured angular reflectance in the investigated spectra for both (e) amorphous and (f) crystalline states. (a)-(b) are reprinted with permission from [135]; (c) is reprinted with permission from [136]; (d)-(f) are reprinted with permission from [137].

made up of GST nanorods that allows switchable beam-steering when the GST nanorods are selectively modulated in the telecom range of λ =1.55 μm, has also been recently devised (see Figure 22(d)). The phase states of the GST meta-atoms can be locally modulated by external excitation to change the reflection angle [63].

The tuneable optical response of the GST media can be also utilized to achieve various binary and grayscale photonic devices based on a reconfigurable metasurface having a 70 nm GST layer sandwiched between two ZnS/SiO_2 layers on a glass substrate (Figure 22(e)), exemplified by multifocus Fresnel zone plates [140]. A Fresnel zone was engineered to assign each equivalent intensity to a focal point, and the resulting image from the designed Fresnel-zone-plate contains a set of consecutively impenetrable and transparent rings expanded to focus light by diffraction. Phase transition repeatedly induced between two distinct phases of GST media also stimulated the presence of a dynamic and reconfigurable zone-plate device. Two superimposed Fresnel zone patterns with different foci were first fabricated on a plane, one of which is subsequently amorphized and then re-written back to its crystalline phase. Figure 22(f) shows the write-erase-write configuration cycle with a double Fresnel-zone-plate pattern. A GST326 based metasurface was also devised to realize a non-volatile, all-optical, and reversible switching of surface phononpolaritons (SPhPs) by tuning the phase of an ultrathin GST326 layer [141], as illustrated in Figure 22(g). Phase transition that mainly takes place inside a micrometer-sized domain in the thin GST326 film is induced by a focused ns laser pulse, and a V-shaped resonator composed of two crystalline GST326 arm was created in a 30 nm thick as-deposited amorphous GST326 film. This design can radically confine the SPhPs on a quartz substrate, and generate the subwavelength SPhPs resonators due to the local change of GST326 phase (Figure 22(h)). The successful writing and erasing of subwavelength SPhP resonators

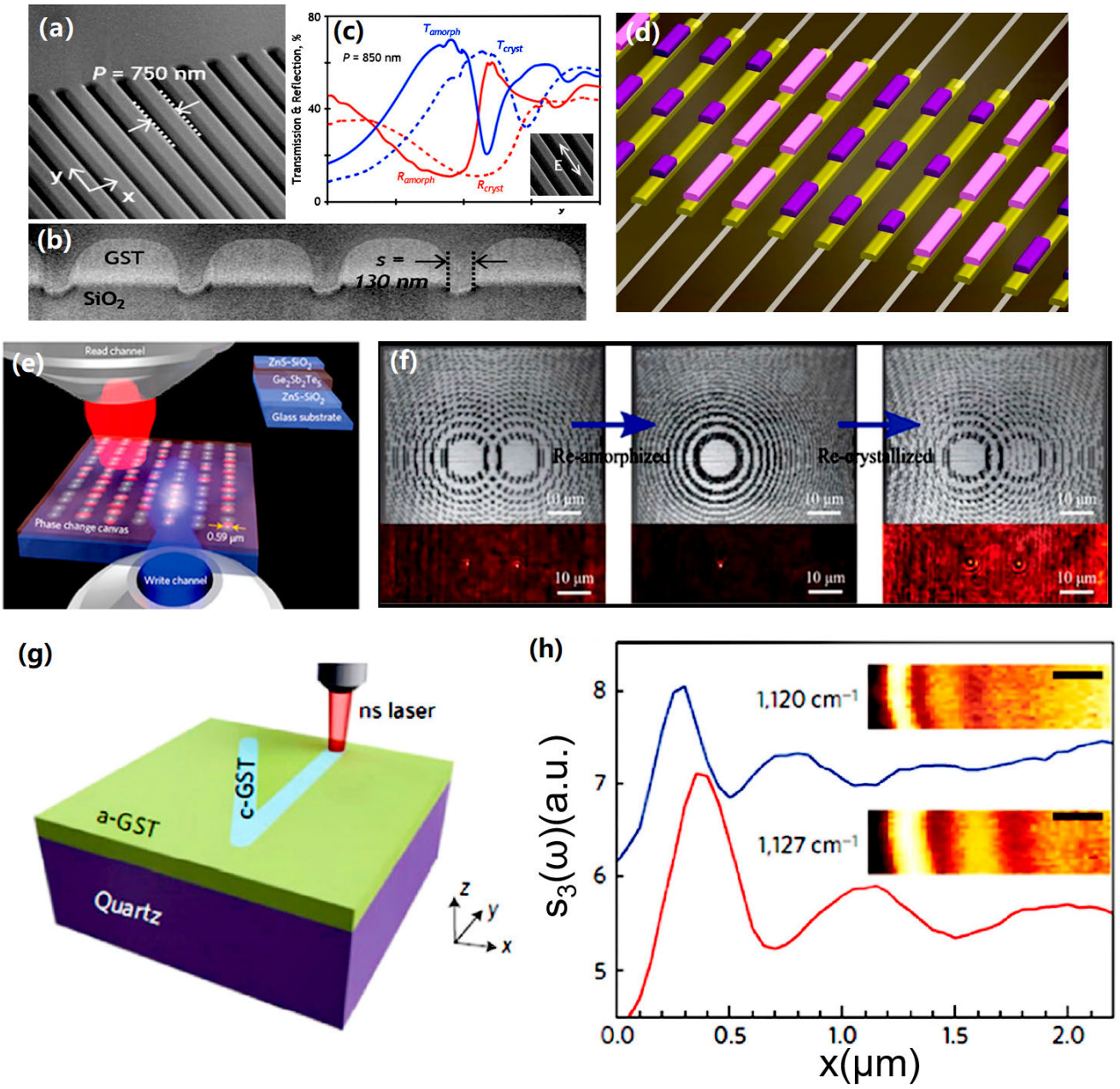

FIGURE 22. (a) Tilted incidence and (b) cross-sectional scanning electron microscopy image of the nanograting in a GST film on an SiO_2 layer. (c) Microspectrophotometrically measured TE-mode reflectivity and transmission spectra for the as-deposited amorphous and laser-annealed crystalline phases of a 300 nm thick GST nano-grating metamaterial with a period P = 850 nm. (d) Schematics for realization of the selective modification of phase-change metasurface. Phase states of GST cells can be changed by applying electric current pulses through the conductive wire. (e) Scheme of reconfigurable phase-change metasurfaces. Femto second pulses are focused and positioned across the surface to change the refractive index of GST active layer by converting continuously from the amorphous to crystalline state. The written pattern can be erased by the same laser with the different parameters. The written devices are observed via the "read" channel. (f) Optically reconfigurable Fresnel zone-plate devices. The top row shows the optical images of the patterns written, erased, and rewritten on the GST film, and the bottom row shows the corresponding transmission focal spots $\lambda = 730$ nm. (g) Schematic of switching a V-shaped crystalline GST domain in a 30 nm thick amorphous GST film by scanning a pulsed laser with proper parameters. (h) Line profiles of optical amplitudes at two different frequencies indicate the existence of ultraconfined surface phonon-polaritons (SPhPs). (a)-(c) are reprinted with [139]; (d) is reprinted with permission from [63]; (e) and (f) are reprinted with permission from [140]; (g) and (h) are reprinted with permission from [141].

array on the as-deposited amorphous GST326 film leads to a rewritable platform for subwavelength optical devices with high speed.

Some recent work on metasurfaces has explored ways of improving the phase-tuning of the PCMs, their diffraction performance and their degree of loss. One such study has developed generic principles for the design of a 2π range all-dielectric architecture [142]. The proposed architecture was tested using a 5.2 μm wavelength varifocal metalens constructed out of $Ge_2Sb_2Se_4Te_1$ (GSST), which offered a

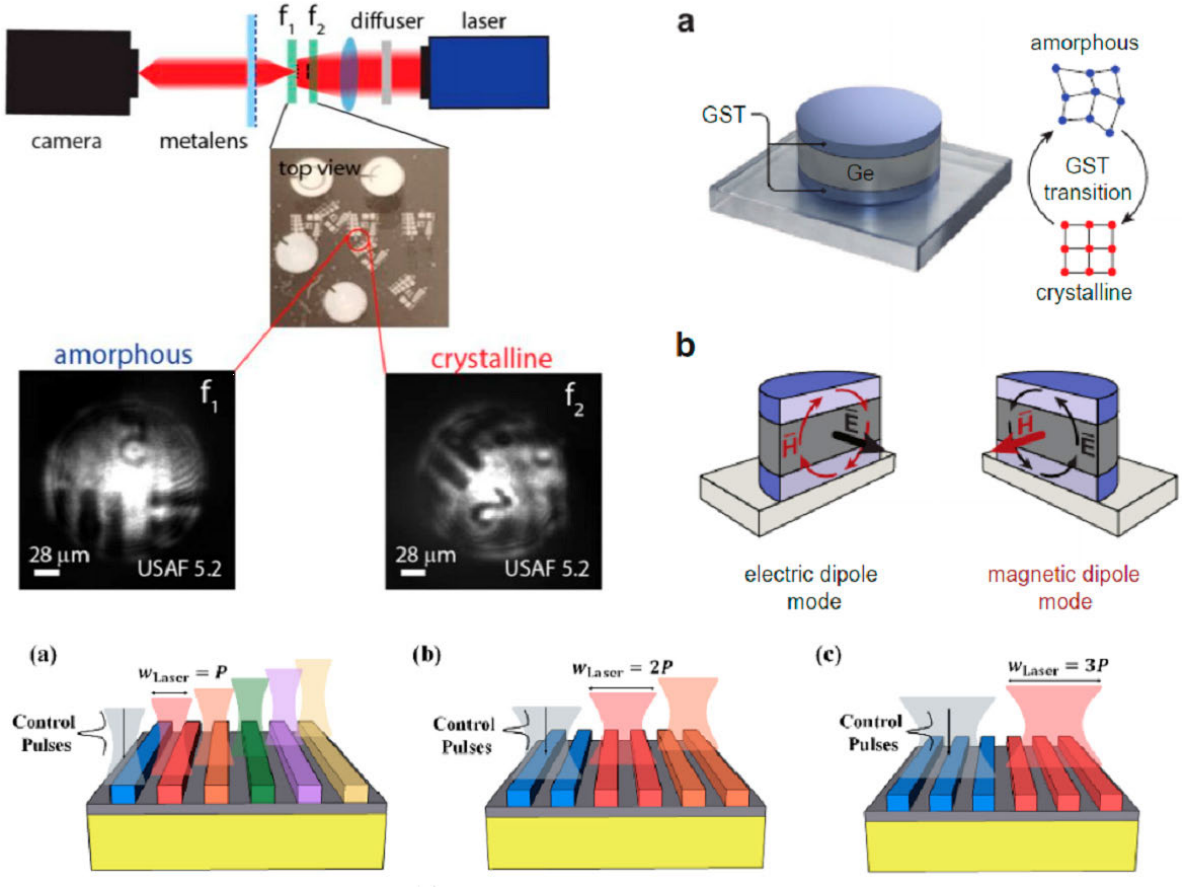

FIGURE 23. (a) Schematic of the setup for imaging multi-depth targets. Top view photograph of the target consisting of two patterned samples overlapped at an angle of 45°. Camera images of the dual-depth target acquired by a stationary metalens in a- and c-states. (b) A multi-layer dielectric meta-unit design incorporating the switchable phase-change material GST in a sandwich-like structure enables mid-IR optical phase modulation (top) and the disk-shaped meta-units sustain magnetic (MD) and electric dipole (ED) resonances, where the spectral positions can be dynamically reconfigured by changing the crystallinity of the GST layers (bottom). (c) Illustrataion of laser-induced crystallization of an array of GSST nanobars when one, two, and three neighbour nanobars should be crystallized to the same level depending on the waist of used laser pulse. (a) is reprinted with permission from [139]. (b) is reprinted with permission from [140]. (c) is reprinted with permission from [141].

refractive index contrast of $\Delta n > 1$ with low-loss in both crystalline and amorphous phases. GSST is able to deliver better broadband transparency in the infrared than conventional GST. The design depended upon the optimization of the meta-atom design, which was achieved through calculation of the different diffraction efficiencies of a pool of Huygens meta-atoms. The metalens presented an efficiency of over 20% and switching contrast ration of 29.5 dB, which is very high. Figure. 23(a) shows the basic set-up of this architecture and some sample results. A similar interest in all-dielectric metasurfaces that are tunable in the infrared can be found in [143]. In this case, multilayer Ge disks are topped and bottomed with GST (see Figure 23(b)). Ge was selected for the disk core because of it having a virtually zero absorption loss in the mid-IR spectrum. By careful design of the shape of the disk and its height, electric dipole (ED) and magnetic dipole (MD) resonances can be maintained in close proximity (see Figure 23(b)). An incident electric field can induce the ED and polarize the dielectric disk at a chosen resonant frequency. An oscillating displacement current can serve to induce the magnetic dipole. The magnetic mode is more susceptible than the electric mode to changes in the refractive index of the GST upon crystallization. When the GST is crystallized it satisfies the Kerker condition [144], such that there is a spatial and spectral overlap of resonances that delivers constructive interference in the direction of the transmission, giving almost perfect transmittance at specifically chosen wavelength. Different optical phase shifts of π for each particular resonance can ultimately provide almost a full 2π phase modulation. Different states of crystallization can encode different values. Optical switching of the individual disks in the metasurface makes it possible to write specific optical phase profiles on the surface. This makes the metasurface capable of producing HR phase-encoded images and therefore of potential utility for tunable lenses, dynamic holograms and spatial light modulators. When tested, it proved to be possible to tune the metasurface's light phase across 81% of the 2π range.

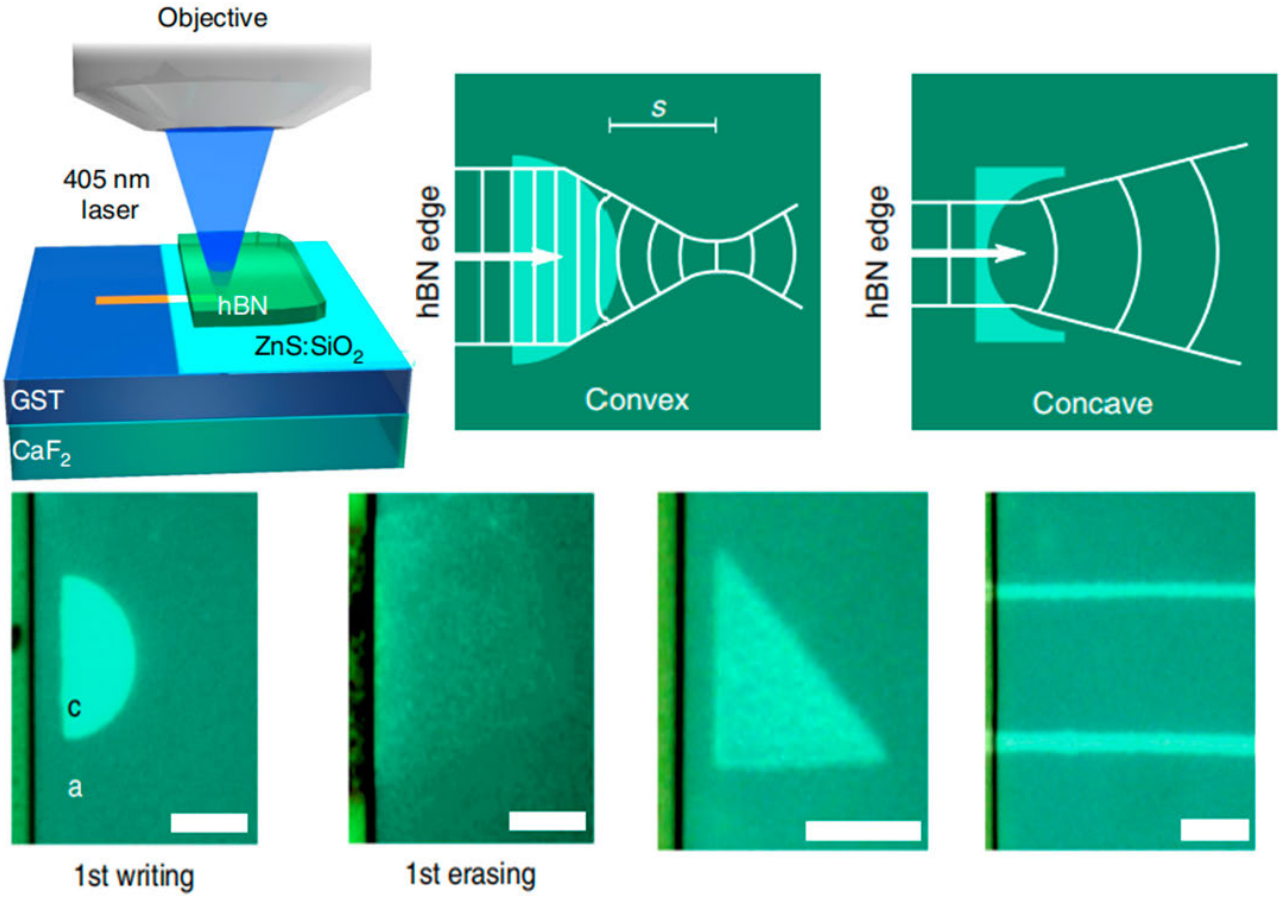

FIGURE 24. (a) Writing setup and device cross-section. A 405 nm focused laser beam is used to write and reconfigure devices on GST underneath hBN (transpartent at 405 nm). (b) Optical images of the written and erased lens. (c) Diagram of wavefronts for 2D plano-convex and plano-concave lenses, respectively. (d) Optical image of the written prism with an isosceles right-angled triangle with edges of 7.5 μm (left) and the written waveguides having top 0.7 μm wide and bottom 1.1 μm wide (right). Reprinted with permission from [146].

Forouzmand and Mosallaei [145] laid some important groundwork for the evolved use of GSST for phase-change metasurfaces by developing GSST nanobars. These nanobars use the varying degree of GSST crystallization as a means of defining the strength and spectral character of magnetic and electrical resonances. One of the key advantages of their approach is the capacity to work at an off-resonance level in the centre of the geometrical resonances, which can prevent high field confinement and dissipative loss. This enables the possibility of high reflectivity of levels between 0.6 and 0.8 and a wide phase angle of about 270°. Their technique renders a reflected beam's wavefront controllable through the selective crystallization of the GSST (Figure 23(c)). Numerical simulation has suggested that this can deliver a reflection efficiency of over 45%. Some promising work that has taken place lately that also exploits the properties of PCM-based dielectric surfaces relates to the creation of miniaturized optoelectronic devices and biosensors using phonon resonators [146]. This research centers upon the using polaritons, which are generated by coupled light-matter interactions. These interactions occur at a nanoscale and significantly extend the potential scope of optics. The challenge confronting work in this area is being able to effectively control polariton propagation and harness its characteristics in actual devices. The propagation of phonon polaritons (PhPs) is heavily influenced by the refractive indices of the surrounding superstrate an substrate. Chaudary *et al.* [146] have therefore experimented with the possibility of polariton-based optics in the mid-infrared by drawing upon the interaction of phonon polaritons in boron nitride (hBN) with a surrounding GST-based dielectric environment. This specific combination has several useful advantages. hBN contains low-loss polaritons that are notable for their long propagation lengths. GST provides highly-contrasting refractive indexes according to its phase. Chaudary *et al.*'s work has shown that a hBN-GST heterostructure can allow for the effective control of PhP propagation by writing, erasing and re-writing arbitrary patterns. On the basis of their approach they were able to construct reconfigurable 2D refractive polariton lenses using a 55 nm layer of GST under a 195 nm layer of hBN. The GST was itself deposited on a CaF_2 substrate and protected against oxidation by a q5 nm layer of $ZnS:SiO_2$ (Figure 24(a)). A pulse laser diode was then used to write and erase patterns

by crystalising and re-amorphising the GST. The propagation angle of the polaritons can then be controlled by the write and erase process (Figure 24(b)). This allowed for the creation of semi-circular plano-convex and plano-concave lenses (see Figure 24(c)). Chaudary *et al.* also established the viabiltiy of using the same approach to create prisms and waveguides (Figure 24(d)) and, through the use of arrays, reconfigurable one-dimensional metalenses that can focus the propagation of polaritons in two-dimensions.

VI. PHASE-CHANGE COLOR DISPLAY

The tuneability of most of the aforementioned PCM-based photonic devices is dependent upon external excitations such as laser pulses or thermal heating. To fulfill the practica requirements of tuning, it is essential to locally modulate the amplitude pixel by pixel, which is realized by selective electronic switching techniques. This has been exploited by an optoelectronic reflective display that was developed to achieve high resolution display functionality, rapid switching at a low power cost [147]. The framework in question has a GST thin film sandwiched between two conductive ITO layers on a platinum (Pt) coated Si wafer, as illustrated in Figure 25(a). Switching the phase state of the GST film between its amorphous and crystalline states can then display various colors. The actual colors depends on the thickness of the GST thickness (Figure 25(b)). An array of different colored pixels has been fabricated using lithographic techniques to make a display. A nanometer-sized probe was implemented to electrically switch the color of each pixel, as shown in Figure 25(c). This innovative technique can scale down the pixel size to 300 nm, thus providing an ultrahigh-resolution display. The large optical contrast this makes possible is testified by the electronically constructed image obtained by using a nanoscale conductive tip, that can be seen in Figure 25(d). A growth dominated PCM, i.e., $Ag_3In_4Sb_{76}Te_{17}$ (AIST), was later adopted for nanopixel displays. These materials, offer superior depth modulation comparison to the GST-based nanodisplays [148] (Figure 25(e)). Using multilayer optical cavities enables an off-line color modulation that has a resolution as fine as 300 nm in scanning mode, and less than 50 nm in pixel-by-pixel mode. It can be seen in Figure 25(f) that partially crystallizing AIST by electronic means leads to continuous grayscale images beyond binary colors. This raises the possibility of grayscale colored pictures. Most recently a switchable phase-change metasurface resonant absorber, created by fusing a phase-change optical metasurface and an optoelectronic display, was fabricated that shows exotic color-generation capabilities [149]. The basic structure (Figure 25(g)) consists of an Al bottom plane, a GeTe layer, an ITO layer, and a top Al layer patterned in circles. The negative value of the real part of the permittivity of the GeTe in its crystalline phase produces an optically metallic-like behavior. This can be employed to support and confine a resonant mode primarily in the ITO layer for a specific spectral band. This makes the designed metasurface absorb the energy that corresponds to wavelengths that fulfill the resonant condition. As a result, a device structure containing GST in its crystalline state can absorb in the red, green, and blue (RGB) wavebands. This enables the genreation of cyan, magenta, and yellow (CMY) pixels, respectively. By the same token, if the GeTe is switched to its amorphous state, the resonant absorption is switched off and a white-like reflectance is obtained. Figure 25(h) shows a binary (black and white) image of part of an old city wall, rendered by using the designed display device and magenta pixels, with the GeTe layer being in either a crystalline or amorphous state. There are numerous potential applications for such displays, including mobile devices, in-window displays, near-eye displays, and artificial retinas.

Recent work undertaken by Bodle Technologies, a spin-off from the University of Oxford, has been seeking to expand upon the research reported above by exploring the use of PCM-based color display technology to overcome a noted difficulty with how state-of-the-art solid-state reflective displays (SRDs) go about displaying color and video content. The focus in this technology builds upon the notion described above of using electrical impulses to switch PCM nanocavities between their amorphous and crystalline state [150]. As noted, this alone is enough to induce a change in color at very high speeds and with very low power consumption, with the technology being able to produce red, green and blue pixels, so it can cover the whole of the color spectrum. However, PCMs were initially considered unsuitable for color displays because of their high optical absorption and the strong limitations there seemed to be upon the extent to which they could modulate visible light [151]. When it was found that using ultra-thin PCM layers of less than 50 nm as lossy absorbers in interference stacks with transparent spacers between the PCM and a metallic substrate could result in amplification of saturation and reflected color [147], the use of PCMs for color displays received a new impetus. Despite this overall shift, one of the principal issues with using PCMs in this way for SRDs is being able to realize the switching effect across large enough areas of pixels for it to meet the requirements of a color display. There is also a need to provide controllable color, not just in terms of RGB brightness and saturation, but also in terms of being able to move between vivid, high contrast states and pale, highly reflective states (RGBWK) [151], [152]. In order to meet these requirements and gain better control over the thermal response of the PCM, the Bodle Technologies team came up with an SRD microheater pixel design that disposed of the need for the switching pulse electrical current to be conducted by the active material (Figure 26(a)). This enabled the optical layers to be completely isolated from the driving electronics, so that attention could be fully devoted to their optical and thermal properties. In subsequent work [153], they characterized the SRD pixel design as consisting of three planes: a backplane; a midplane; and a frontplane (Figure 26(b)). The backplane is constructed of a glass substrate with a row and a column electrode placed on top, together with an LTPS diode that was specifically

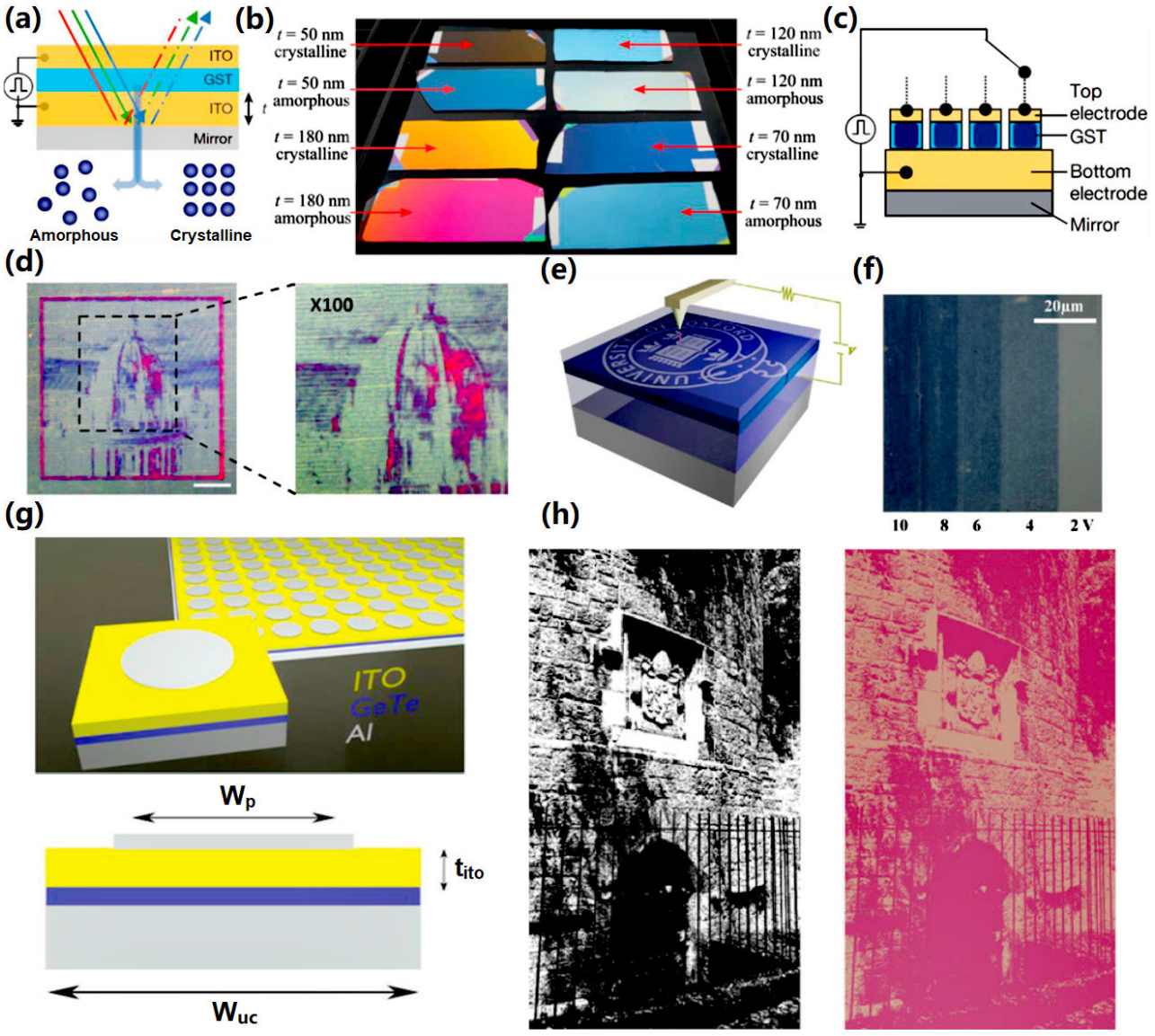

FIGURE 25. (a) Schematic of the ITO/GST/ITO thin-films layers for dynamic color change when the few-nanometers-thick GST layer undergoes phase transition. (b) Four different thin films with different thickness of the intermediate GST layer show different reflective colors when GST is in amorphous and crystalline states, respectively. (c) Schematic illustration of the GST-integrated optoelectronic framework emerging as promising blocks for high-resolution color pixels and display devices. (d) Electrically constructed image on a lithographically defined 300 × 300 nm^2 pixel array on a standard thin-film stack with a 50-nm-thick GST layer. (e) Sketch of the experimental setup where conductive atomic force microscopy (AFM) is used to locally switch AIST by applying voltage between the two ITO layers. (f) Different colors in reflection mode corresponding to different levels of crystallization of AIST layer by changing the scanning voltage from 0 to 10 V. (g) 3D schematic of the phase-change absorber structure and the materials (top) and cross sectional view of the structure with labeling of the geometrical parameters varied in the optimization of the devices. (h) A binary (black and white) image of part of Exeter's city wall (left), rendered to a binary image using magenta pixels (right) with the GeTe layer in both crystalline (for the black regions) and amorphous (for the white) phases. (a)-(d) are reprinted with permission from [147]; (e)-(f) are reprinted with permission from [1459]; (g)-(h) are reprinted with permission from [149].

designed to be optimal for pulse delivery to the SRD. The midplane is effectively the thermal layer, consisting of an optimized microheater attached to the electrodes and driven by the LTPS diode for uniform pixel heating, with a planarization/insulation layer underneath and a comprehensive isolation layer above. The optical frontplane is a 4-layer interference stack made up of a metallic mirror, the PCM (GST was used in their test fabrication), a transparent dielectric spacer and a capping layer. This design has proved capable of high contrast controllable switching for active areas of between 25 × 25 μm and 600 × 600 μm [151], [152]. Simulations conducted by the Bodle Technologies team arrived at an optimal stack design that could deliver the range of colors, contrast and reflectivity needed for full-color displays (Figure 26(c)). These indicated the possibility of arriving at displays with a white-state luminance reflectivity exceeding 50% and of anything between 40% and 80% of the standard RGB color gamut (sRGB). This can be compared to reflective

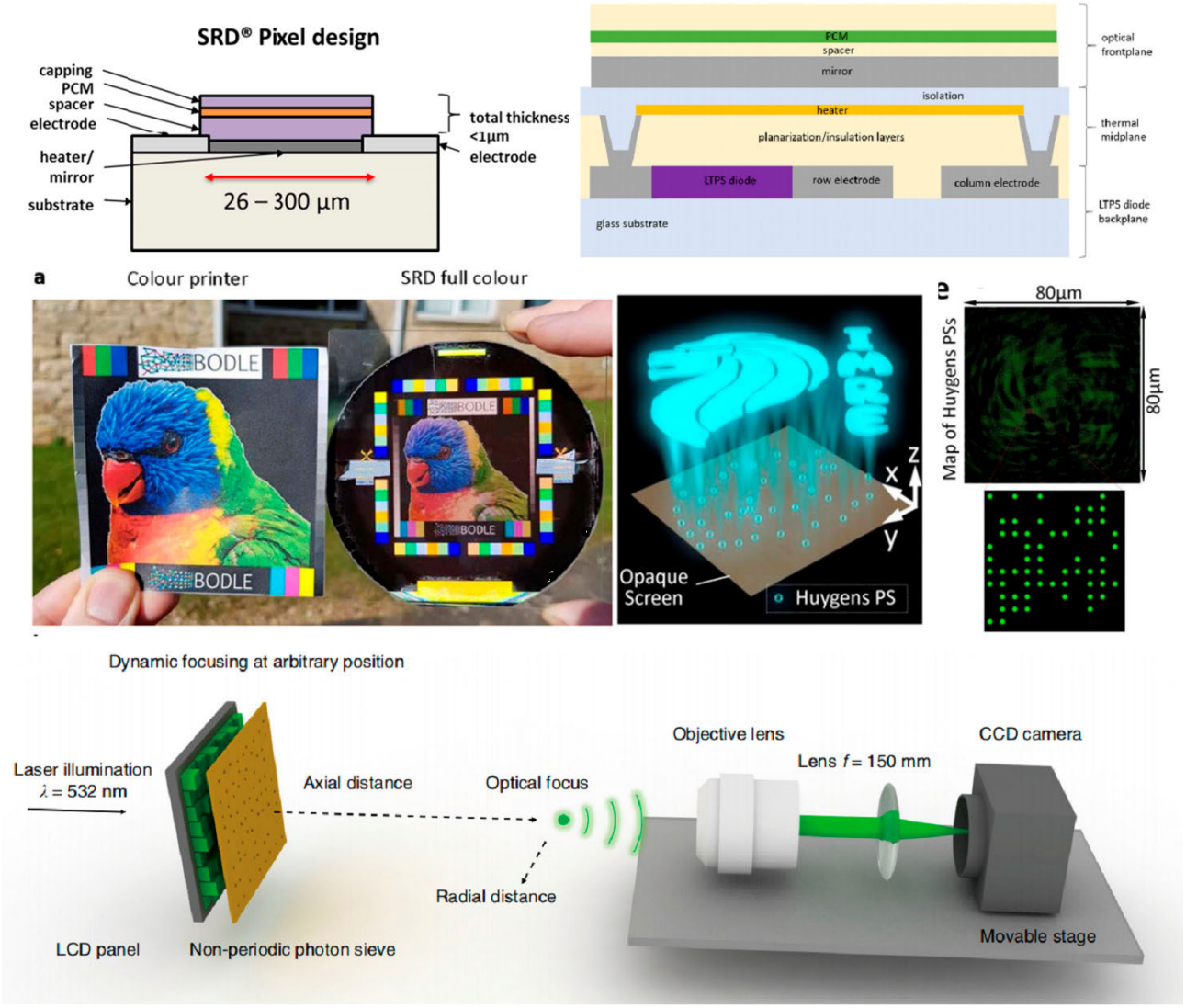

FIGURE 26. (a) Schematic of the preliminary SRD microheater pixel design. (b) Schematic of the updated SRD pixel structure having three layer sets. (c) A static full color SRD demo created via a lithographically defined subpixelated process (right) is placed next to a color printed version of the same picture (left). No enhancement in contrast or brightness was applied to this picture. (d) Sketch of PS-based holograms for displaying an image (left) and a map of PS-based hologram with 20, 931 PSs located in an 80 μm $\times \mu$m square. The PSs are denoted by the green dots. (e) Scheme of dynamic optical focusing over a wide volume. Optical focus is generated at arbitrary positions by displaying optimal patterns at the LCD panel. (a) us reprinted with permission from [151]. (b) is reprinted with permission from [153]. (c) is reprinted with permission from [152]. (d) is reprinted with permission from [154]. (e) is reprinted with permission from [155].

LCD displays which typically provide about 21% reflectivity and 35% of the sRGB [151], [152]. Subsequent physical testing with prototype RGB color films containing a PCM layer that were deposited over large areas achieved a white state luminance of 30% and an sRGB of 47% [152]. The reasons for these figures not yet achieving the maxima implied by the simulations was put down to the need to further refine the film and the associated deposition technique.

A further relevant development here, that relates not only to phase-change color displays but also to the work on plasmonic metasurfaces discussed in Section 5.1, is the use of photon nanosieves for the projection of 3D holographic color displays. Photon nanosieves are effectively photon nanogratings constructed out of plasmonic metasurfaces that are capable of pixel by pixel projection for the generation of high-quality holographic images [154] (Figure 26(d)). However, existing approaches, here, have been criticized for their dynamic modulation capability and slow refresh rates [155]. A promising new design here that may be able to overcome these difficulties confronting the effective use of PCM-based photonics for holographic display has been developed by Park *et al.* [155]. In this design, a non-periodic nanosieve is placed directly in front of commercially available LCD displays, with the number of pinholes in the nanosieve being exactly the same as the number of pixels in the display (Figure 26(e)). The goal here is to provide the possibility

of dynamic holograms rather than static holograms. Previous work in this area focused on tailoring the size and distribution of the pinholes [156], which only allows for static images. In Park *et al.*'s design the positioning of the pinholes is more or less random and the focus is upon tailoring the LCD-acquired light incident on the pinholes instead. The pixels from the LCD are randomly assigned to RGB lasers and the wavefronts from each laser are then separately modulated by the nanosieve to produce three-colour, potentially dynamic holographic images [155].

VII. CONCLUSION AND OUTLOOKS

Non-volatile memory manipulated by light is not a newly-invented concept. It was already present in the advent of phase-change optical discs, such as rewritable DVDs and rewritable Blu-ray technologies that date back several decades. PCM-based non-volatile memory is now considered to be one of the most promising contenders in the external storage market owing to its rewritability and portability. However, far-field diffraction limits severely impair the recorded density of phase-change optical discs, making it harder for them to compete with other popular tertiary storage memories like hard disk drives (HDDs) and Flash memory. Some emerging technologies and approaches, such as near-field recording and multi-disc/level techniques, can enhance the storage capacity of phase-change optical discs, but are usually accompanied by a greater cost and more cumbersome architecture. As a result, the outlook for phase-change optical discs remains pessimistic, meaning that they will slowly drop out of view for research industry. More advanced storage solutions are therefore required to avoid the demise of optical discs in the near future.

In spite of the dim prospects for off-chip storage, on-chip photonic memory using PCMs has recently shown exciting potential in the field of in-memory computing. The problem of the von Neumann bottleneck has recently been exacerbated by the increasingly pronounced difference in operational speed between CPUs and the main memory of devices [157]. As a result, the CPU is remaining idle for even loger while it waits for data to be retrieved from the electronic memory. This issue can be addressed by using an integrated all-photonic memory based on PCMs that can avoid the need to convert between electrical and optical signals during the information exchanging between the processors and the memory. This novel kind of device can not only store and execute data in the same place by using multiple wavelengths, but also accelerate the read-write speed with smarter algorithms [158]. However, despite these advantages, a number of challenges still remain. Although write energy at a picojoules level can be achieved, this operation does not yet achieve the high sensitivity required for reliable multibit operations. This is because multi-level operations usually need a higher signal-to-noise ratio, and thus require higher power devices. Another challenge arises from the relatively large footprint of all-photonic memory. This is due to the fact that telecom wavelengths have been adopted, which require the waveguides that are very space hungry. This will have a negative impact on the integration density of photonic devices. To overcome this drawback, it is essential to explore shorter wavelengths, which might move photonic memories away from standard silicon and silicon nitride waveguides and possibly towards AlN waveguides [159]. Unfortunately, designing photonic memory at shorter wavelengths currently has an adverse effect on PCMs and results in higher extinction coefficients.

Phase-change metasurfaces that rely on the switchable optical properties of PCMs have triggered a lot of encouraging applications including switchable perfect absorbers, thermal emitters, beam-steering, and color displayings. The exploration of new PCMs with low losses and superior optical responses indeed is accelerating developments of phase-change metasurface technologies. This is evidenced by the creation of the GSST PCM, which allows for transparency and low loss in an extremely wide broadband range (1-18.5 μm), with a large optical contrast of 2 [145], [160]. This obviously renders metasurfaces using GSST suitable for new applications in infrared and thermal photonic devices. However, the operation of most reported phase-change metasurfaces depends on the phase transformation from amorphous to crystalline states. Although rewriting PCM thin films with endurance of over one million cycles at an ultrafast speed has already been demonstrated for aelectronic approaches [161], reproducing this functionality with photonic metasurfaces is more challenging because of the need to have protective layers and additional electrodes. This may negatively influence the design and functionality of these kinds of metasurfaces. Additionally, local heating is required for phase transformation. This is likely to harm the plasmonic nanostructures and photothermal effects may even reshape their geometries [162]. In spite of these issues, such super-fast and low-dimensional phase-change metasurfaces will have a very promising market for the forseeable future because of their applicability to a wide range of applications, from conventional global and local amplitude/phase control to more novel and exciting fields such as smart glasses, smart contact lenses and synthetic retinas [163].

REFERENCES

[1] Z. Wang, H. Wu, G. W. Burr, C. S. Hwang, K. L. Wang, Q. Xia, and J. J. Yang, "Resistive switching materials for information processing," *Nature Rev. Mater.*, vol. 5, no. 3, pp. 173–195, Mar. 2020.

[2] W. Eerenstein, N. D. Mathur, and J. F. Scott, "Multiferroic and magnetoelectric materials," *Nature*, vol. 442, pp. 759–765, Aug. 2006.

[3] G. Catalan and J. F. Scott, "Physics and applications of bismuth ferrite," *Adv. Mater.*, vol. 21, no. 24, pp. 2463–2485, Jun. 2009.

[4] M. Gajek, M. Bibes, S. Fusil, K. Bouzehouane, J. Fontcuberta, A. Barthélémy, and A. Fert, "Tunnel junctions with multiferroic barriers," *Nature Mater.*, vol. 6, no. 4, pp. 296–302, Apr. 2007.

[5] R. Sbiaa and S. N. Piramanayagam, "Recent developments in spin transfer torque MRAM," *Phys Status Solidi-R.*, vol. 11, no. 12, 2017, Art. no. 1700163.

[6] K. A. Ahmed, F. Li, S. Y. H. Lua, and C. H. Heng, "Area-efficient multibit-per-cell architecture for spin-orbit-torque magnetic random-access memory with dedicated diodes," *IEEE Magn. Lett.*, vol. 9, 2018, Art. no. 4303105.

[7] J.-G. Zhu, "Magnetoresistive random access memory: The path to competitiveness and scalability," *Proc. IEEE*, vol. 96, no. 11, pp. 1786–1798, Nov. 2008.
[8] B. K. An, S. B. Kim, and Y. H. Song, "Effect of bottom electrode size on Ovonic Threshold Switch (OTS) characteristics," *J. Semicond. Technol. Sci.*, vol. 20, no. 1, pp. 8–11, 2020.
[9] S. Durai, S. Raj, and A. Manivannan, "An extremely fast, energy-efficient RESET process in $Ge_2Sb_2Te_5$ phase change memory device revealed by the choice of electrode materials and interface effects," *Semicond. Sci. Technol.*, vol. 35, no. 1, 2020, Art. no. 015022.
[10] J. Choi, J. Jang, and L. S. Kim, "DC-PCM: Mitigating PCM write disturbance with low performance overhead by using detection cells," *IEEE Trans. Comput.*, vol. 68, no. 12, pp. 1741–1754, Dec. 2019.
[11] H.-S. P. Wong, H.-Y. Lee, S. Yu, Y.-S. Chen, Y. Wu, P.-S. Chen, B. Lee, F. T. Chen, and M.-J. Tsai, "Metal-oxide RRAM," *Proc. IEEE*, vol. 100, no. 6, pp. 1951–1970, Jun. 2012, doi: 10.1109/JPROC.2012.2190369.
[12] A. Wedig, M. Luebben, D.-Y. Cho, M. Moors, K. Skaja, V. Rana, T. Hasegawa, K. K. Adepalli, B. Yildiz, R. Waser, and I. Valov, "Nanoscale cation motion in TaOx, HfOx and TiOx memristive systems," *Nature Nanotechnol.*, vol. 11, no. 1, pp. 67–74, Jan. 2016.
[13] J. Choi, J. S. Han, K. Hong, S. Y. Kim, and H. W. Jang, "Organic–inorganic hybrid halide perovskites for memories, transistors, and artificial synapses," *Adv Maters.*, vol. 136, Oct. 2018, Art. no. 1704002.
[14] H.-S. P. Wong, S. Raoux, S. B. Kim, and J. Liang, "Phase change memory," *Proc. IEEE*, vol. 98, no. 12, pp. 2201–2227, Dec. 2010.
[15] G. W. Burr, M. J. Breitwisch, and M. Franceschini, "Phase change memory technology," *J. Vac. Sci. Technol. B, Microelectron.*, vol. 28, no. 2, pp. 223–262, 2010.
[16] D. Loke, T. H. Lee, W. J. Wang, L. P. Shi, R. Zhao, Y. C. Yeo, T. C. Chong, and S. R. Elliott, "Breaking the speed limits of phase-change memory," *J. Vac. Sci. Technol. B, Microelectron.*, vol. 28, pp. 223–262, Jun. 2010.
[17] F. Rao, K. Y. Ding, Y. X. Zhou, Y. H. Zheng, M. J. Xia, S. L. Lv, Z. T. Song, S. L. Feng, I. Ronneberger, R. Mazzarello, W. Zhang, and E. Ma, "Reducing the stochasticity of crystal nucleation to enable subnanosecond memory writing," *Science*, vol. 358, no. 6369, pp. 1423–1427, 2017.
[18] D. B. Strukov, G. S. Snider, D. R. Stewart, and R. S. Williams, "The missing memristor found," *Nature*, vol. 453, no. 7191, pp. 80–83, May 2008.
[19] M. Shin, K. Min, H. Shim, and Y. Kwon, "Investigation on phase-change synapse devices for more gradual switching," *J. Semicond. Technol. Sci.*, vol. 19, no. 1, pp. 8–17, Feb. 2019.
[20] T. Tuma, M. Le Gallo, A. Sebastian, and E. Eleftheriou, "Detecting correlations using phase-change neurons and synapses," *IEEE Electron Device Lett.*, vol. 37, no. 9, pp. 1238–1241, Sep. 2016.
[21] D. Kuzum, R. G. D. Jeyasingh, B. Lee, and H. S. P. Wong, "Nanoelectronic programmable synapses based on phase change materials for brain-inspired computing," *Nano Lett.*, vol. 12, no. 5, pp. 2179–2186, 2012.
[22] M. Suri, O. Bichler, D. Querlioz, O. Cueto, L. Pemiola, V. Sousa, D. Vuillaume, C. Gamrat, and B. DeSalvo, "Physical aspects of low power synapses based on phase change memory devices," *J. Appl. Phys.*, vol. 112, no. 5, 2012, Art. no. 054904.
[23] G. W. Burr, R. M. Shelby, S. Sidler, C. Di Nolfo, J. Jang, I. Boybat, R. S. Shenoy, P. Narayanan, K. Virwani, E. U. Giacometti, B. N. Kurdi, and H. Hwang, "Experimental demonstration and tolerancing of a large-scale neural network (165,000 synapses) using phase-change memory as the synaptic weight element," *IEEE Trans. Electron Devices*, vol. 62, no. 11, pp. 3498–3507, Dec. 2014, doi: 10.1109/iedm.2014.704713.
[24] A. Pantazi, S. Wozniak, T. Tuma, and E. Eleftheriou, "All-memristive neuromorphic computing with level-tuned neurons," *Nanotechnology*, vol. 27, no. 35, 2016, Art. no. 355205.
[25] M. Wuttig and N. Yamada, "Phase-change materials for rewriteable data storage," *Nature Mater.*, vol. 6, no. 11, pp. 824–832, Nov. 2007.
[26] A. J. G. Mank, A. E. T. Kuiper, H. A. G. Nulens, B. Feddes, and G. Wei, "Detection of recording marks on digital versatile discs and blu-ray discs using conductive atomic force microscopy," *Jpn. J. Appl. Phys.*, vol. 46, no. 9A, pp. 5813–5820, Sep. 2007.
[27] W. H. P. Pernice and H. Bhaskaran, "Photonic non-volatile memories using phase change materials," *Appl. Phys. Lett.*, vol. 101, no. 17, 2012, Art. no. 171101.
[28] W. Zhang, R. Mazzarello, and E. Ma, "Phase-change materials in electronics and photonics," *MRS Bull.*, vol. 44, no. 9, 2012, Art. no. 171101.
[29] W. Chen, R. Chen, Y. Zhou, and Y. Ma, "A switchable metasurface between meta-lens and absorber," *IEEE Photon. Technol. Lett.*, vol. 31, no. 14, pp. 1187–1190, Jul. 15, 2019.
[30] H.-K. Ji, H. Tong, H. Qian, Y.-J. Hui, N. Liu, P. Yan, and X.-S. Miao, "Non-binary colour modulation for display device based on phase change materials," *Sci. Rep.*, vol. 6, no. 1, p. 39206, Dec. 2016.
[31] M. A. Kats, D. Sharma, J. Lin, P. Genevet, R. Blanchard, Z. Yang, M. M. Qazilbash, D. N. Basov, S. Ramanathan, and F. Capasso, "Ultra-thin perfect absorber employing a tunable phase change material," *Appl. Phys. Lett.*, vol. 101, no. 12, 2012, Art. no. 221101.
[32] M. A. Kats, R. Blanchard, P. Genevet, and Z. Yang, "Thermal tuning of mid-infrared plasmonic antenna arrays using a phase change material," *Opt. Lett.*, vol. 38, no. 3, pp. 368–370, 2013.
[33] S. R. Ovshinsky, "Reversible electrical switching phenomena in disordered structures," *Phys. Rev. Lett.*, vol. 21, no. 20, pp. 1450–1453, Nov. 1968.
[34] M. Chen, K. A. Rubin, and R. W. Barton, "Compound materials for reversible, phase-change optical data storage," *Appl. Phys. Lett.*, vol. 49, no. 9, pp. 502–504, 1986.
[35] N. Yamada, M. Takenaga, and M. Takao, "Te-Ge-Sn-Au Phase change recording film for optical disk," *Proc. SPIE*, vol. 695, pp. 79–85, Jan. 1986.
[36] E. Ohno, N. Yamada, T. Kurumizawa, K. Kimura, and M. Takao, "TeGeSnAu alloys for phase change type optical disk memories," *Jpn. J. Appl. Phys.*, vol. 28, no. 7, pp. 1235–1240, 1989.
[37] N. Yamada, E. Ohno, K. Nishiuchi, N. Akahira, and M. Takao, "Rapid-phase transitions of GeTe-Sb_2Te_3 pseudobinary amorphous thin films for an optical disk memory," *J. Appl. Phys.*, vol. 69, no. 5, pp. 2849–2856, 1991.
[38] K. Yusu, T. Nakai, S. Ashida, N. Ohmachi, N. Morishita, and N. Nakamura. (2005). *Highspeed Crystallization Characteristics of Ge–Sb–Te–Bi Materials Used for Next Generation Rewritable DVD With Blue Laser and NA=0.65*. [Online]. Available: http://www.epcos.org
[39] H. Kusada, T. Hosaka, R. Kojima, and N. Yamada, "Effect of excess Sb on GeTe–Sb_2Te_3–Bi_2Te_3 recording films," in *Proc. 18th Symp. PCOS*, 2006, pp. 1–8.
[40] CN. Afonso, J. Solis, F. Catalina, and C. Kalpouzos, "Ultrafast reversible phase change in GeSb films for erasable optical storage," *Appl. Phys. Lett.*, vol. 60, no. 25, pp. 3123–3125, 1992.
[41] H. Iwasaki, M. Harigaya, O. Nonoyama, Y. Kageyama, M. Takahashi, K. Yamada, H. Degushi, and Y. Ide, "Completely erasable phase change optical disk II-application of Ag-In-Sb-Te mixed-phased system for CD rewritable compatible disc compatible with CD-velocity and double CD-velocity," *Jpn. J. Appl. Phys.*, vol. 32, pp. 5241–5247, May 1993.
[42] T. Cao and M. J. Cen, "Fundamentals and applications of Chalcogenide phase-change material photonics," *Adv. Theory Simul.*, vol. 2, Aug. 2019, Art. no. 1900094.
[43] A. Lotnyk, M. Behrens, and B. Rauschenbach, "Phase change thin films for non-volatile memory applications," *Nanosc. Adv.*, vol. 1, no. 10, pp. 3836–3857, 2019.
[44] T. Matsunaga, N. Yamada, and Y. Kubota, "Structures of stable and metastable $Ge_2Sb_2Te_5$, an intermetallic compound in GeTe–Sb_2Te_3 pseudobinary systems," *Acta Crystallogr.*, vol. 60, no. 6, pp. 685–691, 2004.
[45] A. Lotnyk, S. Bernütz, X. Sun, U. Ross, M. Ehrhardt, and B. Rauschenbach, "Real-space imaging of atomic arrangement and vacancy layers ordering in laser crystallised $Ge_2Sb_2Te_5$ phase change thin films," *Acta Mater.*, vol. 105, pp. 1–8, Feb. 2016.
[46] B. Zhang, W. Zhang, Z. J. Shen, Y. J. Chen, J. X. Li, S. B. Zhang, Z. Zhang, M. Wuttig, R. Mazzarello, E. Ma, and X. D. Han, "Element-resolved atomic structure imaging of rocksalt $Ge_2Sb_2Te_5$ phase-change material," *Appl. Phys. Lett.*, vol. 108, no. 19, 2016, Art. no. 191902.
[47] C. Koch, T. Dankwort, A.-L. Hansen, M. Esters, D. Häußler, H. Volker, A. von Hoegen, M. Wuttig, D. C. Johnson, W. Bensch, and L. Kienle, "Investigation of the phase change mechanism of $Ge_6Sn_2Sb_2Te_{11}$," *Acta Mater.*, vol. 152, pp. 278–287, Jun. 2018.
[48] U. Ross, A. Lotnyk, E. Thelander, and B. Rauschenbach, "Direct imaging of crystal structure and defects in metastable $Ge_2Sb_2Te_5$ by quantitative aberration-corrected scanning transmission electron microscopy," *Appl. Phys. Lett.*, vol. 104, no. 12, 2014, Art. no. 121904.
[49] Y. Zheng, Y. Wang, T. Xin, Y. Cheng, R. Huang, P. Liu, M. Luo, Z. Zhang, S. Lv, Z. Song, and S. Feng, "Direct atomic identification of cation migration induced gradual cubic-to-hexagonal phase transition in Ge2Sb2Te5," *Commun. Chem.*, vol. 2, no. 1, pp. 1–9, Dec. 2019.

[50] I. Hilmi, A. Lotnyk, J. W. Gerlach, P. Schumacher, and B. Rauschenbach, "Epitaxial formation of cubic and trigonal Ge-Sb-Te thin films with heterogeneous vacancy structures," *Mater. Des.*, vol. 115, pp. 138–146, Feb. 2017.

[51] T. Rosenthal, S. Welzmiller, L. Neudert, P. Urban, A. Fitch, and O. Oeckler, "Novel superstructure of the rocksalt type and element distribution in germanium tin antimony tellurides," *J. Solid State Chem.*, vol. 219, pp. 108–117, Nov. 2014.

[52] P. Urban, M. N. Schneider, L. Erra, S. Welzmiller, F. Fahrnbauer, and O. Oeckler, "Temperature dependent resonant X-ray diffraction of single-crystalline $Ge_2Sb_2Te_5$," *CrystEngComm*, vol. 15, no. 24, pp. 4823–4829, 2013.

[53] R. Zallen, "Models of amorphous solids," *J. Non-Crystalline Solids*, vol. 75, nos. 1–3, pp. 3–14, Oct. 1985.

[54] A. V. Kolobov, P. Fons, A. I. Frenkel, A. L. Ankudinov, J. Tominaga, and T. Uruga, "Understanding the phase-change mechanism of rewritable optical media," *Nature Mater.*, vol. 3, no. 10, pp. 703–708, Oct. 2004.

[55] W. Wełnic, A. Pamungkas, R. Detemple, C. Steimer, S. Blügel, and M. Wuttig, "Unravelling the interplay of local structure and physical properties in phase-change materials," *Nature Mater.*, vol. 5, no. 1, pp. 56–62, Jan. 2006.

[56] W. Welnic, S. Botti, I. Reining, and M. Wuttig, "Origin of the optical contrast in phase-change materials," *Phys. Rev. Lett.*, vol. 98, Jun. 2007, Art. no. 236403.

[57] D. A. Baker, M. A. Paesler, G. Lucovsky, S. C. Agarwal, and P. C. Taylor, "Application of bond constraint theory to the switchable optical memory material $Ge_2Sb_2Te_5$," *Phys. Rev. Lett.*, vol. 96, Jun. 2006, Art. no. 255501.

[58] S. Kohara, K. Kato, S. Kimura, H. Tanaka, T. Usuki, K. Suzuya, H. Tanaka, Y. Moritomo, T. Matsunaga, N. Yamada, Y. Tanaka, H. Suematsu, and M. Tanata, "Structural basis for the fast phase change of $Ge_2Sb_2Te_5$: Ring statistics analogy between the crystal and amorphous states," *Appl. Phys. Lett.*, vol. 89, no. 20, 2006, Art. no. 201910.

[59] J. Akola and R. O. Jones, "Structural phase transitions on the nanoscale: The crucial pattern in the phase-change materials $Ge_2Sb_2Te_5$ and GeTe," *Phys. Rev. B, Condens. Matter*, vol. 76, Dec. 2007, Art. no. 235201.

[60] J. Akola, R. O. Jones, S. Kohara, S. Kimura, K. Kobayashi, M. Takata, T. Matsunaga, R. Kojima, and N. Yamada, "Experimentally constrained density-functional calculations of the amorphous structure of the prototypical phase-change material $Ge_2Sb_2Te_5$," *Phys. Rev. B, Condens. Matter*, vol. 80, Jul. 2009, Art. no. 020201.

[61] J. Akola and R. O. Jones, "Structure of Amorphous $Ge_8Sb_2Te_{11}$: GeTe–Sb_2Te_3 Alloys and Optical Storage," *Phys. Rev. B, Condens. Matter*, vol. 79, Apr. 2009, Art. no. 134118.

[62] K. Shportko, S. Kremers, M. Woda, D. Lencer, J. Robertson, and M. Wuttig, "Resonant bonding in crystalline phase-change materials," *Nature Mater.*, vol. 7, no. 8, pp. 653–658, Aug. 2008.

[63] C. H. Chu, M. L. Tseng, J. Chen, P. C. Wu, Y.-H. Chen, H.-C. Wang, T.-Y. Chen, W. T. Hsieh, H. J. Wu, G. Sun, and D. P. Tsai, "Active dielectric metasurface based on phase-change medium," *Laser Photon. Rev.*, vol. 10, no. 6, pp. 986–994, Nov. 2016.

[64] T. Tsafack, E. Piccinini, B.-S. Lee, E. Pop, and M. Rudan, "Electronic, optical and thermal properties of the hexagonal and rocksalt-like $Ge_2Sb_2Te_5$ chalcogenide from first-principle calculations," *J. Appl. Phys.*, vol. 110, no. 6, 2011, Art. no. 063716.

[65] M. Behrens, A. Lotnyk, U. Roß, J. Griebel, P. Schumacher, J. W. Gerlach, and B. Rauschenbach, "Impact of disorder on optical reflectivity contrast of epitaxial $Ge_2Sb_2Te_5$ thin films," *CrystEngComm*, vol. 20, no. 26, pp. 3688–3695, 2018.

[66] J. E. Boschker, X. Lü, V. Bragaglia, R. Wang, H. T. Grahn, and R. Calarco, "Electrical and optical properties of epitaxial binary and ternary GeTe-Sb_2Te_3 alloys," *Sci. Rep.*, vol. 8, no. 1, pp. 5889–5896, Dec. 2018.

[67] L. Wang, L. Tu, and J. Wen, "Application of phase-change materials in memory taxonomy," *Sci. Technol. Adv. Mater.*, vol. 18, no. 1, pp. 406–429, Dec. 2017.

[68] N. Kato, Y. Takeda, T. Fukano, T. Motohiro, S. Kawai, and H. Kuno, "Compositional dependence of optical constants and microstructures of GeSbTe thin films for Compact-Disc-Rewritable (CD-RW) readable with conventional CD-ROM drives," *Jpn. J. Appl. Phys.*, vol. 38, no. 3, pp. 1707–1708, Mar. 1999.

[69] Y. Satoh, T. Nakai, and S. Ashida, "Development of 40 GB dual-layer rewritable HD DVD media," *Proc. SPIE*, vol. 6620, May 2007, Art. no. 66202A.

[70] H. Shingai, T. Kato, M. Kosuda, Y. Takagi, H. Oyake, and H. Hirata, "Triple-layer rewritable disc with Sb-based phase-change material," *Jpn. J. Appl. Phys.*, vol. 49, no. 8S2, 2010, Art. no. 08KG02.

[71] L. Wang, C.-H. Yang, S. Gai, and J. Wen, "Current status and future prospects of conventional recording technologies for mass storage applications," *Current Nanosci.*, vol. 10, no. 5, pp. 638–659, Aug. 2014.

[72] K. Yamamoto, K. Osato, I. Ichimura, F. Maeda, and T. Watanabe, "0.8-numerical-aperture two-element objective lens for the optical disk," *Jpn. J. Appl. Phys.*, vol. 36, no. 1B, pp. 456–459, 1997.

[73] J.-H. Kim and J.-S. Lee, "Cover-layer with high refractive index for near-field recording media," *Jpn. J. Appl. Phys.*, vol. 46, no. 6B, pp. 3993–3996, Jun. 2007.

[74] A. V. Kolobov, P. Fons, and J. Tominaga, "Phase-change optical recording: Past, present, future," *Thin Solid Films*, vol. 515, no. 19, pp. 7534–7537, Jul. 2007.

[75] L. P. Shi, T. C. Chong, E. M. Wee, X. S. Miao, P. K. Tan, K. G. Lim, J. Li, and W. Qiang, "Investigation on rewritable multilevel reflection modulation recording phase-change optical disk," *Proc. SPIE*, vol. 39, pp. 733–736, Jan. 2000.

[76] X. X. Sun, A. Lotnyk, M. Ehrhardt, J. W. Gerlach, and B. Rauschenbach, "Realization of multilevel states in phase-change thin films by fast laser pulse irradiation," *Adv. Opt. Mater.*, vol. 5, no. 12, 2017, Art. no. 1700169.

[77] B. Jiang, Z. L. Shen, J. W. Cai, H. H. Tang, H. Xing, and W. H. Huang, "New method of two-photon multi-layer optical disc storage," *Proc. SPIE*, vol. 6150, Feb. 2006, Art. no. 61503Q.

[78] T. Nakai, T. Tsukamoto, S. Ashida, K. Yusu, N. Yoshida, K. Umezawa, N. Ohmachi, N. Morishita, N. Nakamura, and K. Ichihara, "Dual-layer rewritable phase-change recording media for HD DVD system," *Jpn. J. Appl. Phys.*, vol. 43, no. 7B, pp. 4987–4991, Jul. 2004.

[79] S. Pu, H. Tang, B. Chen, J. Xu, and W. Huang, "Photochromic diarylethene for two-photon 3D optical storage," *Mater. Lett.*, vol. 60, nos. 29–30, pp. 3553–3557, 2006.

[80] M. Wuttig, H. Bhaskaran, and T. Taubner, "Phase-change materials for non-volatile photonic applications," *Nature Photon.*, vol. 11, no. 8, pp. 465–476, Aug. 2017.

[81] M. Rude, J. Pello, R. E. Simpson, J. Osmond, G. Roelkens, J. J. G. M. Van der Tol, and V. Pruneri, "Optical switching at 1.55 μm in silicon racetrack resonators using phase change materials," *Appl. Phys. Lett.*, vol. 103, no. 14, 2013, Art. no. 141119.

[82] C. Rios, P. Hosseini, C. D. Wright, H. Bhaskaran, and W. H. P. Pernice, "On-chip photonic memory elements employing phase-change materials," *Adv. Mater.*, vol. 26, no. 9, pp. 1372–1377, Mar. 2014.

[83] C. Ríos, M. Stegmaier, P. Hosseini, D. Wang, T. Scherer, C. D. Wright, H. Bhaskaran, and W. H. P. Pernice, "Integrated all-photonic non-volatile multi-level memory," *Nature Photon.*, vol. 9, pp. 725–733, Sep. 2015.

[84] C. Rios, M. Stegmaier, and Z. Cheng, "Controlled switching of phase-change materials by evanescent-field coupling in integrated photonics," *Opt. Mater. Express*, vol. 8, no. 9, pp. 2455–2470, Sep. 2018.

[85] X. Li, N. Youngblood, C. Rios, Z. G. Cheng, C. D. Wright, W. H. P. Pernice, and H. Bhaskaran, "Fast and reliable storage using a 5 bit, nonvolatile photonic memory cell," *Optica*, vol. 6, no. 1, pp. 1–6, 2019.

[86] J. Zheng, S. Zhu, P. Xu, S. Dunham, and A. Majumdar, "Modeling electrical switching of nonvolatile phase-change integrated nanophotonic structures with graphene heaters," *ACS Appl. Mater. Interfaces*, vol. 12, no. 19, pp. 21827–21836, 2020.

[87] Z. Fang, J. Zheng, P. Xu, and A. Majumdar, "GST integrated silicon photonics," *Proc. SPIE*, vol. 11081, Feb. 2019, Art. no. 110811Q.

[88] Z. Fang, J. Zheng, P. Xu, S. Deshmukh, E. Pop, and A. Majumdar, "Phase change material integrated silicon photonics: GST and beyond," *Proc. SPIE*, vol. 11276, Mar. 2020, Art. no. 1127602.

[89] X. Li, N. Youngblood, Z. Cheng, S. G. C. Carrillo, E. Gemo, W. H. P. Pernice, C. D. Wright, and H. Bhaskaran, "Experimental investigation of silicon and silicon nitride platforms for phase-change photonic in-memory computing," *Optica*, vol. 7, no. 3, pp. 218–225, 2020.

[90] H. Zhang, L. Zhou, J. Xu, N. Wang, H. Hu, L. Lu, B. M. A. Rahman, and J. Chen, "Nonvolatile waveguide transmission tuning with electrically-driven ultra-small GST phase-change material," *Sci. Bull.*, vol. 64, no. 11, pp. 782–789, Jun. 2019.

[91] J. Feldmann, M. Stegmaier, N. Gruhler, C. Ríos, H. Bhaskaran, C. D. Wright, and W. H. P. Pernice, "Calculating with light using a chip-scale all-optical abacus," *Nature Commun.*, vol. 8, no. 1, pp. 8–1256, Dec. 2017.

[92] H. Zhang, L. Zhou, L. Lu, J. Xu, N. Wang, H. Hu, B. A. Rahman, Z. Zhou, and J. Chen, "Miniature multilevel optical memristive switch using phase change material," *ACS Photon.*, vol. 6, no. 9, pp. 2205–2212, 2019.

[93] L. Yu, Y. L. Yin, Y. C. Shi, D. X. Dai, and S. L. He, "Thermally tunable silicon photonic microdisk resonator with transparent graphene nanoheaters," *Optica*, vol. 3, no. 2, pp. 159–166, 2016.

[94] C. S. G. Gemo, C. R. De Galarreta, A. Baldycheva, H. Hayat, N. Youngblood, H. Bhaskaran, W. H. P. Pernice, and C. D. Wright, "Plasmonically-enhanced all-optical integrated phase-change memory," *Opt. Express*, vol. 27, no. 17, pp. 24724–24737, 2019.

[95] N. Farmakidis, N. Youngblood, X. Li, J. Tan, J. L. Swett, Z. Cheng, C. D. Wright, W. H. P. Pernice, and H. Bhaskaran, "Plasmonic nanogap enhanced phase-change devices with dual electrical-optical functionality," *Sci. Adv.*, vol. 5, no. 11, Nov. 2019, Art. no. eaaw2687.

[96] A. Sebastian, M. Le Gallo, and E. Eleftheriou, "Computational phase-change memory: Beyond von Neumann computing," *J. Phys. D, Appl. Phys.*, vol. 52, no. 44, 2019, Art. no. 443002.

[97] E. J. Fuller, Y. Li, C. Bennet, S. T. Keene, A. Melianas, S. Agarwal, M. J. Marinella, A. Salleo, and A. A. Talin, "Redox transistors for neuromorphic computing," *IBM J. Res. Develop.*, vol. 63, no. 6, pp. 9–18, 2019.

[98] Z. G. Cheng, C. Rios, N. Youngblood, C. D. Wright, W. H. P. Pernice, and H. Bhaskaran, "Device-level photonic memories and logic applications using phase-change materials," *Adv. Mater.*, vol. 30, Aug. 2018, Art. no. 1802435.

[99] C. Rios, N. Youngblood, Z. G. Cheng, M. Le Gallo, W. H. P. Pernice, C. D. Wright, A. Sebastian, and H. Bhaskaran, "In-memory computing on a photonic platform," *Sci. Adv.*, vol. 5, no. 2, 2019, Art. no. eaau5759.

[100] J. Feldmann, N. Youngblood, X. Li, C. D. Wright, H. Bhaskaran, and W. H. P. Pernice, "Integrated 256 cell photonic phase-change memory with 512-bit capacity," *IEEE J. Sel. Topics Quantum Electron.*, vol. 26, no. 2, pp. 1–7, Mar. 2020.

[101] J. Feldmann, N. Youngblood, M. Karpov, H. Gehring, X. Li, M. Le Gallo, X. Fu, A. Lukashchuk, A. Raja, J. Liu, D. Wright, A. Sebastian, T. Kippenberg, W. Pernice, and H. Bhaskaran, "Parallel convolution processing using an integrated photonic tensor core," 2020, *arXiv:2002.00281*. [Online]. Available: http://arxiv.org/abs/2002.00281

[102] V. Bangari, B. A. Marquez, H. Miller, A. N. Tait, M. A. Nahmias, T. F. de Lima, H.-T. Peng, and P. R. Prucnal, "Digital electronics and analog photonics for convolutional neural networks (DEAP-CNNs)," *IEEE J. Sel. Topics Quantum Electron.*, vol. 26, no. 1, Jan./Feb. 2020, Art. no. 7701213.

[103] A. N. Tait, T. F. de Lima, E. Zhou, A. X. Wu, M. A. Nahmias, B. J. Shastri, and P. R. Prucnal, "Neuromorphic photonic networks using silicon photonic weight banks," *Sci. Rep.*, vol. 7, no. 1, p. 7430, Dec. 2017.

[104] M. A. Nahmias, T. F. de Lima, A. N. Tait, H.-T. Peng, B. J. Shastgri, and P. R. Prucnal, "Photonic multiply-accumulate operations for neural networks," *Sci. Rep.*, vol. 26, Feb. 2019, Art. no. 7701518.

[105] D. Silver, J. Schrittwieser, K. Simonyan, I. Antonoglou, A. Huang, A. Guez, T. Hubert, L. Baker, M. Lai, A. Bolton, Y. Chen, T. Lillicrap, F. Hui, L. Sifre, G. van den Driessche, T. Graepel, and D. Hassabis, "Mastering the game of go without human knowledge," *Nature*, vol. 550, no. 7676, pp. 354–359, Oct. 2017.

[106] Q. Z. Wan, M. T. Sharbati, J. R. Erickson, Y. H. Du, and F. Xiong, "Emerging artificial synaptic devices for neuromorphic computing," *Adv. Mater. Technol.*, vol. 4, Apr. 2019, Art. no. 1900037.

[107] MT. Sharbati, YH. Du, J. Torres, ND. Ardolino, M. Yun, and F. Xiong, "Low-power, electrochemically tunable graphene synapses for neuromorphic computing," *Adv. Mater.*, vol. 4, Sep. 2018, Art. no. 1802353.

[108] M. A. Lynch, "Long-term potentiation and memory," *Physiol. Rev.*, vol. 84, no. 1, pp. 87–136, Jan. 2004, doi: 10.1152/physrev.00014.2003.

[109] N. K. Upadhyay, S. Joshi, and J. J. Yang, "Synaptic electronics and neuromorphic computing," *Sci. China Inf. Sci.*, vol. 59, no. 6, Jun. 2016, Art. no. 061404.

[110] A. L. Hodgkin and A. F. Huxley, "Action potentials recorded from inside a nerve fibre," *Nature*, vol. 144, pp. 710–711, Oct. 1939.

[111] Y. Li, Y. Zhong, L. Xu, J. Zhang, X. Xu, H. Sun, and X. Miao, "Ultrafast synaptic events in a chalcogenide memristor," *Sci. Rep.*, vol. 3, no. 1, p. 1619, Dec. 2013.

[112] B. L. Jackson, B. Rajendran, G. S. Corrado, M. J. Breitwisch, G. W. Burr, R. Cheek, K. Gopalakrishnan, S. Raoux, C. T. Rettner, R. S. Shenoy, B. N. Kurdi, C. H. Lam, and D. S. Modha, "Nanoscale electronic synapses using phase change devices," *ACM J. Emerg. Technol. Comput. Syst.*, vol. 9, no. 2, pp. 12–20, 2013.

[113] ZG. Cheng, C. Rios, W. H. P. Pernice, C. D. Wright, and H. Bhaskaran, "On-chip photonic synapse," *Sci. Adv.*, vol. 3, no. 9, 2017, Art. no. e1700160.

[114] I. Chakraborty, G. Saha, A. Sengupta, and K. Roy, "Toward fast neural computing using all-photonic phase change spiking neurons," *Sci. Rep.*, vol. 8, no. 1, p. 12980, Dec. 2018.

[115] I. Chakraborty, G. Saha, and K. Roy, "Photonic in-memory computing primitive for spiking neural networks using phase-change materials," *Phys. Rev. A, Gen. Phys.*, vol. 11, no. 1, Jan. 2019, Art. no. 014063.

[116] J. Feldmann, N. Youngblood, C. D. Wright, H. Bhaskaran, and W. H. P. Pernice, "All-optical spiking neurosynaptic networks with self-learning capabilities," *Nature*, vol. 569, pp. 208–214, May 2019.

[117] D. R. Smith, W. J. Padilla, D. C. Vier, S. C. Nemat-Nasser, and S. Schultz, "Composite medium with simultaneously negative permeability and permittivity," *Phys. Rev. Lett.*, vol. 84, no. 18, pp. 4184–4187, May 2000.

[118] N. I. Zheludev and Y. S. Kivshar, "From metamaterials to metadevices," *Nature Mater.*, vol. 11, pp. 917–924, Nov. 2012.

[119] A. Ciattoni, C. Rizza, A. Marini, A. D. Falco, D. Faccio, and M. Scalora, "Enhanced nonlinear effects in pulse propagation through epsilon-near-zero media," *Laser Photon. Rev.*, vol. 10, no. 3, pp. 517–525, 2016.

[120] A. V. Kildishev, A. Boltasseva, and V. M. Shalaev, "Planar photonics with metasurfaces," *Science*, vol. 339, no. 6125, 2013, Art. no. 1232009.

[121] N. Yu, P. Genevet, M. A. Kats, F. Aieta, J.-P. Tetienne, F. Capasso, and Z. Gaburro, "Light propagation with phase discontinuities: Generalized laws of reflection and refraction," *Science*, vol. 334, no. 6054, pp. 333–337, 2011.

[122] A. E. Minovich, A. E. Miroshnichenko, A. Y. Bykov, T. V. Murzina, D. N. Neshev, and Y. S. Kivshar, "Functional and nonlinear optical metasurfaces," *Laser Photon. Rev.*, vol. 9, no. 2, pp. 195–213, Mar. 2015.

[123] S. Wang, D. C. Abeysinghe, and Q. Zhan, "Generation of vectorial optical fields with slot-antenna-based metasurface," *Opt. Lett.*, vol. 40, no. 20, pp. 4711–4714, 2015.

[124] L.-J. Black, Y. Wang, C. H. de Groot, A. Arbouet, and O. L. Muskens, "Optimal polarization conversion in coupled dimer plasmonic nanoantennas for metasurfaces," *ACS Nano*, vol. 8, no. 6, pp. 6390–6399, Jun. 2014.

[125] J. Wang and J. Du, "Plasmonic and dielectric metasurfaces: Design, fabrication and applications," *Appl. Sci.*, vol. 6, no. 9, p. 239, 2016.

[126] F. van Beijnum, P. J. van Veldhoven, E. J. Geluk, M. J. A. de Dood, G. W.'t Hooft, and M. P. van Exter, "Surface plasmon lasing observed in metal hole arrays," *Phys. Rev. Lett.*, vol. 110, no. 20, pp. 106–110, May 2013.

[127] C. Genet and T. W. Ebbesen, "Light in tiny holes," *Nature*, vol. 445, no. 7123, pp. 39–46, Jan. 2007.

[128] F. J. García de Abajo, "Colloquium: Light scattering by particle and hole arrays," *Rev. Mod. Phys.*, vol. 79, no. 4, pp. 1267–1290, Oct. 2007.

[129] Z. L. Samson, K. F. MacDonald, F. De Angelis, B. Gholipour, K. Knight, C. C. Huang, E. Di Fabrizio, D. W. Hewak, and N. I. Zheludev, "Metamaterial electro-optic switch of nanoscale thickness," *Appl. Phys. Lett.*, vol. 96, no. 14, 2010, Art. no. 143105.

[130] B. Gholipour, J. Zhang, K. F. MacDonald, D. W. Hewak, and N. I. Zheludev, "An all-optical, non-volatile, bidirectional, phase-change meta-switch," *Adv. Mater.*, vol. 25, no. 22, pp. 3050–3054, Jun. 2013.

[131] T. Cao, C.-W. Wei, R. E. Simpson, L. Zhang, and M. J. Cryan, "Perfect absorber using a phase-change metamaterial at visible frequenciess," *Sci. Rep.*, vol. 4, pp. 3955–3962, Apr. 2015.

[132] S. G. C. Carrillo, G. R. Nash, H. Hayat, M. J. Cryan, M. Klemm, H. Bhaskaran, and C. D. Wright, "Design of practicable phase-change metadevices for near-infrared absorber and modulator applications," *Opt. Express*, vol. 24, no. 12, pp. 13563–13573, 2016.

[133] A.-K.-U. Michel, D. N. Chigrin, T. W. W. Maß, K. Schönauer, M. Salinga, M. Wuttig, and T. Taubner, "Using low-loss phase-change materials for mid-infrared antenna resonance tuning," *Nano Lett.*, vol. 13, no. 8, pp. 3470–3475, Aug. 2013.

[134] A.-K.-U. Michel, P. Zalden, D. N. Chigrin, M. Wuttig, A. M. Lindenberg, and T. Taubner, "Reversible optical switching of infrared antenna resonances with ultrathin phase-change layers using femtosecond laser pulses," *ACS Photon.*, vol. 1, no. 9, pp. 833–839, Sep. 2014.

[135] Y. G. Chen, T. S. Kao, B. Ng, X. Li, and X. G. Luo, "Hybrid phase-change plasmonic crystals for active tuning of lattice resonances," *Opt. Express*, vol. 21, no. 11, pp. 13691–13698, 2013.
[136] T. Cao, G. Z. Zheng, S. Wang, and C. W. Wei, "Ultrafast beam steering using gradient Au-$Ge_2Sb_2Te_5$-Au plasmonic resonators," *Opt. Express*, vol. 23, no. 14, pp. 18029–18039, 2015.
[137] C. Ruiz de Galarreta, A. M. Alexeev, Y.-Y. Au, M. Lopez-Garcia, M. Klemm, M. Cryan, J. Bertolotti and, and C. D. Wright, "Nonvolatile reconfigurable phase-change metadevices for beam steering in the near infrared," *Adv. Funct. Mater.*, vol. 28, Mar. 2018, Art. no. 1704993.
[138] Y. Yang, I. I. Kravchenko, D. P. Briggs, and J. Valentine, "All-dielectric metasurface analogue of electromagnetically induced transparency," *Nature Commun.*, vol. 5, no. 1, pp. 5753–5761, Dec. 2014.
[139] Y. A. Karvounis, B. Gholipour, K. F. MacDonald, and N. I. Zheludev, "All-dielectric phase-change reconfigurable metasurface," *Appl. Phys. Lett.*, vol. 109, no. 5, 2016, Art. no. 051103.
[140] Q. Wang, E. T. F. Rogers, B. Gholipour, C.-M. Wang, G. Yuan, J. Teng, and N. I. Zheludev, "Optically reconfigurable metasurfaces and photonic devices based on phase change materials," *Nature Photon.*, vol. 10, no. 1, pp. 60–65, Jan. 2016.
[141] P. Li, XS. Yang, T. W. W. Ma, J. Hanss, M. Lewin, A-K. Michel, M. Wuttig, and T. Taubner, "Reversible optical switching of highly confined phonon–polaritons with an ultrathin phase-change material," *Nature Mater.*, vol. 10, pp. 60–65, May 2015.
[142] M. Y. Shalaginov, S. An, Y. Zhang, F. Yang, P. Su, V. Liberman, J. B. Chou, C. M. Roberts, M. Kang, C. Rios, Q. Du, C. Fowler, A. Agarwal, K. Richardson, C. Rivero-Baleine, H. Zhang, J. Hu, and T. Gu, "Reconfigurable all-dielectric metalens with diffraction limited performance," 2019, *arXiv:1911.12970*. [Online]. Available: http://arxiv.org/abs/1911.12970
[143] A. Leitis, A. Heßler, S. Wahl, M. Wuttig, T. Taubner, A. Tittl, and H. Altug, "All-dielectric programmable Huygens' metasurfaces," *Adv. Funct. Mater.*, vol. 30, May 2019, Art. no. 1910259.
[144] M. Kerker, D.-S. Wang, and C. L. Giles, "Electromagnetic scattering by magnetic spheres," *J. Opt. Soc. Amer.*, vol. 73, no. 6, pp. 765–767, 1983.
[145] A. Forouzmand and H. Mosallaei, "Dynamic beam control via Mie-resonance based phase-change metasurface: A theoretical investigation," *Opt. Express*, vol. 26, no. 14, pp. 17948–17963, 2018.
[146] K. Chaudhary, M. Tamagnone, X. Yin, C. M. Spägele, S. L. Oscurato, J. Li, C. Persch, R. Li, N. A. Rubin, L. A. Jauregui, K. Watanabe, T. Taniguchi, P. Kim, M. Wuttig, J. H. Edgar, A. Ambrosio, and F. Capasso, "Polariton nanophotonics using phase-change materials," *Nature Commun.*, vol. 10, no. 1, pp. 1–6, Dec. 2019.
[147] P. Hosseini, C. D. Wright, and H. Bhaskaran, "An optoelectronic framework enabled by low-dimensional phase-change films," *Nature*, vol. 511, no. 7508, pp. 206–211, Jul. 2014.
[148] C. Ríos, P. Hosseini, R. A. Taylor, and H. Bhaskaran, "Color depth modulation and resolution in phase-change material nanodisplays," *Adv. Mater.*, vol. 28, no. 23, pp. 4720–4726, Jun. 2016.
[149] SGC. Carrillo, L. Trimby, Y-Y. Au, V. K. Nagareddy, G. Rodriguez-Hernandez, P. Hosseini, C. Rios, H. Bhaskaran, and C. D. Wright, "A nonvolatile phase-change metamaterial color display," *Adv. Opt. Mater.*, vol. 7, Sep. 2019, Art. no. 1801782.
[150] A. Scott, "Bodle technologies: Creating low-energy reflective displays–with color and video," in *Chemical & Engineering News*. Oxford, U.K.: Bodle Technologies, 2018, pp. 30–31.
[151] B. Broughton, L. Bandhu, C. Talagrand, S. Garcia-Castillo, M. Yang, H. Bhaskaran, and P. Hosseini, "Solid-state reflective displays (SRD) utilizing ultrathin phase-change materials," in *SID Symp. Dig. Tech. Paper*, 2017, pp. 546–549.
[152] C. Talagrand, G. Triggs, L. Bandhu, S. Garcia-Castillo, B. Broughton, H. Bhaskaran, and P. Hosseini, "Solid-state reflective displays (SRD) for video-rate, full color, outdoor readable displays," *J. Soc. Inf. Display*, vol. 26, no. 10, pp. 619–624, 2018.
[153] S. Garcia-Castillo, L. Feng, T. Bachmann, L. Bandhu, C. Talagrand, G. Triggs, K. Didewar, B. Broughton, Q. Yao, B. Bhaskaran, and P. Hosseini, "Solid-state reflective display (SRD) with LTPS diode backplane," in *SID Symp. Dig. Tech. Paper*, 2019, pp. 807–810.
[154] K. Huang, H. Liu, G. Si, Q. Wang, J. Lin, and J. Teng, "Photon-nanosieve for ultrabroadband and large-angle-of-view holograms," *Laser Photon. Rev.*, vol. 11, May 2017, Art. no. 1700025.
[155] J. Park, K. Lee, and Y. Park, "Ultrathin wide-angle large-area digital 3D holographic display using a non-periodic photon sieve," *Nature Commun.*, vol. 10, no. 1, pp. 1–8, Dec. 2019.
[156] K. Huang, H. Liu, F. J. Garcia-Vidal, M. Hong, B. Luk'yanchuk, J. Teng, and C.-W. Qiu, "Ultrahigh-capacity non-periodic photon sieves operating in visible light," *Nature Commun.*, vol. 6, no. 1, p. 7059, Nov. 2015.
[157] S. Yu, *Neuro-Inspired Computing Using Resistive Synaptic Devices*. Cham, Switzerland: Springer, 2017.
[158] R. Soref, "Tutorial: Integrated-photonic switching structures," *APL Photon.*, vol. 3, no. 2, 2018, Art. no. 021101.
[159] M. Stegmaier, J. Ebert, J. M. Meckbach, K. Ilin, M. Siegel, and W. H. P. Pernice, "Aluminum nitride nanophotonic circuits operating at ultraviolet wavelengths," *Appl. Phys. Lett*, vol. 104, no. 9, 2014, Art. no. 091108.
[160] Y. Zhang, J. B. Chou, J. Li, H. Li, Q. Du, and A. Yadav, "Broadband transparent optical phase change materials for high-performance nonvolatile photonics," *Nature Commun.*, vol. 10, no. 1, p. 4279, Dec. 2019.
[161] Z. Song, S. Song, M. Zhu, L. Wu, K. Ren, W. Song, and S. Feng, "From octahedral structure motif to sub-nanosecond phase transitions in phase change materials for data storage," *Sci. China Inf. Sci.*, vol. 61, no. 8, Aug. 2018, Art. no. 081302.
[162] X. Chen, Y. Chen, M. Yan, and M. Qiu, "Nanosecond photothermal effects in plasmonic nanostructures," *ACS Nano*, vol. 6, no. 3, pp. 2550–2557, Mar. 2012.
[163] Y. Zhai, J.-Q. Yang, Y. Zhou, J.-Y. Mao, Y. Ren, V. A. L. Roy, and S.-T. Han, "Toward non-volatile photonic memory: Concept, material and design," *Mater. Horizons*, vol. 5, no. 4, pp. 641–654, 2018.

JIANMIN WANG is currently pursuing the B.S. degree in electrical engineering with the School of Information Engineering, Nanchang Hangkong University, Nanchang, China.

LEI WANG received the B.Eng. degree in electrical engineering from the Beijing University of Science and Technology, Beijing, China, in 2003, the M.Sc. degree in electronic instrumentation systems from The University of Manchester, Manchester, U.K., in 2004, and the Ph.D. degree in Tbit/sq.in. scanning probe phase-change memory from the University of Exeter, Exeter, U.K., in 2009. From 2008 to 2011, he was employed as a Postdoctoral Research Fellow with the University of Exeter to work on a fellowship funded by European Commission. These works included the study of phase-change probe memory and phase-change memristor. Since 2012, he joined the Nanchang Hangkong University, Nanchang, China, as an Associated Professor, where he is involved in the phase-change memories, phase-change neural networks, and other phase-change-based optoelectronic devices and their potential applications.

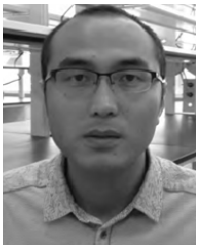

JUN LIU received the Ph.D. degree in control theory and control engineering from Zhejiang University, in 2007. From 2015 to 2016, he was a Visiting Scholar with the University of Houston. He is currently an Associate Professor with Nanchang Hangkong University. His research interests include in-memory computing, image registration, and pattern recognition.